CARBON NANOTUBE NETWORKS IN EPOXY COMPOSITES AND AEROGELS

Mateusz B. Bryning

A Dissertation

in

Physics and Astronomy

Presented to the Faculties of the University of Pennsylvania in Partial

Fulfillment of the Requirements for the Degree of Doctor of Philosophy

2007

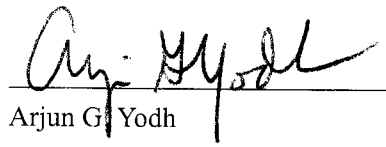

Arjun G. Yodh

Supervisor of Dissertation

Randall D. Kamien

Graduate Group Chairperson

UMI Number: 3271724

Copyright 2007 by
Bryning, Mateusz B.

All rights reserved.

INFORMATION TO USERS

The quality of this reproduction is dependent upon the quality of the copy submitted. Broken or indistinct print, colored or poor quality illustrations and photographs, print bleed-through, substandard margins, and improper alignment can adversely affect reproduction.

In the unlikely event that the author did not send a complete manuscript and there are missing pages, these will be noted. Also, if unauthorized copyright material had to be removed, a note will indicate the deletion.

UMI®

UMI Microform 3271724
Copyright 2007 by ProQuest Information and Learning Company.
All rights reserved. This microform edition is protected against unauthorized copying under Title 17, United States Code.

ProQuest Information and Learning Company
300 North Zeeb Road
P.O. Box 1346
Ann Arbor, MI 48106-1346

© Copyright 2007

by

Mateusz B. Bryning

Dedication

To Max and Natasza

Acknowledgements

I would like to acknowledge the help of many people during my study.

I am tremendously grateful to my advisor, Arjun Yodh, for his leadership and his steady and constant support.

I am also grateful to my family. I would particularly like to thank my wife, Natasza, for her patience and unwavering encouragement, and my parents, who planted and cultivated my interest in science and always went out of their way to offer any and every assistance.

Jay Kikkawa and Mohammad Islam were invaluable to all aspects of this work and have often illuminated my path ahead. Dan Milkie developed much of the measurement equipment and contributed greatly to the data taking and analysis.

I would like to thank all of the members of the Yodh group, past and present for their varied and significant help - Dan Chen, Ahmed Alsayed, Larry Hough, Yilong Han, Jian Zhang, Oni Basu, Matt Pelc, and all others. It has been a pleasure to work with you. Thank you also to Minus-nine Technologies, particularly Dave Kurz, for licensing our patent and lifting my morale, and for invaluable help with chemistry.

Thank you also to Paul Heiney for X-ray measurements, and to Brooks Harris, Tom Lubensky, Brian DiDonna, Charlie Johnson, and Karen Winey for their insight about percolation and nanotube networks.

This work was supported by grants from the National Science Foundation (MRSEC DMR-0079909, DMR-0203378, DMR05-20020 and DMR-0505048), NASA (NAG8-2172), and DARPA/ONR (N00015-01-1-0831).

Abstract

Carbon Nanotube Networks in Epoxy Composites and Aerogels

Mateusz B. Bryning

Arjun G. Yodh

This thesis describes the properties of carbon nanotube networks in epoxy composites and in novel carbon nanotube aerogels.

SWNT-Epoxy composites were created using a new procedure that enabled us to control SWNT concentration and dispersion quality in the composite. The composites exhibited percolation-like electrical conductivity with threshold volume fractions in the semi-dilute nanotube concentration regime. The observed electrical conductivites are described in terms of nanotube length, degree of aggregation, and sample homogeneity. By modifying the procedure to allow for nanotube chaining, conductive composites were created at SWNT volume fractions as low as 5.2 $(+1.9/-0.5)\times 10^{-5}$, the lowest reported to date. The thermal conductivity of SWNT-epoxy composites is also investigated. Composites were prepared using suspensions of SWNTs in N-N-Dimethylformamide (DMF) or surfactant stabilized aqueous SWNT suspensions. Thermal conductivity enhancement was observed in both types of composites, but DMF-processed composites showed an advantage at SWNT volume fractions between $\phi \sim 0.001$ to 0.005. Surfactant processed samples, however, allowed greater SWNT loading at which a larger overall enhancement (64 ± 9) % at $\phi \sim 0.1$ was observed. The enhancement differences are attributed to a tenfold higher SWNT/solid-composite interfacial thermal resistance in the surfactant-processed composites over DMF-processed composites. The interfacial resistance was extracted from the data using effective

medium theory.

Carbon nanotube aerogels were created by freeze drying and critical point drying aqueous carbon nanotube gels. The resulting aerogels have densities of approximately 0.01 to 0.06 g/cm^3 and maintain the dimensions of the wet gel. Critical point dried aerogels also preserve the microscopic three-dimensional network of *debundled* carbon nanotubes of the original gel. Pure SWNT aerogels are self-supporting. Reinforcement with small amounts of added polyvinyl alcohol (PVA) produces much stronger structures that can support at least 8000 times their own weight. Electrical conductivity of order 1 S/cm is observed in the self-supporting aerogels, and at least 10^{-2} S/cm can be achieved in PVA-reinforced aerogels through additional processing. The aerogels have potential applications in areas such as sensors, novel battery or supercapacitor electrodes, and ultra-light structural materials. They can be backfilled with polymers or other materials to create composites that retain the high conductivity of the network.

Contents

Dedication iii

Acknowledgements iv

Abstract v

List of Tables xiii

List of Figures xxx

1 Introduction 1

2 Overview of carbon nanotubes 6

2.1 Nanotube structure 6

2.2 Synthesis of single wall carbon nanotubes 10

2.2.1 Arc discharge 11

2.2.2 Laser oven 12

2.2.3 High pressure decomposition of carbon monoxide (HiPco) 12

2.2.4 Chemical vapor deposition (CVD) 13

2.2.5 CoMoCat 14

2.3 Some properties of single wall carbon nanotubes 15

2.3.1 Electrical properties 15

2.3.2 Thermal transport 20

2.3.3 Mechanical properties 23

3 Working with carbon nanotubes **25**

3.1 Dispersing carbon nanotubes 25

3.1.1 Sonication 25

3.1.2 Ultracentrifugation 28

3.1.3 Solvents, surfactants, and other solubilization methods 29

3.2 Characterization 34

3.2.1 Raman scattering 34

3.2.2 Thermogravimetric analysis 38

3.2.3 Atomic force microscopy 41

3.2.4 Electron microscopy 46

3.2.5 Energy-dispersive x-ray spectroscopy 51

3.2.6 Optical microscopy 54

3.2.7 Optical absorption 54

3.2.8 Fluorescence 56

3.2.9 X-ray diffraction 58

3.2.10 Small Angle Neutron Scattering 62

3.3 SWNT purification 64

3.3.1 HiPco purification example 66

4 Percolation and effective medium theories **74**

4.1 Percolation 75

4.1.1 Lattice percolation 77

4.1.2 Percolation of rods 83

4.1.3 Summary - percolation of carbon nanotubes 89

4.2 Effective medium theory 90

4.2.1 Basic formulation 90

4.2.2 Ellipsoidal particles with interfacial thermal resistance 94

5 Electrical conductivity of SWNT/Epoxy composites **100**

5.1 Background 100

5.2 Materials 103

5.2.1 Single Wall Carbon Nanotubes 103

5.2.2 Epoxy 104

5.3 Composite preparation 106

5.4 Electrical conductivity measurement 109

5.4.1 Two-point and Four-point measurements 109

5.4.2 High impedance measurements 112

5.4.3 Sample preparation 115

5.5 Results 116

5.6 Discussion 119

6 Thermal Conductivity of SWNT/Epoxy composites **122**

6.1 Background 122

6.2 Materials and Preparation 124
6.3 Thermal conductivity measurement 125
6.4 Results and discussion 127

7 Carbon Nanotube Aerogels **131**

7.1 Background 131
7.2 Aerogel Preparation 133
7.2.1 Materials and wet gel preparation 133
7.2.2 Critical-point drying and freeze drying 134
7.3 Aerogel Structure 138
7.4 Electrical Properties 140
7.4.1 Nominal Electrical Conductivity 140
7.4.2 Conductivity Enhancement 142
7.5 Composite Applications 143

8 Conclusions **147**

8.1 Summary 147
8.2 Future directions 150
8.2.1 Aerogel improvement, characterization, and applications 150
8.2.2 Improved SWNT composites 152
8.2.3 Theoretical issues 154

Bibliography **154**

List of Tables

2.1 A comparison of room-temperature electrical conductivities for carbon nanotubes and other materials. It is difficult to directly compare individual SWNT conductivity to the conductivity of bulk materials. In SWNTs, the conductance is independent of length and the cross-section of a nanotube is $\sim 10^{-7}$ cm. If no interactions or contact resistances existed between nanotubes, a bundle of nanotubes with a cross section of 1 cm would, by the same token, have a conductance 10^{14} times higher, or 10^{10} S, and be independent of length. In reality, nanotube ropes do not conduct ballistically, and their conductivity is $\sim 10^{4}$ S/cm, an order of magnitude lower than copper. 18

2.2 A comparison of room-temperature thermal conductivities for carbon nanotubes and other materials. For mats of aligned SWNTs, the thermal conductivity is given for the direction of SWNT alignment. Graphite thermal conductivity is anisotropic, and given here for the directions parallel and perpendicular to the graphitic plane. Ranges given for diamond and steel correspond to the thermal conductivities of different types of the material. 21

2.3 A comparison of room-temperature heat capacity [60] and speed of sound for SWNTs [40, 127] to some common materials [97]. These properties determine the phonon contribution to thermal conductivity. 22

2.4 A comparison of the persistence length of SWNT to other polymers. 23

2.5 A comparison of the elastic modulus of SWNTs to other materials. 24

3.1 Types of sonicators, their typical operating parameters, and primary applications [1]. 27

3.2 approximate SWNT dispersion limits for some effective solvents and water/surfactant combinations 33

4.1 Table of percolation thresholds for bond (p_{cb}) and site (p_{cs}) percolation for some lattices where the exact thresholds can be found. Z is the coordination number for each lattice. In site percolation, values followed by (a) are approximate, based on computer simulations. No exact solutions have been found for these lattices [126]. . 79

4.2 Table of some percolation critical exponents in two- and three-dimensions and the Bethe Lattice (d=∞). Exponents given as fractions are exact results. [126] 83

4.3 Table of mathematically equivalent problems for which effective medium theory can be used directly. These steady-state systems are described by the Laplace equation that forms the basis of EMA. 91

5.1 A comparison of some commercially available conductive epoxies. The values quoted are provided by the manufacturer. The tensile strength of Epon 828 epoxy with EpiKure 3234 crosslinker is approximately 73 MPa. 102

5.2 Table of observed thresholds, exponents, and predicted thresholds for the four data sets. All numbers are given in terms of SWNT volume fraction. 120

6.1 A comparison of some commercially available thermally conductive epoxies. The values quoted are provided by the manufacturer. 123

6.2 Table of thermal conductivity enhancements and calculated interfacial resistances. Enhancements are quoted for 1 wt% nanotube loadings, except for Ref [30], which is quoted for 1 vol% SWNT. 129

7.1 Summary of some properties of carbon [114, 115] and silica [66] aerogels 132

List of Figures

2.1 a) The chiral vector, $\mathbf{C}_N(n,m)$, is defined in terms of the unit vectors $\mathbf{a_1}$ and $\mathbf{a_2}$. Directions of the chiral vectors for "armchair" and "zig-zag" nanotubes are shown. b)The chiral vector, $\mathbf{C}_N$, of a "chiral" nanotube and the corresponding translation vector $\mathbf{T}$ are shown. Shaded area denotes the unit cell of the nanotube. The direction of the long axis of the resultant nanotube is also shown. 7

2.2 Examples of zig-zag, chiral, and armchair SWNTs 8

2.3 A now classic TEM image of the cross section of a SWNT rope from ref. [145] showing the crystalline order of the SWNTs inside. Scale bar is 10 nm. 9

2.4 Lennard-Jones potential describing the van der Waals interaction between two carbon atoms in adjacent graphene planes. 10

2.5 Schematic diagrams for common SWNT synthesis methods 11

2.6 Electronic properties of a $(4, 2)$ nanotube from reference [80] a) Constant-energy contours of the valence and conduction bands of graphene in the hexagonal first Brillouin zone. The bands are degenerate at six K points. Dark black lines represent the cutting lines of allowed wave vectors in the $(4, 2)$ nanotube. b) Band structure of the (4,2) nanotube obtained from zone-folding of the cutting lines in (a). $\mathbf{T}$ is the translation vector of the nanotube that defines the unit cell. c) The electronic density of states of the $(4, 2)$ nanotube determined from the band structure shown in (b). Note the discrete spikes known as van Hove singularities. 16

2.7 a) and b) are from ref. [35], while c) and d) are from ref. [158]. a) Simulated (10,10) SWNT rope. b)Interactions between adjacent SWNTs in the rope from (a) result in a pseudogap near the Fermi energy (0 eV). In contrast, the density of states for an isolated (10,10) SWNT is nearly constant close to the Fermi energy. c) Simulated T-junction of (5,5) SWNTs. A 15 nN contact force force between the SWNTs causes distortion at the junction. d) Plots of the inter-tube and intratube conductances as a function of contact force and the corresponding intertube distances. Solid (dashed) lines and left (right) y-axis indicate intertube (intratube) conductances. Note that the intertube conductance increases under greater contact force, but the greater distortion of the SWNTs reduces the intratube conductance. . 19

3.1 Chemical formula of NaDDBs surfactant and a schematic of its interaction with a SWNT from Ref. [75]. It is believed that the surfactant forms hemi-micelles on the SWNT surface. 31

3.2 Flowchart of process for dispersing SWNTs in NaDDBs surfactant. 32

3.3 a) Simplified schematic of a Raman Spectrometer. b) Raman spectrum of CVD-grown carbon nanotubes from Thomas Swan (Elicarb SW batch 1713). Radial Breathing modes, D, G, and G' bands are depicted c) Schematic representation of the vibrational modes involved in the RBM and G bands of the nanotube Raman spectrum. 35

3.4 a) Schematic of Thermogravimetric Analysis (TGA) apparatus. Two identical balance beams and pans are housed inside a furnace. The temperature of each pan is monitored with a thermocouple. Powdered sample is placed in one pan, while the second pan serves as the reference. Air (or another gas, depending on the application) is flowed through the sample area, while the furnace temperatrure is slowly raised. b) TGA results for a 3 mg sample of CVD-grown nanotubes from Thomas Swan (Elicarb SW batch 1713). The temperature is ramped from room temperature to 900°C at 3°C/min. The ratio of the sample mass to the initial sample mass is plotted vs. temperature. The carbonaceous material vaporizes around 600°C, which is typical of a high-quality nanotube sample. Above 800°C less than 5% of the initial mass remains. This remaining mass is typically attributed to the metal catalyst particles. 39

3.5 a) Schematic of a tapping-mode atomic force microscope. An oscillating (tapping) cantilever is scanned across the substrate, and is deflected up or down as it encounters topological features, such as a nanotube. A laser reflected from the top surface of the cantilever is imaged onto a split diode detector that can sensitively monitor the position of the laser. b) Electron microscope images of AFM tips. c) Tapping-mode AFM image of SWNTs deposited from DMF solution onto an HMDS-treated silicon wafer. 42

3.6 A thin hydrophilic oxide layer is typically present on silicon (top). Treatment with Hexamethyldisilazane (HMDS), middle, can render it hydrophobic. Nitrogen in the HMDS molecule reacts with two hydrogens (possibly from the surface layer), splitting the molecule and creating ammonia. Each half of the original molecule bonds to oxygen atoms on the surface with the methyl groups pointing up, rendering the surface hydrophobic. 44

3.7 Holey carbon TEM grids. a) some patterns of the micromachined support disks. b) Optical (left) and SEM (center and right) images of the carbon films on holey carbon TEM grids. These examples feature microfabricated films with regular hole patterns. c) TEM image of a MWNT. Individual graphene layers are clearly visible. d) TEM image of a cluster of SWNTs over a hole on a holey carbon grid. The supporting carbon film is visible in the top right corner of the image. 49

3.8 Energy Dispersive X-ray spectroscopy (EDX). a) The $K\alpha_2$ transition in carbon. A void created in the K electron shell is filled by an electron from the L shell, releasing an X-ray in the process. The quantum numbers, n, l, and j that correspond to the energy levels are also shown. b) Electrons are ejected from the sample by a beam of high-energy electrons, such as those from a scanning electron microscope, emitting x-rays in the process. An EDX X-Ray detector is mounted above the sample. c) Example of an EDX spectrum of NaDDBs-coated SWNTs. The presence of carbon, oxygen, sodium, and sulfur peaks are consistent with the composition of the surfactant. 53

3.9 Near-IR Absorption spectra of SWNTs from Ref. [76]. a) Absorption spectra of two SWNT samples of different purity. The S_{11}, S_{22}, and M_{11} peaks are evident. The solid line is the sample with a higher purity. b) Quantitative analysis of the S_{22} peaks of three different samples to determine the content of the carbonaceous impurities. The reference sample is on the left and is assumed to be 100 % pure. The middle and right samples are compared against the reference sample to obtain relative purity (see text). 55

3.10 Fluorescence map of SWNTs in a sodium dodecyl sulfate suspension from reference [80]. Each peak represents a distinct (n,m) nanotube species. 57

3.11 a) Schematic of x-rays scattered from a crystal structure. X-rays incident on successive crystal planes interfere constructively when the Bragg condition, $2d\sin(\theta) = n\lambda$, is satisfied, forming a bright spot in the diffraction pattern. b) Typical ring diffraction pattern from a powder scattering measurement. 59

3.12 a) Raw SAXS data from a critical-point dried nanotube aerogel (0.75 wt% CVD CNT, 0% PVA, ~5 wt% catalyst) from which the surfactant has been removed with water. b) log-log plot of the intensity profile vs. scattering vector, Q, of the image in (a). The plot is nearly linear with a slope of -2.7. Bottom part of the plot shows the residuals of the fit. 62

3.13 Log-log plot of SAXS intensity profiles for NaDDBs-dispersed HiPco SWNT gels. The catalyst content is < 0.7 wt%. Q range corresponds to real-space lengths of ~5.5 to 250 nm. Throughout most of this range (~17-250 nm), the scattering intensity falls off as Q^{-2}, which is inconsitent with hard-rod scattering. This may be due to interference from the surfactant or to catalyst particles. 63

3.14 SANS scattering of SWNT dispersion from Reference [163]. Data is for a 0.1% HiPco SWNT solution dispersed with 1% NaDDBs surfactant. The curve reflects the scattering intensity after subtraction of the surfactant contribution, with the assumption that some surfactant is adsorbed onto the nanotubes while some remains as free micelles in solution. Dashed and solid lines reflect extreme assumptions of no excess surfactant in solution and no surfactant on nanotubes, while solid circles represent the best intermediate assumption. The curve reveals a Q^{-1} scaling for Q between 0.003 and 0.02 Å^1 (31-160 nm) and Q^{-2} scaling at lower Q (larger lengths). 64

3.15 Flowchart of a typical purification procedure. After purification, the nanotubes may be dispersed according to the procedure in Fig. 3.2. 67

3.16 Setup for performing acid reflux during carbon nanotube purification. 69

3.17 Three TGA curves obtained during purification of HiPco batch R0519. 71

4.1 Percolation of particles placed randomly in a (zero-gravity) box. As the particle density increases, clusters of particles begin to form. Above a certain particle concentration p_c, a continuous path of particles forms through the matrix. If the particles are electrical conductors, a current will flow from one end of the box to the other above p_c. Below this threshold concentration, the material is insulating. . 76

4.2 Some lattices for which exact solutions of percolation theory exist. Z denotes the coordination number of each lattice. 78

4.3 a) A rod of length L and diameter d capped by a hemisphere at each end. b) and c) The excluded volume for two identical rods depends on the relative orientation of the rods. For parallel, cylindrical rods (b), the excluded volume is a cylinder with volume $V_{excl\|} = (4\pi/3)d^3 + 2\pi(d)^2(L)$, while for perpendicular rods (c), $V_{excl\perp} = (4\pi/3)d^3 + 2\pi d^2 L + 2dL^2$. (d) When one of the rods is oriented at an angle θ, the excluded volume is $V_{excl}(\theta) = (4\pi/3)(d)^3 + 2\pi d^2 L + 2dL^2 \sin(\theta)$. . 84

4.4 a) Schematic representation of how"Sticky" rods initially below a critical concentration (left) can cluster together to form a network (right). b) For homogeneously distributed attractive rods, a continuous network can form as long as there is at least one rod of length L per spherical volume $\nu = (4\pi/3)(L/2)^3$. 88

4.5 Concentration regimes for hard rods in solution, according to Doi-Edwards theory. 89

4.6 Predicted conductivity of CNT composites based on percolation theory, shown here on a semi-log plot. 90

4.7 a) Schematic representation of the effective medium theory description of our SWNT-epoxy composites. The inhomogeneous composite (left) contains epoxy of thermal conductivity κ_{epoxy} and nanotubes, here approximated as ellipsoidal inclusions, with thermal conductivity κ_{SWNT} and thermal interface resistance (Kapitza resistance) R_K. Effective medium theory approximates this system as a homogeneous medium with effective thermal conductivity κ_{eff} (right). b) The thermal conductivity perpendicular and parallel to each nanotube is considered in the formulation. 92

5.1 a) Epon 828 is frequently made by reacting Bisphenol-A with epichlorohydrin. b) The structure of Epon 828 resin consists of a short linear chain of bisphenol-a groups terminated by epoxide rings at either end. The aliphatic amine crosslinker used in our composites (EpiKure 3234) contains two primary and two secondary amine groups. Each primary amine can ideally react with two epoxide rings, while each secondary amine can react with one epoxide group. c) schematic of the reaction between Epikure 3234 amine crosslinker and epoxide rings. Each molecule of EpiKure 3234 can react with up to six epoxides, but usually the molecules become immobile before all groups are able to react (see text). 105

5.2 Flowcharts describing the preparation of a dilute SWNT-DMF dispersion and the process for making composites. 107

5.3 Process for making composites. a) A dilute dispersion of SWNTs in DMF. b) Sonicating epoxy resin. 0.5 g of epoxy resin in placed in the white crucible at the center of the picture. The sonicator bath is heated by circulating hot water through a coiled copper tube placed in the sonicator bath. A part of the heating coil is seen near the top of the picture. The sonicator bath is covered with a plexiglass cover to reduce evaporation of the bath water. A hole is cut in the middle of the cover to accommodate the crucible, such that the bottom of the crucible rests $\sim$1 cm below the surface of the bath water. The dilute suspension from (a) is slowly added to the sonicating resin in 1 mL additions each 30 minutes, until the desired concentration is reached. c) A 1 mL plastic syringe (inner diameter 4.7 mm) is used as a mold for the curing resin. The syringe tip is cut off, and both sides are sealed by a rubber syringe piston. In sonicured composites, the full syringe is placed back into the sonicator while the epoxy cures. d) The cured epoxy is cut into cylindrical pieces on a diamond saw. 108

5.4 (a) In a two-point configuration, the resistance of a sample, R is measured by applying a voltage across the sample and measuring the resultant current (or by applying a current and measuring the voltage drop) using two contact points on the sample. If the contacts are not ideal, an additional resistance, R_c, exists, and the measured resistance will be $R + 2R_c$. (b) In systems where R_c is significant, a four-point configuration can be used. A known current I is applied across the sample, and a separate set of electrodes is used to read the voltage drop. Although a contact resistance, R_c is present at each contact, the true resistance of the sample, R, can be obtained (see text). 111

5.5 Two-point and four-point I-V curves for a non-sonicured HiPco SWNT composite at 1.6×10^{-4} SWNT volume fraction show a typical response of our samples. The insets show composite samples mounted for two- and four-point conductivity measurements. At a given current, the measured voltage in two-point measurements is significantly higher than in four-point due to both contact resistance and a larger separation between electrodes. 112

5.6 A two-point alternating-bias method is used to measure highly resistive composite samples. The applied voltage is alaternated between positive $(+V)$ and negative $(-V)$ values, and the measured current in each step approaches an asymptotic value. The method takes into account capacitative effects as well as a drifting background (dashed line) to establish the resistance of the sample, as explained in the text. 113

5.7 (a) Photographs of composites. SWNT volume fractions, from left to right, are 2.6×10^{-5}, 5.2×10^{-5}, 1.0×10^{-4}, and 1.5×10^{-4}. (b) - (f). Images of composites (SWNT volume fraction 2.1×10^{-4}). Information about SWNT distribution in the composites can be obtained from transmitted light microscopy through thin ($\sim$300 μm) slices ((b),(c), and (f)), and from scanning electron microscopy (SEM) of fractured surfaces ((d) and (e)). (b) In a *non-sonicured* sample, dark and bright regions correspond to high and low SWNT concentrations, respectively. (d) In SEM images of the same *non-sonicured* composite, SWNT ropes (white strips) appear in $\sim$10 μm clusters on the surface. Here, the ropes are present only in the lower left quadrant of the field of view. (c) The more uniform gray color in this *sonicured* composite implies a more uniform SWNT distribution than in (b). (e) SEM image of a *sonicured* sample shows that SWNT ropes are distributed more uniformly across the fractured surface than in (d). (f) Dense aggregates are seen in a *non-sonicured* composite made from a more concentrated SWNT/DMF starting dispersion at 0.04 wt% (see text). (g) Tapping mode AFM image of laser-oven SWNTs adsorbed over 30 minutes onto an HMDS treated silicon wafer from a well sonicated, dilute DMF-SWNT suspension. 117

5.8 Conductivity σ as a function of SWNT volume fraction ϕ for non-sonicured and sonicured laser-oven and HiPco samples. The vertical lines on the charts indicate approximate transitions from dilute to semi-dilute regimes (wavy) and semi-dilute to concentrated regimes (solid). Each point on the plot represents a separately made composite. The observed scatter in conductivity is likely caused by small variations in processing conditions between samples. In contrast, the conductivities of different sections of the same sample were never more than 50% of each other. Filled circles represent four point measurements. Open circles depict two point alternating bias measurements. Points in shaded areas are below the baseline of our equipment. Connecting curves reflect the predicted behavior according to the best fits for the observed threshold ϕ_c and the exponent s. Insets show plots of $\log(\sigma)$ as function of $\log(\phi - \phi_c)$ for the same data sets, where multiple points at the same concentration have been binned prior to fitting. Best fit lines determining ϕ_c and s are shown. 119

6.1 Photograph of thermal conductivity measurement setup 126

6.2 Inset (a) depicts the measurement setup. The main plot shows the applied current and corresponding temperature response of the top and bottom plates. In inset (b), the slope of the applied power (I^2R) versus the temperature differential (ΔT) gives the thermal conductance of the sample, from which thermal conductivity is extracted. 127

6.3 Thermal conductivity of DMF-processed and surfactant-processed samples. The fits shown assume SWNT dimensions (L = 167 nm, d = 1.1 nm), thermal conductivities of SWNTs (κ_{swnt} = 3000 W/m-K), and epoxy (κ_m = 0.198 W/m-K). The thermal interface resistance (R_K) is the free fit parameter. ϕ is known to within $\pm$ 10 %. 128

7.1 Nanotubes used in the experiment, Elicarb SW batch K1713 from Thomas Swan, Inc. are characterized by thermogravimetric analysis (TGA) and Raman spectroscopy. a) TGA analysis of the material reveals a metallic impurity content of <5 wt%. b) Raman spectroscopy (514 nm laser) exhibits some radial breathing modes (RBMs) at wavenumbers >250 cm^{-1}, suggesting the presence of DWNTs [13]. 133

7.2 Polyvinyl Alcohol (PVA) is made by fully or partially hydrolyzing Polyvinyl Acetate, a hydrophobic polymer that is the main component of common household "white glue." In our experiments we use fully (100%) hydrolized PVA. Partially hydrolized PVA contains some acetate groups and is less soluble in water. 134

7.3 Elemental analysis by Energy Dispersive X-ray Spectroscopy (EDX) is used to qualitatively determine the effectiveness of the water bath for removing surfactant in PVA reinforced CNT aerogels. a) In an unwashed, unreinforced aerogel sample that contains sodium dodecylbenzene sulfonate (NaDDBs) surfactant, the elements carbon, oxygen, sulfur and sodium are evident. These elements are consistent with the composition of the surfactant. b) Aerogel sample after being placed in a 0.25 wt% PVA solution for three days at room temperature. The mobile sodium ion is effectively removed, but the presence of sulfur suggests that some surfactant remains. c) Aerogel sample placed in a 0.25 wt% PVA bath at 90°C for three days shows only trace amounts of sulfur and no sodium, suggesting the surfactant is effectively removed. The main peaks here are carbon and oxygen, likely from the nanotubes and PVA polymer. 135

7.4 Principles of critical point drying and freeze drying on a generic phase diagram. By starting with a wet gel, there are in general three ways to remove the background liquid by transitioning to the gas phase. The simplest is to evaporate the liquid, directly transitioning from liquid to gas, as in (a). However, as the liquid evaporates, surface tension at the liquid/gas interface causes the gel network to collapse. To preserve the network structure, the liquid/gas interface is avoided. b) In freeze-drying, the sample is flash frozen, and placed under vacuum. The temperature is then raised to allow the ice to sublimate. c) In critical-point drying, the pressure and temperature are raised above the critical point, where liquid and gas cease to be separate phases. Once above the critical point, the pressure is slowly released, and the sample is subsequently cooled. 136

7.5 Zone refinement is seen in this optical image of fluorescently-labeled DNA being frozen in a thin glass cell. a) ice "fingers" (large dark features) grow through the liquid and push DNA out of the way. Note the brighter fluorescence, i.e., higher DNA concentration, at the liquid/ice interface. Field of view is ~600 μm. b)As the sample solidifies, the DNA is concentrated in the narrow bands between the ice fingers. 137

7.6 Images of aerogels. a) Macroscopic pieces of 7.5 mg/mL CNT aerogels. Pristine CNT aerogel (left) appears black, while the aerogel reinforced in a 1 wt% PVA bath (right) is slightly gray. b) Three PVA-reinforced aerogel pillars (total mass = 13.0 mg) supporting 100 g, or ~8000 times their weight. c) SEM image of a critical-point dried aerogel reinforced in a 0.5 wt% PVA solution (CNT content = 10 mg/mL) reveals an open, porous structure. d) High-magnification TEM image of an unreinforced aerogel reveals small-diameter CNTs arranged in a classic filamentous network. 138

7.7 a) Freeze-dried aerogels sometimes have a second porosity lengthscale of order tens to hundreds of μm, as seen in this SEM image of an unreinforced aerogel (7.5 mg/mL CNT content. b) The large pores in freeze-dried aerogels are a result of the growth of ice crystals during freezing, and can have remarkably regular patterns, including the cellular structures seen here. c) closeup of a honeycomb structure. d) Individual CNTs are seen here compressed into a thin layer due to the pressure of the ice crystals. Many other morphologies are also observed in freeze-dried samples. 139

7.8 a) Densities of some critical-point dried aerogels are plotted vs. the PVA bath concentration. The density increases with increasing PVA bath concentration and depends on the CNT content of the aerogel. b) PVA content in the aerogels can be estimated by subtracting the CNT weight from the total weight of the aerogel sample. The CNT weight is determined to an accuracy of ~10% from the CNT content in the precursor gel and the measured sample volume. The average PVA content ranges between 15 to 50 mg/mL, which corresponds to PVA to CNT weight ratios of between 1 and 6. The observed variation in aerogel PVA content with PVA bath concentration could be a result of deposition of more than one PVA layer on the nanotubes and/or deposition of residual PVA from the solution during solvent exchange. 141

7.9 Conductivities of as-prepared CNT aerogel samples. a) Dependence of CNT content on the conductivity. The bath PVA content is fixed at 1 wt%. b) Dependence of aerogel conductivity on PVA content. CNT content is fixed at 7.5 mg/mL. Inset depicts the electrical connections to an aerogel sample. 142

7.10 (a) Discrete current pulses, I_p, applied across a sample, as shown in this schematic, improve the electrical conductivity of PVA reinforced CNT aerogels. (b) A 15 ms, 0.5 mA current pulse (depicted by vertical gray line) is applied to a 13.3 mg/mL CNT critical-point dried sample reinforced in a 0.5 wt% PVA bath. The conductivity improves by $\sim 2\times$ after the pulse, and remains at the new level indefinitely. (c) A 15 ms, 100 mA current pulse is applied across the same sample, after the sample has undergone repeated current pulses and the starting resistance is much lower. Although the current here is much higher, conductivity improves only transiently, presumably due to heating, and returns to the original value in a matter of seconds. (d) and (e) show the full breakdown history of this sample. (d) Pulsing current is linearly increased up to 100 mA (pulse duration is always 15 ms; pulses are spaced more than 30s apart). Each point represents a discrete current pulse. Arrows point to the pulses depicted in (b) and (c). (e) The corresponding steady-state conductivity, measured 30s after each pulse. Notice, the conductivity improved by several orders of magnitude after repeated pulsing. 144

7.11 (a) Aerogel sample (7.5 mg/mL CNT, 0.5% PVA bath) backfilled under vacuum with Epon 828 epoxy resin and EpiKure 3234 cross-linker. (b) The sample is removed from the resin and left to cure. Fracturing the sample reveals that the infiltration of the sample by the resin was complete; no voids or bubbles are evident. 145

Chapter 1

Introduction

Since their discovery in 1991 [70], carbon nanotubes have been among the most widely studied materials in science. They are an integral part of the current boom in nanotechnology research and are widely acclaimed for having the potential to revolutionize composite materials, electronics, energy storage, and biomedicine, among others. Their appeal stems largely from their unique atomic structure and the remarkable physical properties that follow from it. These properties, described in some detail in chapter 2 of this thesis, include exceptionally high thermal conductivity and strength, electrical conductivities that can range from semiconducting to metallic depending on structural features such as diameter and chirality, and the ability to carry high currents without degrading [38].

Research on single wall carbon nanotubes (SWNTs) can be roughly divided between studies of individual SWNTs and studies of SWNT ensembles and networks. In the former case, the intrinsic properties of individual carbon nanotubes are explored; these properties are critical for applications like molecular electronics. In carbon nanotube networks, on the other hand, the nature of the nanotube junctions and interactions between the nanotubes and their environment also play a

critical role in the properties of the resultant material. This thesis describes our work with carbon nanotube networks in SWNT/epoxy composites and in novel carbon nanotube aerogels. The research addresses the seemingly contradictory goals of both dispersing the nanotubes in a matrix and creating a connected network at the same time. Much of this work has been published [21–23].

Our work is motivated in part by the significant potential of carbon nanotubes for creating so-called "multifunctional materials." Such materials possess several properties, or functions, that are usually not found together in a single material. For example, light-weight, high-strength epoxies that are also electrically conductive are aggressively sought out by the aerospace and semiconductor industries. The inclusion of very small quantities of carbon nanotubes into epoxy can render it electrically conductive, without diminishing the otherwise desirable properties of the epoxy [21]. However, many challenges exist. Of primary concern in this thesis is the fact that single- and few-wall carbon nanotubes are strongly aggregating and are thus difficult to disperse and stabilize in most materials. Achieving the desired properties in a bulk composite depends heavily on the successful dispersion of nanotubes within the matrix and, further, on the arrangement of the nanotubes in the matrix, i.e., the morphology of a continuous nanotube network. We present data to show that these factors depend strongly on the methodology used to create the networks, and we offer some solutions for achieving greater control over network formation and the resulting properties.

Carbon nanotubes are difficult materials to work with. Generally, the carbon nanotube material available today contains high levels of impurities; in addition their dispersions are typically composed of nanotubes of various diameters, lengths, and chiralities - and therefore various electrical and thermal properties. Purification and characterization of the nanotubes are among the top priorities for any project involving carbon nanotubes. To date, there is no effective way to make

monodisperse carbon nanotubes or to fractionate them in sufficient quantities for use in composites. The first two chapters of this thesis provide a general background about nanotubes (Chapter 2) and the various tools and methods that have been developed to work with them, including methods for dispersing, purifying and characterizing them (Chapter 3).

Chapter 4 provides a theoretical framework for explaining the properties of inhomogeneous materials such as nanotube composites. Two approaches, percolation theory and effective medium theory, are presented. Percolation describes the properties of particle clusters and the onset of a continuous network, while effective medium theory uses a mean-field approach to describe the bulk properties of microscopically inhomogeneous materials. Percolation is appropriate for systems in which the particles have very dissimilar properties from their surroundings, as is the case with electrical conductivity of nanotubes in a highly insulating epoxy matrix. Effective medium theory, on the other hand, works better for describing composite material properties when the constituents are more similar to each other, as with the thermal conductivity of nanotubes in an epoxy matrix that is also thermally conductive.

The remainder of the thesis describes our work with SWNT/epoxy composites and carbon nanotube aergoels. In the first investigation, we explore the effects of SWNT aspect ratio and dispersion homogeneity on the electrical conductivity of the composite. We find that higher SWNT aspect ratios and, surprisingly, more inhomogeneous dispersions reduce the amount of SWNTs that are needed to obtain conductive composites. By using SWNTs of high aspect ratio and dispersing them with some inhomogeneity in the epoxy, we create conductive composites at the lowest SWNT concentrations reported to date [21]. We next explore the thermal conductivity of these composites as a function of the preparation method and we extract thermal interfacial resistance [23]. We find that preparation plays a critical role in determining the thermal conductivity of the composites. In

particular, using surfactant to aid in SWNT dispersion enhances the ability to achieve high SWNT volume fractions in the epoxy, but also increases the thermal interfacial resistance between the nanotubes tenfold. As a result, composites with comparable SWNT content are more thermally conducting when no surfactant is used.

The process used to synthesize our epoxy composites is described in Chaper 5. Our novel approaches use very dilute DMF-dispersed SWNTs and NaDDBs stabilized aqueous SWNT dispersions to achieve improved SWNT homogeneity in the matrix over previous work [5, 15, 16, 19, 41,51,54,67,84,92,98,108,111,113,120,121,129,134,140,165]. The SWNTs used in these experiments are purified to a high degree, which also enables us us to draw more meaningful conclusions about the effects of SWNT volume fraction and aspect ratio on the electrical and thermal conductivities of our composites. Our work gives insight into the effects of processing on the SWNT network homogeneity and conductivity in SWNT epoxy composites. In chapter 5, we show that certain types of inhomogeneities in the SWNT dispersion are advantageous, resulting in conductive composites at lower SWNT filling fractions than a homogeneous dispersion. This result enables us to create composites that are conductive at very low SWNT volume fractions. A simple model based on percolation theory (detailed in chapter 4) is used to illustrate how the strongly interacting SWNTs can form continuous networks at concentrations lower than those predicted by percolation theory for non-interacting rods. The threshold concentrations all occur in the semidilute SWNT regime, which is consistent with our simple model.

Chapter 6 details our thermal conductivity measurements of the SWNT/epoxy composites. Although the thermal conductivity of individual SWNTs is very high [38], we find that the thermal conductivity of the SWNT networks in our composites is severely limited by the interfacial thermal resistance at the SWNT junctions. We analyze our results using effective medium theory [105],

which enables us for the first time to extract a value for this resistance for a solid composite. We find that this interfacial resistance (also known as Kapitza resistance [106]) is variable; a ten-fold increase is observed when surfactant is used in making the composites over composites made from DMF SWNT suspensions. We attribute this difference to thermal damping by the surfactant.

In Chapter 7 we introduce carbon nanotube aerogels, a new type of material with unique properties and potentially important applications in a number of fields [22]. These ultralight, highly porous materials are self-supporting, three-dimensional networks of carbon nanotubes created by critical-point drying and freeze drying of aqueous nanotube gels. By using an optimized process [75] to disperse nanotubes in water with surfactant, the nanotubes in the aerogels are not bundled into large "ropes", but individually arranged in a classical filamentous network structure. A well-understood gelation process [64, 65] allows us to optimize network formation, control the nanotube concentration, and add reinforcing agents if desired. The aerogels are electrically conducting and can be very strong upon reinforcement with polyvinyl alcohol (PVA) polymer. We characterize the electrical conductivity of the aerogels with respect to the nanotube and PVA content.

Chapter 2

Overview of carbon nanotubes

2.1 Nanotube structure

Carbon nanotubes are cylindrical carbon macromolecules made of rolled graphene, or sheets of sp^2 hybridized carbon atoms arranged in a planar "honeycomb" structure. Unlike carbon fibers and filaments, carbon nanotubes have well-defined atomic structures that give rise to their unique properties, such as high strength, unique electrical properties, and high thermal conductivity. Nanotubes comprised of a single layer of graphene are called single-wall carbon nanotubes (SWNTs), whereas those that have concentric multiple layers of graphene are called multi-wall carbon nanotubes (MWNTs). Typically SWNTs have diameters of order 1 nm, and lengths of order 100 nm to several μm. MWNT have much larger diameters of tens to hundreds of nanometers. Intermediate to these are the so-called few-walled carbon nanotubes (FWNT) that have only a few layers, such as double-wall carbon nanotubes (DWNT). The latter share many properties with SWNTs, including bulk electrical [156] and tensile [95] properties, similar size and aspect ratio.

A graphene sheet can be arranged in various configurations to form a SWNT, giving rise to

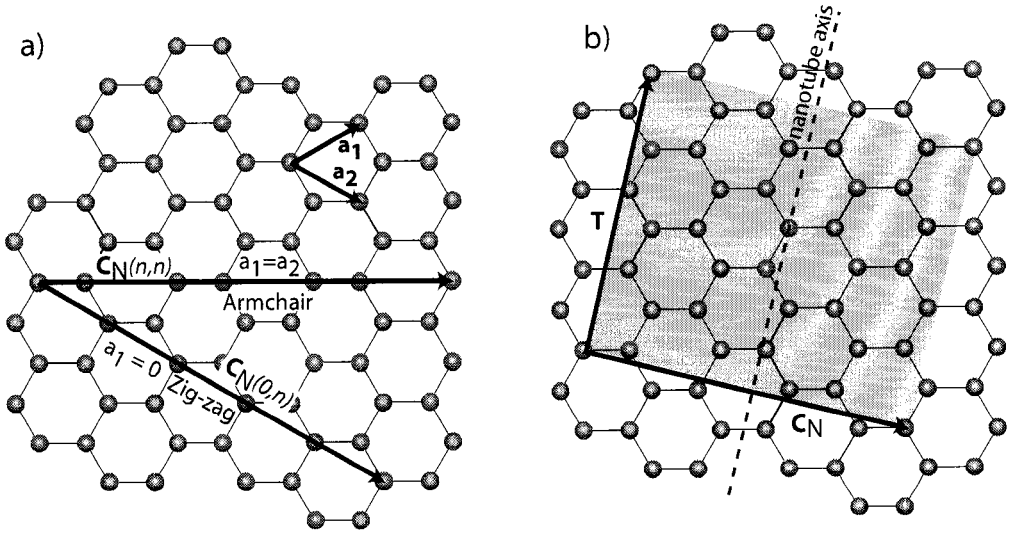

Figure 2.1: a) The chiral vector, $\mathbf{C}_N(n,m)$, is defined in terms of the unit vectors $\mathbf{a_1}$ and $\mathbf{a_2}$. Directions of the chiral vectors for "armchair" and "zig-zag" nanotubes are shown. b)The chiral vector, $\mathbf{C}_N$, of a "chiral" nanotube and the corresponding translation vector $\mathbf{T}$ are shown. Shaded area denotes the unit cell of the nanotube. The direction of the long axis of the resultant nanotube is also shown.

nanotubes of different sizes and properties. These configurations, and the resulting SWNTs, are fully described by the chiral vector, $\mathbf{C}_N(n,m)$, where n and m are integers (see Fig. 2.1(a)). In a nanotube, the graphene sheet is rolled in the direction of the chiral vector such that the head and the tail of the vector meet at one point. Thus, the magnitude of the chiral vector gives the nanotube circumference, while the vector's direction in the graphene plane describes the chirality of the SWNT, or the direction in which the graphene sheet is rolled with respect to the carbon honeycomb structure [39]. The magnitude of the vector is given by $c = a\sqrt{n^2 + m^2 + nm}$, where a is the length of the unit vector, i.e., $a = \sqrt{3}a_{C-C} = 2.41$ Å, where $a_{C-C} = 1.44$ Å is the spacing between carbon atoms in the lattice. The chirality of the nanotube is described by the indices n and m. If $m = 0$, the SWNTs are called "zigzag". If $n = m$, the SWNTs are called "armchair". Otherwise, they are called "chiral". Examples of these are shown in Fig. 2.2. Another quantity of interest is the translation vector, $\mathbf{T}$, as shown in Fig. 2.1(b), which is perpendicular

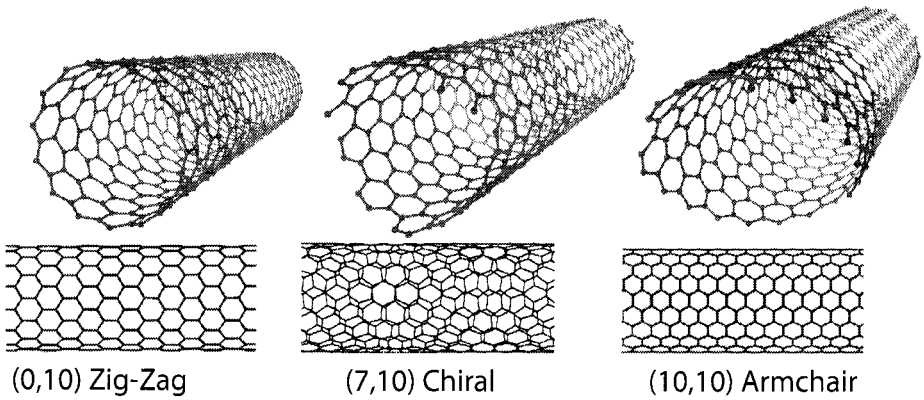

Figure 2.2: Examples of zig-zag, chiral, and armchair SWNTs

to the chiral vector, and whose length indicates the periodicity of the hexagonal pattern along the axis of the nanotube. In the unrolled graphene plane, the rectangle described by the chiral and translational vectors define the unit cell of the nanotube.

SWNTs tend to aggregate in ropes consisting of tens to hundreds of nanotubes in cross-section. The ropes have diameters of tens of nanometers and can be many microns in length [145]. The SWNTs inside a rope are packed in a crystalline hexagonal order, as seen in Fig. 2.3. The ropes are held together by strong van der Waals forces between the SWNTs.

The van der Waals interaction between two atoms is approximately modelled by the Lennard-Jones (also known as LJ or 6-12) potential,

$$u(x) = -\frac{A}{x^6} + \frac{B}{x^{12}} \tag{2.1}$$

where $u(x)$ is the potential energy, x is the separation between the atoms, and A and B are constants. A simple model based on the lattice spacing of carbon atoms in graphene predicts that, $A = 15.2$ eVÅ^6 and $B = 24.1 \times 10^3$ eVÅ^{12} for a pair of atoms in adjacent graphene planes. A plot of this potential is shown in Fig. 2.4. The potential minimum occurs when the atoms are are

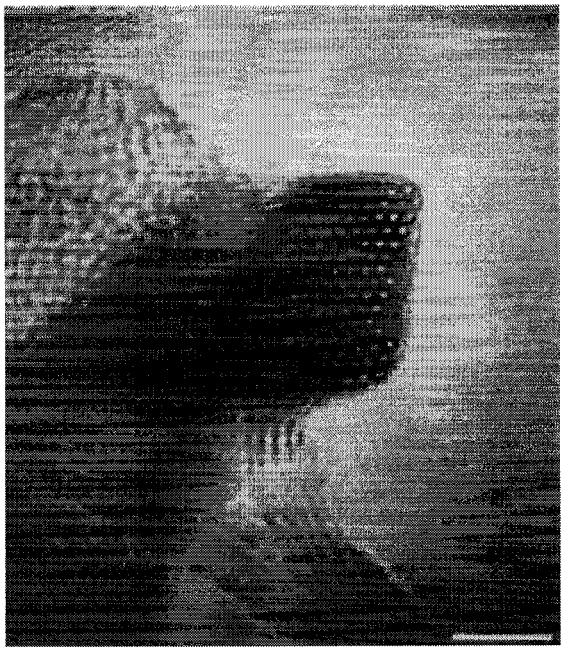

Figure 2.3: A now classic TEM image of the cross section of a SWNT rope from ref. [145] showing the crystalline order of the SWNTs inside. Scale bar is 10 nm.

separated by 3.83Å, and the well depth is 2.39 meV per atom pair [49]. The actual separation of graphite planes, as determined by x-ray scattering and TEM imaging, is 3.347 Å [97], so the values obtained from the simple model are only approximate.

For carbon nanotubes, a continuum model based on the LJ potential, which assumes a uniform electron distribution over the surface of the nanotube is sometimes used. This model may be more appropriate for nanotubes in a rope, where the graphene planes of adjacent nanotubes with different chiralities are not neccessarily in register with each other. The solution requires numerical integration. The model predicts a typical separation between the surfaces of SWNTs in a rope to be ~3.13 Å and a well depth of 95 meV/Å (~37 kT/nm) [49]. For comparison, the same model predicts a well depth of 15.36 meV/Å^2 and equilibrium spacing of 3.414 Å for graphene-graphene interactions. Although the values are approximate, it is evident from the model that very strong van der Waals interactions exist between nanotubes, and this is consistent with experimental

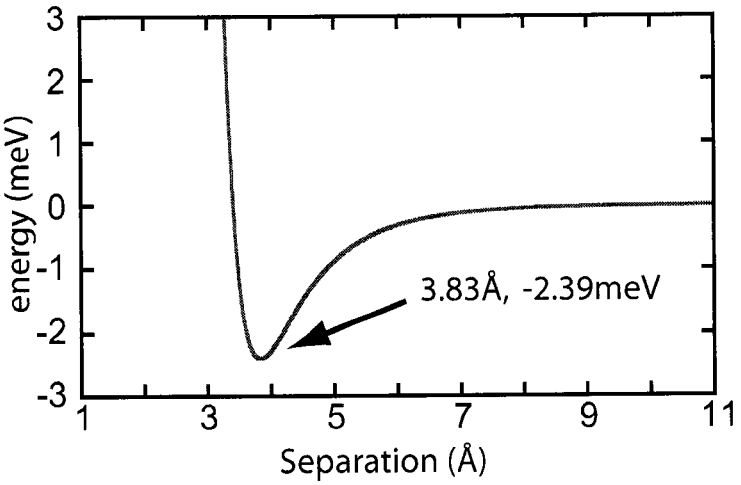

Figure 2.4: Lennard-Jones potential describing the van der Waals interaction between two carbon atoms in adjacent graphene planes.

observations.

These strong van der Waals interactions between SWNTs are in some sense a main theme in this thesis. The attraction makes the ropes very stable and difficult to disperse into individual SWNTs, but it is also responsible for the subsequent network formation and the properties that follow. Much of the original work presented here uses the van der Waals attraction between SWNTs to create optimal SWNT networks.

2.2 Synthesis of single wall carbon nanotubes

This section describes some common methods used for SWNT synthesis. The SWNTs used in our experiments were made with the Laser-oven, HiPco and CVD methods. The physical dimensions of the SWNTs used in our experiments are also described. Fig. 2.5 shows a schematic for the various synthesis methods.

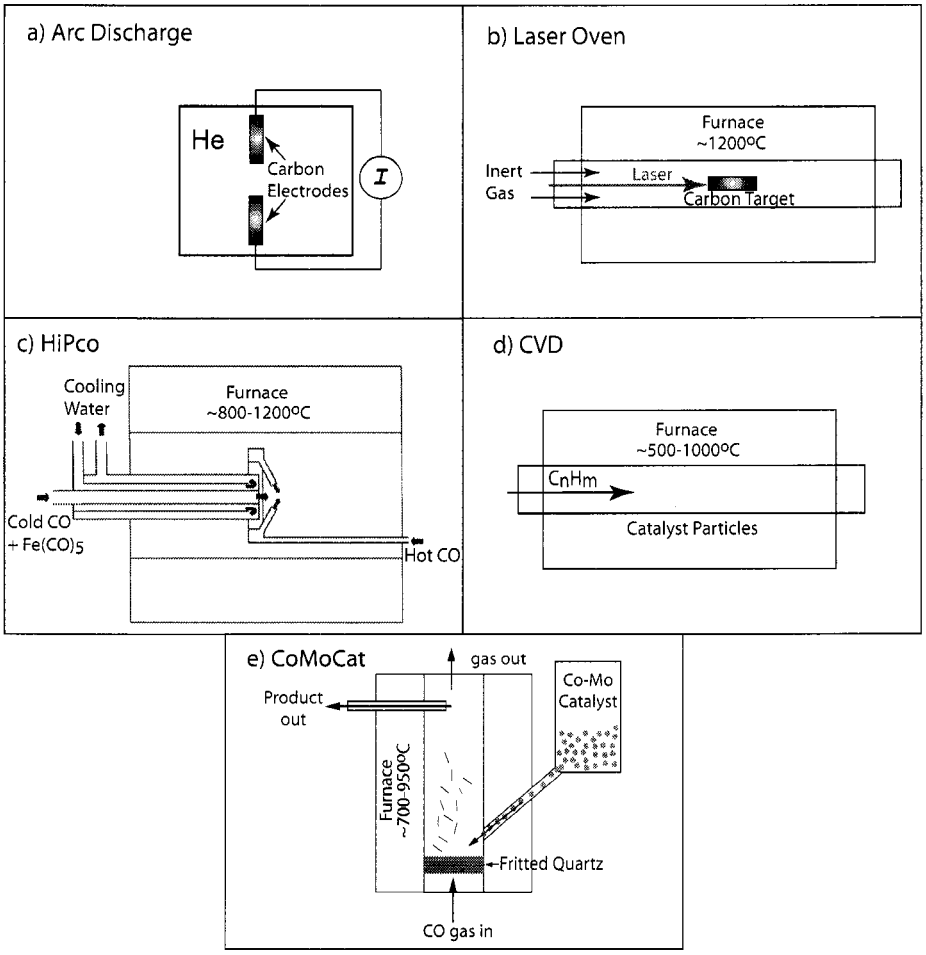

Figure 2.5: Schematic diagrams for common SWNT synthesis methods

2.2.1 Arc discharge

The first carbon nanotubes discovered in 1991 by Sumio Ijima at NEC Laboratory in Japan were multi-walled carbon nanotubes observed in carbon soot produced by the arc discharge method [70]. Soon after, SWNTs were also observed in arc discharge soot by the same group [71]. In the arc discharge method, carbon atoms are evaporated by a helium plasma, created when high currents are passed between carbon electrodes through helium gas (see Fig 2.5(a)). The electrode surfaces reach temperatures of 3000-4000°C, which is near the sublimation temperature of carbon. The method has been improved to obtain better yields of both MWNTs [44] and SWNTs [18, 81]. For

SWNTs, it was found that the presence of metal catalyst particles in the electrodes is required [18]. This has turned out to be true for other SWNT growth methods as well. The arc-discharge method, however, is not frequently used today to produce commercial SWNTs. Other methods, in particular HiPco [112] and more recently CVD, have been found to be cheaper and more scalable.

2.2.2 Laser oven

The first successful method for growing substantial amounts (1-10 g batches) of high quality SWNTS was the laser ablation (A.K.A. laser oven) method [145]. In this method, strong laser pulses are used to ablate a carbon target that also contains 0.5 atomic % of nickel and cobalt (see Fig 2.5(b)). The target is heated to 1200°C in a tube furnace. The produced SWNTs are carried downstream by a flow of inert gas, and collected onto a cold "finger". Once a dominant SWNT synthesis method, the laser-oven approach is difficult to scale up, and has been largely displaced by HiPco and CVD processes.

Laser oven SWNTs supplied by Tubes@Rice are used to make some of our SWNT/epoxy composites. Our AFM characterization (see section 3.2) of these SWNTs after purification, annealing, and dispersion, reveals that they have average length $L = 516 \pm 286$ nm, and average diameter, $d = 1.35 \pm 0.15$ nm [75].

2.2.3 High pressure decomposition of carbon monoxide (HiPco)

Also called "gas phase catalytic growth" [112], the HiPco method is currently one of the most common methods used for growing SWNTs. In this method, Carbon Monoxide gas, which provides the carbon material, is injected at high pressure (up to 10 Atm) into a 800-1200°C furnace (see

Fig 2.5(c)). Iron catalyst particles are also simultaneously created in the furnace by thermal decomposition of (gaseous) iron pentacarbonyl. SWNTs grow and are collected from the gas phase, enabling a continuous and scalable manufacturing process. In this method, high pressure is required to provide sufficient carbon quantities, since carbon monoxide is a very stable molecule and thus not a very efficient source of carbon. However, since CO does not spontaneously decompose without the catalyst particles, it results in cleaner SWNT material without much amorphous carbon. HiPco SWNTs used in our SWNT/Epoxy composites (Carbon Nanotechnologies, Inc., batch 79) are found to have average length $L = 167 \pm 90$ nm and average diameter $d = 1.1 \pm 0.3$ nm)

2.2.4 Chemical vapor deposition (CVD)

Chemical Vapor Deposition (CVD) has been successfully used for more than 20 years to make carbon fibers and filaments [10, 146], and more recently carbon nanotubes. In this method, catalyst particles are placed into a furnace, heated to a high temperature, and a hydrocarbon gas is flowed in to serve as the carbon feedstock (see Fig 2.5(d)). Nanotube growth occurs from the catalyst particles, and the product is extracted after the furnace is cooled. The quality of nanotubes and whether MWNTs or SWNTs are grown with this method depends strongly on the growth conditions. For MWNT growth, ethylene or acetylene are frequently used as the feedstock gas, with iron, nickel, or cobalt catalyst particles, at furnace temperatures of 550-700°C [38], For SWNT growth, higher energies are required to attain the smaller nanotube diameters, and thus higher furnace temperatures (800-1000°C) are needed. Methane is the most frequently used hydrocarbon for growing SWNTs [87, 88], as it is the most stable hydrocarbon at the elevated temperatures, but carbon monoxide and ethylene [53] have also been successfully used.

CVD growth is often seen as the most promising method for large scale production of SWNTs

at the kg or ton level required for applications such as composites, and several approaches are being pursued to create highly efficient catalyst particles [143] and to optimize processing conditions [33, 46].

Chemical vapor deposition (CVD) manufactured SWNTs were used in our experiments to create SWNT aerogels. The SWNTs were obtained from Thomas Swan, Inc. (Elicarb SW, batch K1713), and they were used as received. According to manufacturer characterization, the material contains 70-90% SWNTs, with $< 3\%$ metallic impurities. The mean SWNT diameter is <2 nm and the mean length is >1 μm. Although the process is optimized for SWNT production, and the material is sold as SWNTs, our analysis of the material by TEM and Raman spectroscopy revealed the presence of many double- and few-walled nanoutubes (DWNTs and FWNTs) along with SWNTs. The presence of DWNTs was confirmed by the company, and is a limitation of their current CVD method.

2.2.5 CoMoCat

This scheme was developed recently at the University of Oklahoma [123]. The CoMoCat method derives its name from the Cobalt-molybdenum catalyst particles used in the synthesis. This scalable approach produces higher quality SWNTs than CVD with a narrow diameter distribution. 80% of the raw product is claimed to be SWNTs.

The key to this method is the Cobalt-Molybdenum catalyst. The Cobalt catalyst, by itself, produces MWNTs. Molybdenum does not catalyze carbon nanotube growth. Instead, Mo stabilizes the cobalt at high temperature, keeping it from sintering and forming large particles. Small (i.e., few atom) Co particles lead to SWNT growth, whereas larger Co particles produce MWNTs and graphite. The process requires modest CO pressures of 1-10 atm, and high gas velocity which

keeps the particles suspended in the gas to prevent inhibition of the reaction by CO_2 buildup, to enhance mixing, and to reduce diffusion within the catalyst particles. As-produced CoMoCat SWNTs contain Co and Mo impurities, as well as SiO_2 from the supporting disk (see Fig. 2.5e) and carbonaceous impurities. Purification of this material requires different techniques from those used with iron-catalyst SWNTs such as HiPco or CVD SWNTs.

2.3 Some properties of single wall carbon nanotubes

2.3.1 Electrical properties

The electrical properties of individual SWNTs derive from the electronic structure of graphene. Graphene is an electrical conductor. The constant-energy contours of the valence (π) and conduction (π^*) bands of graphene in the first Brillouin zone are shown in Fig. 2.6(a). Note that the valence and conduction bands touch (are degenerate) at six "K" points in the first Brillouin zone. The energy at which the two bands touch corresponds to the Fermi level of graphene. Unlike a metal, where the Fermi level is usually well within the conduction band and the Fermi Surface is continuous, the Fermi Surface of graphene consists of only these six "K" points. For this reason, graphene is sometimes called a zero-gap semimetal.

When the graphene sheet is rolled to form a nanotube, a periodic boundary condition is imposed along the direction of the chiral vector, i.e., around the circumference of the nanotube, and the allowed wave vectors in this direction, $\mathbf{k}_\perp$, become quantized such that $\mathbf{k}_\perp = l(2/d_t)$ where d_t is the nanotube diameter, and l is an integer [38, 80]. In the direction along the nanotube length, the wave vectors remain unconstrained and continuous. These allowed wave vectors can be represented as lines superimposed on the first Brillouin zone of graphene, as shown by the thick black

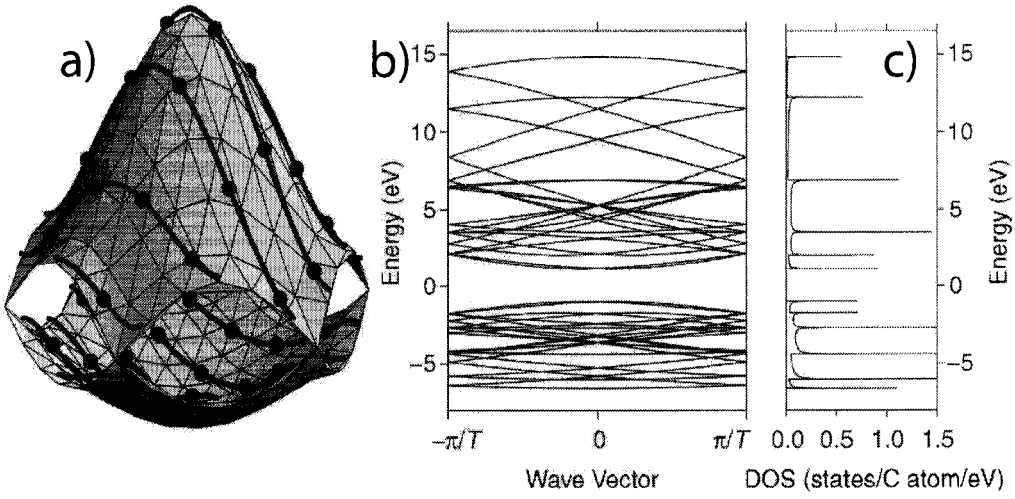

Figure 2.6: Electronic properties of a $(4, 2)$ nanotube from reference [80] a) Constant-energy contours of the valence and conduction bands of graphene in the hexagonal first Brillouin zone. The bands are degenerate at six K points. Dark black lines represent the cutting lines of allowed wave vectors in the $(4, 2)$ nanotube. b) Band structure of the (4,2) nanotube obtained from zone-folding of the cutting lines in (a). $\mathbf{T}$ is the translation vector of the nanotube that defines the unit cell. c) The electronic density of states of the $(4, 2)$ nanotube determined from the band structure shown in (b). Note the discrete spikes known as van Hove singularities.

lines in Fig. 2.6(a). The direction of these cutting lines in the Brillouin zone depends on the chirality of the nanotube - they are continuous in the direction corresponding to the long axis of the nanotube. The electronic band structure of the nanotube along its length is obtained by projecting the constant energy cutting lines from Fig. 2.6(a) onto a plane and zone-folding the projection onto the first Brillouin zone of the nanotube, defined by the translation vector, $\mathbf{T}$, as in Fig. 2.6(b). Note that the $(4, 2)$ nanotube represented in the figure has a bandgap around the Fermi Energy, i.e., it is semiconducting. If, on the other hand, the cutting lines passed through one of the degenerate K points, the valence and conduction bands of the nanotube would also be degenerate, no bandgap would be present, and the nanoube would be metallic. Although this model is correct to first order, the curvature of the nanotube introduces a small angle between adjacent p_z orbitals. This deviation from ideal sp^2 bonding results in a shifting of the K points from the graphene positions, opening a small ($\sim$10 meV) bandgap in some nominally metallic nanotubes.

These electronic properties have been calculated using tight-binding models [55,101,128]. For a given (n, m) nanotube, if $n = m$, (armchair), the SWNT is metallic. If $n - m = 3j$, where j is a non-zero integer, the SWNT has a very small bandgap due to nanotube curvature, and all other SWNTs have large bandgaps. The size of the bandgap decreases with increasing SWNT radius as $1/r$ for the large-bandgap SWNTs and as $1/r^2$ for the small-bandgap SWNTs. This strong radius dependence in the small-gap SWNTs means that the bandgaps of most such nanotubes are exceedingly small, and these SWNTs are frequently said to be metallic. A consequence of these models is that one-third of all possible nanotubes are (nominally) metallic, while two-thirds are semiconducting. A metallic nanotube should ideally have a conductance of $4e^2/h$, where e is the electron charge and h is Planck's constant, which is independent of the nanotube length (i.e., ballistic conduction) [29]. Thus, an individual metallic nanotube has a conductance $\sim 1.5 \times 10^{-4}$ S. The electronic density of states (DoS) of nanotubes can be determined from the band structure. The DoS of a $(4, 2)$ nanotube is shown Fig. 2.6(c). Since this type of nanotube is semiconducting, no electronic states are present around the Fermi energy. In a metallic nanotube, the density of states is nearly constant near the Fermi energy. The sharp spikes in the DoS, known as van Hove singularities, are unique to each type of nanotube and dominate many of the optical properties of carbon nanotubes such as absorption and fluorescence [80].

These models describe the electrical conductivity of individual, isolated SWNTs in a vacuum. In this thesis, we are more concerned with the electrical properties of nanotube networks, usually in the presence of a solid background matrix. Although it is difficult to account theoretically for the essentially infinite possible nanotube/nanotube and nanotube/environment interactions, some theoretical progress has been made for model systems, and experiments have studied a wide range of possibilities. In general, the conductivity of nanotube networks is much lower than would be

Material	Electrical Conductivity (S/cm)	Reference
Individual metallic SWNT	ballistic; $4e^2/h \approx 1.5 \times 10^{-4}$ S	[29]
SWNT ropes	10^4	[145]
Copper	5.8×10^5	[97]
Gold	4.5×10^5	[97]
Purified water	5.5×10^{-8}	[97]

Table 2.1: A comparison of room-temperature electrical conductivities for carbon nanotubes and other materials. It is difficult to directly compare individual SWNT conductivity to the conductivity of bulk materials. In SWNTs, the conductance is independent of length and the cross-section of a nanotube is $\sim 10^{-7}$ cm. If no interactions or contact resistances existed between nanotubes, a bundle of nanotubes with a cross section of 1 cm would, by the same token, have a conductance 10^{14} times higher, or 10^{10} S, and be independent of length. In reality, nanotube ropes do not conduct ballistically, and their conductivity is $\sim 10^4$ S/cm, an order of magnitude lower than copper.

expected from the predictions based on individual nanotubes.

The results of two *ab initio* simulation studies are presented here to elucidate some of the reasons behind the different conductivities in isolated nanotubes and nanotube networks. The first study models the density of states (DOS) of a (10,10) nanotube rope [35]. The second study considers the conductance of two crossed (5,5) nanotubes at a junction [158].

In the first study [35], a rope of (10,10) SWNTs is considered. Such ropes are composed of tightly packed SWNTs in a hexagonal pattern, as seen in Fig. 2.7(a). These structures arise spontaneously due to van der Waals interactions between SWNTs. The distance between nanotubes in a rope is small enough so that each SWNT feels the potential due to every other SWNT in the rope. This interaction results in the formation a "pseudogap" along the rope axis at the Fermi level, where the density of states decreases to about 1/3 of the average value, as seen in Fig. 2.7(b). The pseudogap is present both in the case of axially "misaligned" SWNTs, i.e., the hexagons of adjacent SWNTs are out of register with each other so no symmetries exist in the rope cross-section, and in the case of "aligned" SWNTs, where the hexagons of adjacent SWNTs line up exactly with the hexagons of neighboring nanotubes. The presence of the pseudogap predicts that the conductivity of SWNT ropes is very different from that of isolated SWNTs. In particular, a

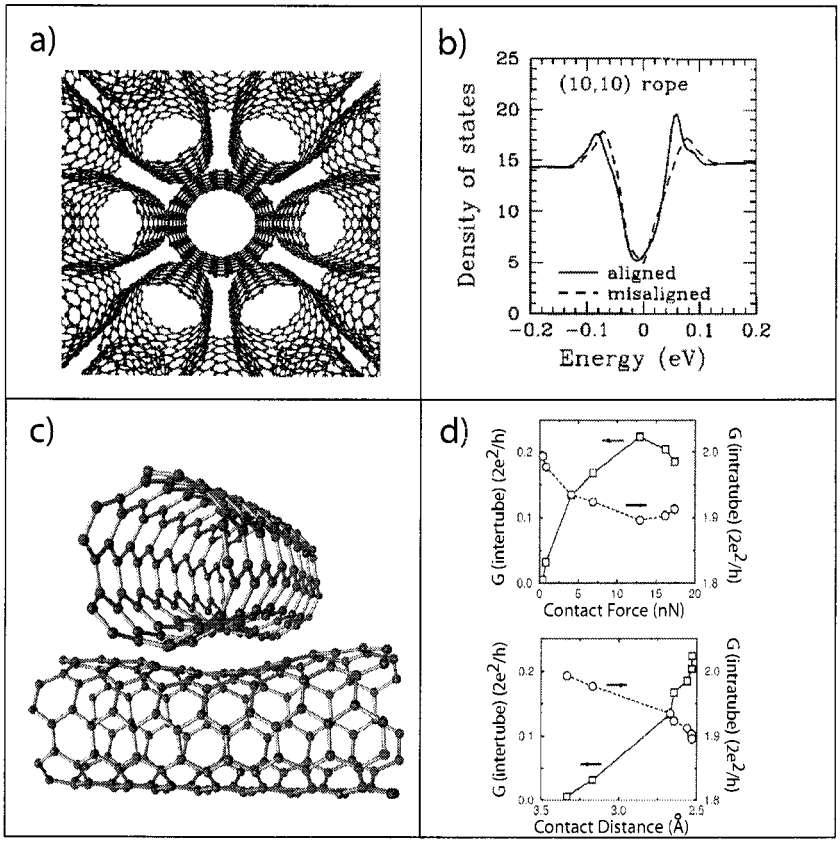

Figure 2.7: a) and b) are from ref. [35], while c) and d) are from ref. [158]. a) Simulated (10,10) SWNT rope. b)Interactions between adjacent SWNTs in the rope from (a) result in a pseudogap near the Fermi energy (0 eV). In contrast, the density of states for an isolated (10,10) SWNT is nearly constant close to the Fermi energy. c) Simulated T-junction of (5,5) SWNTs. A 15 nN contact force force between the SWNTs causes distortion at the junction. d) Plots of the inter-tube and intra-tube conductances as a function of contact force and the corresponding intertube distances. Solid (dashed) lines and left (right) y-axis indicate intertube (intratube) conductances. Note that the intertube conductance increases under greater contact force, but the greater distortion of the SWNTs reduces the intratube conductance.

temperature dependence and high sensitivity to doping is predicted for the conductivity of SWNT ropes.

In the second study [158], a junction of two crossed (5,5) SWNTs is considered, with the SWNTs placed at a 90° angle to each other. The the inter-tube and intra-tube conductivites are derived for this geometry as function of the pressure between the nanotubes at the junction. With no external pressure acting on the SWNTs, the mean distance at the junction predicted from van

der Waals interactions is 3.34Å, and a repulsive force between the nanotubes exists when this separation is reduced. The SWNTs can be brought closer together by an applied force, but are distorted in the process, as in Fig. 2.7(c). Since electrons must tunnel from one SWNT to the other, the smaller separation greatly enhances the inter-tube conductance, which reaches a peak of $0.4e^2/h$ under a 15nN applied force. Note that this maximum value is still an order of magnitude smaller than the intratube conductivity of an isolated (5,5) nanotube. The distortion of the SWNTs, however, lowers the intra-tube conductance by a factor of two.

These models suggest that the electrical conductivity of nanotube networks is sensitive to the interactions of the SWNTs with their environment and to the junctions between them, wherein electrons must tunnel from one SWNT to the next.

Experimental measurements of the room-temperature electrical conductivity of laser-oven SWNT ropes [145] consisting of tens to hundreds of nanotubes in cross-section, have found electrical conductivities of $\sim 10^4$ S/cm (resistivities of 0.34-1.00$\times 10^{-4}$ Ω-cm). These conductivites are significantly lower than might be expected from the conductivities of isolated SWNTs, as predicted by the above simulations.

2.3.2 Thermal transport

Conductive thermal transport through materials is due to phonons (quantized lattice vibrations) and electrons. The high thermal conductivity of metals, for example, can be attributed almost entirely to the motion of electrons. Although a phonon contribution is also present in metals, it is negligible by comparison. For metals, the thermal conductivity is directly proportional to the electrical conductivity, as described by the Wiedemann-Franz Law, $\frac{\kappa}{\sigma} = LT$, where κ is the thermal conductivity, σ is the electrical conductivity, T is the absolute temperature, and L is the

Lorenz number. For an idealized electron gas, $L = \pi^2 k^2/3e^2 = 2.45 \times 10^{-8}$ WΩ/K^2, where k is the Boltzmann constant and e is the electron charge, but this value will differ somewhat for different metals and also at low temperatures [86].

Although $1/3$ of carbon nanotubes are metallic, the thermal conductivity of all nanotubes is dominated by phonons. This is due in part to the fact that the conduction electron density is lower in metallic carbon nanotubes than in most metals. More significantly, the large thermal conductivity is due to strong phonon contributions in carbon nanotubes, diamond, and in-plane graphite that are effectively a result of the high stiffness of carbon-carbon bonds. As a class, these carbon materials have the highest measured thermal conductivities among known substances at moderate temperatures. Table 2.2 summarizes the room-temperature thermal conductivities of nanotubes and some other materials.

In materials where the phonon contribution dominates, the thermal conductivity $\kappa \propto Cvl$, where C is the heat capacity per unit volume, v is the speed of sound, and l is the phonon mean-free-path. At moderate temperatures, the specific heat of SWNTs is similar to that of graphene, and was measured to be ~600 mJ/gK at 300K [60]. In comparison, the heat capacity of water is ~4200 mJ/gK. Four acoustic modes are present in nanotubes: an LA (longitudinal acoustic) mode

Material	Thermal Conductivity (W/m-K)	Reference
Individual SWNT	1,000-6,600	[17,38]
Mats of disordered SWNT	35	[61]
Mats of aligned SWNT	200	[61]
Diamond	895-2300	[97]
Graphite $\parallel$	1950	[97]
Graphite $\perp$	5.7	[97]
Copper	401	[97]
Steel	14-65	[97]

Table 2.2: A comparison of room-temperature thermal conductivities for carbon nanotubes and other materials. For mats of aligned SWNTs, the thermal conductivity is given for the direction of SWNT alignment. Graphite thermal conductivity is anisotropic, and given here for the directions parallel and perpendicular to the graphitic plane. Ranges given for diamond and steel correspond to the thermal conductivities of different types of the material.

Material	Heat capacity at 300K (mJ/gK)	speed of sound (km/s)
(10,10) SWNT	600	24
Air	1000	0.344
Water	4200	1.5
Steel	400-500	5.1

Table 2.3: A comparison of room-temperature heat capacity [60] and speed of sound for SWNTs [40, 127] to some common materials [97]. These properties determine the phonon contribution to thermal conductivity.

corresponding to the motion of atoms along the nanotube axis, two degenerate TA (transverse acoustic) modes, corresponding to atomic displacements perpendicular to the nanotube axis, and a "twist" mode corresponding to torsional distortion of the nanotube around its axis [38]. For a (10,10) SWNT, the phonon velocites are 24 km/s for the LA mode, 9 km/s for the TA modes, and 15 km/s for the twist mode [40, 127]. For comparison, the speed of sound is 0.344 km/s in air, 1.5 km/s in water, and 5.1 km/s in steel. The mean-free path of phonons is thought to exceed the micron lengths of the nanotubes [40]. Thus, very high phonon velocities and long mean-free-paths are responsible for the exceptionally high thermal conductivity of carbon nanotubes. See Table 2.3 for a summarized comparison of these properties.

Molecular simulations have placed the axial thermal conductivity of individual SWNTs as high as 6,600 W/m-K [17], well above that of diamond ($\sim$2000 W/m-K), the current record-holder for the highest known thermal conductivity. Experimental measurements of macroscopic SWNT mats (i.e., paper-like sheets of SWNTs made by drying a SWNT suspension) at room temperature have found more modest thermal conductivities of 35 W/m-K in disordered SWNT mats and $\sim$200 W/m-K in mats where the SWNTs were aligned [61]. As with electrical conductivity, the lower values of thermal conductivity obtained for bulk samples are not surprising and are a result of the significantly weaker thermal conduction between nanotubes than inside an individual SWNT, and they also depend on interactions of the nanotubes with the environment.

2.3.3 Mechanical properties

SWNTs can be viewed as very stiff polymers. The persistence length of SWNTs in water has been measured to be between 32-174 μm [43], which is much greater than a typical length of an individual SWNT. This measurement was performed by direct visualization of the thermal fluctuations of individual, surfactant stabilized SWNTs in aqueous solution using fluorescence microscopy. To enable visualization, a hydrophobic fluorescent dye was present within the hydrocarbon chains of the surfactant near the nanotubes, but the SWNTs themselves were not modified. Table 2.4 compares the persistence length of SWNTs to other polymers. Because of the high persistence length, individual SWNTs behave much like rigid rods in solution [163], and it is reasonable to model SWNT dispersions as hard-rod systems. In our work, we will describe SWNT dispersions as suspensions of hard rods. This approach enables us to draw meaningful conclusions about the network formation in these systems by analogy with other work on hard rods.

Description of the material properties of individual SWNTs usually contain ambiguities. For example, the cross-sectional area of a SWNT can be chosen in several relatively arbitrary ways, and a strain applied to the nanotube is not uniform over any SWNT length due to its atomic sctructure [38]. Nevertheless, experimental measurements of SWNT Young's modulus have been reported. For example, TEM observations of the thermal fluctuations of suspended SWNTs have yielded values for Young's (elastic) modulus of 1.3$\pm$0.2 TPa [90]. Other theoretical and experimental studies have cited similar values of $\sim$1 TPa, with some ranging as high as 5 TPa [119]. Table 2.5

Material	Persistence length (μm)	Reference
SWNT	32-174	[43, 90, 119]
F-actin	16	[36]
fd virus	2.2	[36]
λ-DNA (double-stranded)	.05	[36]

Table 2.4: A comparison of the persistence length of SWNT to other polymers.

Material	Elastic Modulus (GPa)	Reference
Individual SWNT	1000-5000	[90, 119]
Diamond	1035	[25]
Steel	207	[25]
Epon 828 epoxy	2.75	[58]
Carbon fiber reinforced epoxy	145	[25]

Table 2.5: A comparison of the elastic modulus of SWNTs to other materials.

compares the elastic modulus of SWNTs to other common materials.

Because of the large stiffness of SWNTs, significant effort has been made to use them as a reinforcing agent in composites. These efforts have met with limited success. The molecular "perfection" of SWNTs means that they do not bind strongly to most matrix materials and are therefore inefficient reinforcing agents [38]. The Young's modulus of SWNT ropes is also sharply lower than that of isolated SWNTs, due in part to sliding of SWNTs within the rope. Some successful reinforcement approaches have included spinning (weaving) MWNTs into strong yarns [159] and using polyvinyl alcohol (PVA) as a binding agent. PVA seems to have an unusually strong affinity to SWNTs, and this has been used to create very strong SWNT/PVA fibers [149]. In our work, we successfully use PVA to reinforce carbon nanotube aerogels [22].

Chapter 3

Working with carbon nanotubes

3.1 Dispersing carbon nanotubes

3.1.1 Sonication

Sonication is a key tool used for dispersing carbon nanotubes. Sonicators use a transducer to generate ultrasonic (high-frequency acoustic) waves that are conducted into the sample. Among other uses, the sound waves can be employed to break apart aggregates of microscopic particles. Various types of sonicators exist with different primary applications. These include bath sonicators, tip sonicators, probe (diagnostic) sonicators, and horn sonicators [1]. See Table 3.1 for more details.

Although the wavelength of the sound waves may be quite large in solution (e.g., several cm for a 20KHz bath sonicator in water), sonication is highly effective for dispersing carbon nanotubes and other nano- and micro-scale particles because of microcavitation [34]. Expansion and compression of a liquid under sonication causes regions of low and high pressure. If enough energy exists during the expansion cycle to overcome the binding forces that hold the solvent molecules

together, the molecules are torn apart, creating a gas-filled gap, or a microcavity. At the onset of the compression cycle, the microcavity violently collapses, creating a microscopic jet of fluid that travels at more than 100 m/s. The rapid compression of the gases within the microcavity causes the immediate area to briefly superheat to temperatures $> 5000°C$. It is this short-range, high-intensity microcavitation that makes sonication effective in dispersing nano-scale particles.

For nanotube dispersions, certain types of bath- and tip-type sonicators have been found to be useful. In particular, bath sonication at 55kHz (Cole Parmer sonicator model 08849-00, 1 pint, 17W) is highly effective at dispersing SWNTs without damaging them [75], and this dispersion method was used in all of the experiments described herein. Bath sonication at significantly higher or lower frequencies (e.g. 20 kHz that is standard for many bath sonicators) is usually much less effective. A stronger, 22.5KHz tip sonicator (Fisher Scientific sonic dismembrator, model F60, 100W) was also used to aid in the dispersion. In-house studies, done by Jian Zhang and Mohammad Islam, have shown that SWNTs are not substantially damaged when the tip sonicator output power is kept at or below 6W for less than 10 minutes. However, tip sonication does weaken the glass vials containing the nanotube samples. The glass vials can easily shatter when subsequently returned to the bath sonicator. Because of this effect, *the sample should be transferred to a new glass vial after each tip-sonication and before being placed into a bath sonicator.*

A typical sonication procedure is as follows. Dry nanotube powder is ground in an agate stone mortar with a small amount of solvent (and surfactant, if applicable) until no large particles remain. The slurry is combined with the desired amount of solvent and transferred to Wheaton 20 mL glass disposable scintillation vials. These vials were found to be optimal for the application. Their thin glass walls minimize SWNT sticking and are more effective at conducting ultrasound than plastics or thicker glass. These particular vials were also found to be sufficiently strong to

withstand extended bath sonication, whereas most other glass vials would invariably crack. The cap is secured to the vial with Parafilm to prevent it from being unscrewed in the sonicator. The sonicator reservoir is filled with tap water, and turned on for at least one hour prior to placing the SWNT sample inside. This step degasses the water bath, resulting in more effective sonication. Degassing the water appears to be most important at elevated sonication temperatures such as those used in the epoxy composites experiments. Samples are usually sonicated for several hours. Unless higher temperatures are required, sonication is most effective at room temperature. Under extended sonication, the water bath can heat up considerably, and it is useful at this point to change the water or move to a second sonicator. The dispersion may be monitored by periodically examining small samples of the nanotube suspension for aggregates under an optical microscope. If necessary, tip sonication is used to disperse persistent aggregates. The initial dispersion process may take 24 hours or more. Over-sonication appears to be possible when surfactant is sonicated at elevated temperatures for extended periods of time. In this case, the dispersion gradually becomes worse as the sonication progresses. As a rule, extended sonication (more than an hour) of surfactant-stabilized nanotubes should be done near room temperature, and stopped when no aggregates are observed.

The final quality of the dispersion can be verified by atomic force microscopy as described later in this chapter.

Sonicator type	Typical frequency (KHz)	Typical power density (W/cm^2)	primary applications
Bath	20 - 100	0.01 - 1	ultrasonic cleaning
Tip	20 - 40	1 - 50	tissue pulverization
Cup-Horn	20 - 40	100 - 1000	pulverization
Probe (diagnostic)	500 - 3000	1 - 1000	imaging (medical, etc.)

Table 3.1: Types of sonicators, their typical operating parameters, and primary applications [1].

3.1.2 Ultracentrifugation

Centrifugation is used to separate or concentrate dispersed materials in a liquid medium by rapidly spinning the sample. The force acting on a unit of a spinning sample is $m\omega^2 R$, where m is the mass of the individual dispersant, ω is the angular velocity, and R is the distance of the sample from the center of the rotor. Since centrifuges have various angular velocities and sizes, the universal unit for centrifugation is g, equal to the earth's gravitational acceleration, $g \approx 9.8$ m/s^2. Typical centrifuges produce thousands to tens of thousands of g's. Ultracentrifuges, on the other hand, can produce up to 1,000,000g or more. Particles sediment under this acceleration. In the dilute, large particle limit, the particle settling velocites follow Stokes' Law, i.e., $V_s = \frac{2}{9}\frac{r^2 x g(\rho_p - \rho_f)}{\eta}$, where V_s is the settling velocity of a particle, r is the Stokes radius of the particle, x is the number of g's, ρ_p is the particle density, ρ_f is the density of the fluid, and η is the viscosity of the fluid. To achieve the large g values, ultracentrifuge rotors spin at up to 70,000 - 90,000 rpm in vacuum on highly efficient air bearings. Rotors are frequently machined from solid titanium for its high strength and light weight. Because of the large forces involved, care must be taken to use undamaged centrifuge tubes, to fill the centrifuge tubes to the recommended capacity to avoid collapse, to carefully balance the rotor by placing samples of equal weight at opposing sides of the rotor, and to ensure that all seals and pieces are undamaged and in place.

Among other applications, ultracentrifugation is useful for concentrating dilute SWNT dispersions and for eliminating heavier impurities or undispersed nanotube bundles from solution. It is generally easier and quicker to disperse SWNTs in dilute suspensions than in concentrated ones, especially when starting from dense, dry SWNT material. The dilute dispersions may then be concentrated as desired. For example, for NaDDBS surfactant-stabilized nanotubes (see below), it is sometimes beneficial to disperse the nanotubes by sonication at relatively low concentrations (e.g.

0.05-0.1 wt%). After sonication, the dispersion is centrifuged at 1000 - 10,000 g (5,000-15,000 RPM) for 1-2 h to sediment any undispersed nanotubes and heavier particles. The supernatant, containing mostly isolated, dispersed SWNTs, is then transferred to a second ultracentrifuge tube and centrifuged at >500,000g, or ~70,000RPM for another 4-6 h. The pellet that collects at the bottom of the centrifuge tube contains individual SWNTs surrounded by surfactant. For HiPco SWNTs, the pellets were found to contain ~1.8 wt% SWNT; this should be verified for other types of SWNTs. The clear supernatant is decanted, and the pellet can then be diluted to the desired concentration. Since dense SWNT aggregates are not present, and the SWNTs in the pellet are covered with surfactant, a brief (~30 min) sonication is usually sufficient to create a homogeneous dispersion at the new concentration. Although most of the surfactant is believed to be physiosorbed to the SWNTs [75], some unbound surfactant remains in the supernatant and should be replaced as needed.

Another interesting ultracentrifuge application for SWNTs is the ability to separate SWNTs by diameter (and therefore by the SWNT electronic structure). Strong diameter selectivity was reported recently [7] when SWNTS were ultracentrifuged in a pre-established density gradient, a common method used in biology for protein separations, and this may open the way to a broad range of specialized applications using single nanotube species. However, only very small amounts of fractionated SWNTs can be separated and retrieved, so this method has limited utility for applications such as composites, where large SWNT quantities are needed.

3.1.3 Solvents, surfactants, and other solubilization methods

SWNTs and other small-diameter nanotubes are usually very difficult to disperse in solution due to their strong van der Waals interactions. Approaches for dispersion include finding an appropriate

solvent, steric stabilization with surfactants or other agents such as DNA [161], and functionalization of the nanotubes to increase solubility.

Among the most effective solvents found for directly dispersing SWNTs are organic amides [94]. These solvents include N,N-dimethylformamide (DMF), N,N-dimethylacetamide (DMA), N,N-diethylacetamide (DEA), N,N-dimethylpropanamide (DMP),N-methylpyrrolidone (NMP). Another organic solvent that has been effective is 1,2-dichlorobenzene. There remains some uncertainty as to why these particular solvents are more effective than others, but it is believed that it is due to a combination of dipole-dipole interactions between the polar solvent and the polarizable (through π electrons) nanotubes, and a commensurate geometry of the solvent molecules to the nanotube structure. The solvent molecules have the right shape and charge distribution to interact strongly with the nanotube surface, leading to steric stabilization by the solvent molecules [94]. The main advantage of dispersing nanotubes directly in a solvent is that the solvent can be easily removed by evaporation. However, the nanotube solubility limit is typically low, and in general only dilute nanotube dispersions can be created. Significantly higher SWNT concentrations can be obtained by using surfactants, as described below. Table 3.2 summarizes approximate SWNT solubility limits for some effective dispersion strategies. It should be noted that most solvents are extremely poor at dispersing nanotubes, including some that may seem promising, such as aromatic solvents (e.g. benzene, xylene, toluene), water, alcohols, etc.

Surfactants are an effective means for suspending SWNTs in water at high concentrations. Of the many surfactants used, Sodium Dodecylbenzene sulfonate (NaDDBs) (see Fig. 3.1) appears to be one of the most effective at creating stable SWNT suspensions. Sonicated suspensions containing 20mg/mL SWNT and a 10:1 surfactant to SWNT ratio were found to contain $63 \pm 5\%$ isolated SWNTs (as opposed to SWNT bundles), while 0.1 mg/mL suspensions contained $74 \pm 4\%$

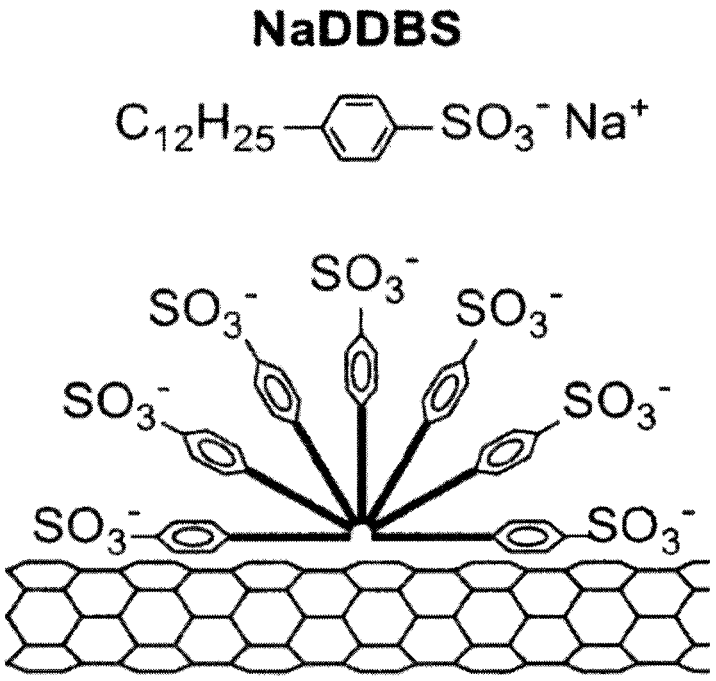

Figure 3.1: Chemical formula of NaDDBs surfactant and a schematic of its interaction with a SWNT from Ref. [75]. It is believed that the surfactant forms hemi-micelles on the SWNT surface.

isolated SWNTs. It is difficult to disperse SWNTs above about 20 mg/mL, because the suspension rapidly turns into a gel. Other surfactants, such as sodium dodecyl sulfate (SDS) are also commonly used by some research groups, but stable SWNT suspensions can only be created at or below ~0.1 mg/mL in SDS. One possible advantage to using SDS, a very common surfactant, is that it is available at high purity. Typical purities available for the specialized NaDDBs surfactant are usually much lower, of order 80%. The remaining 20% consists mostly of byproducts from the synthesis. A flowchart showing the procedure for dispersing SWNTs in NaDDBs surfactant is shown in Fig. 3.2.

Another promising method for dispersing SWNTs in water is with the use of DNA. Single-stranded DNA has been shown to wrap around carbon nanotubes in a regular, helical structure. Solutions with a SWNT content of up to 4 mg/mL were achieved with this method [161]. It was

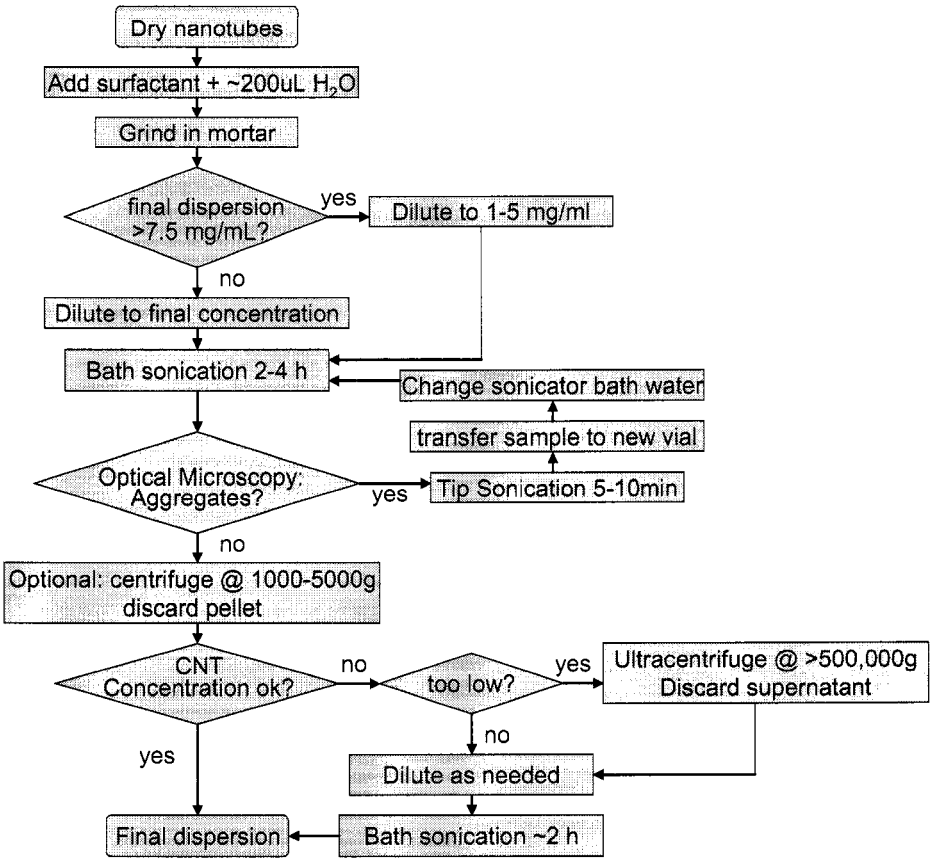

Figure 3.2: Flowchart of process for dispersing SWNTs in NaDDBs surfactant.

also found that the wrapping is selective; different DNA sequences wrap preferentially around different SWNT diameters [162]. This result can potentially lead to the development of methods for separating SWNTs by diameter in large quantities.

Another method for solubilizing SWNTs is by functionalization. Although this method is not used in our experiments, it is included here for completeness. Functionalization of carbon nanotubes refers to covalently bonded functional groups on the surface of the nanotube. Since ideal carbon nanotubes do not possess any free bonds, functionalization requires breaking some sp^2 carbon bonds to accommodate the new functional groups, altering the nanotube structure and properties. The process typically involves acid treatment to break some of the carbon bonds on

the nanotube surface. Various types of acids can be used, including sulfuric and nitric acids, and functionalization also occurs as a side-effect of acid treatment in nanotube purification procedures described later in this chapter. Typically, the acid treatment oxidizes the nanotubes, creating carboxyl (COO^-) groups on the nanotube surface. Other groups, such as sulfonic groups (SO_2 or SO_3^-) may also form depending on the acids used. These reactive groups can be subsequently covalently joined with a variety of molecules including amines, polymers, etc, to obtain desired surface properties [144]. Functionalized SWNTs have been shown to be soluble in water, up to about 10 mg/mL, comparable to the values achieved with NaDDBs surfactant [155]. Although functional groups can form anywhere on the nanotube surface, SWNTs are only a few to tens of carbon atoms in circumference, and removing even a single bond can weaken them significantly, resulting in breakage. For all practical purposes, functionalization cleaves SWNTs, leaving the functional groups on SWNT only at the SWNT ends and not on the sidewalls. In contrast, thick MWNTs can have functional groups along the sidewalls due to their larger diameters and reduced sensitivity to defects.

Solvent	SWNT dispersion limit (weight fraction)	Reference
DMF	10^{-5}	[94]
1,2-dichlorobenzene	10^{-4}	[94]
Water/NaDDBs surfactant	10^{-2}	[75]
Water/SDS surfactant	10^{-4}	[75]
Water/DNA	4×10^{-3}	[161]
Water/Functionalized SWNT	10^{-2}	[155]

Table 3.2: approximate SWNT dispersion limits for some effective solvents and water/surfactant combinations

3.2 Characterization

3.2.1 Raman scattering

Raman spectroscopy is based on the inelastic scattering of light. A photon incident on a sample usually scatters elastically, with no change in energy (Rayleigh scattering). However, one in about 10^7 photons will scatter inelastically by producing or absorbing a phonon in the process.

In Stokes Raman scattering, an electron in the ground vibrational energy state of a molecule in the sample is excited by the incident photon to a virtual vibrational state. The energy of this virtual state depends on the energy of the incident photon. When the photon is 'released,' the electron relaxes back to another vibrational state. In most cases, it returns to the ground state, producing a Rayleigh scattering event. Less often, the electron relaxes to an excited vibrational energy state, typically the first excited vibrational state. A phonon is produced in the nanotube, and the energy of the scattered photon is reduced by the energy difference between the two vibrational states. This change in photon wavelength is the Raman shift typically seen in plots of Raman spectra. To first order, the shift does not depend on the incident wavelength, only the energy difference between the vibrational states.

Anti-Stokes Raman scattering refers to the situation where the electron is already in an excited vibrational state. Upon excitation by a photon to a virtual vibrational state, as before, the electron typically relaxes back to the ground vibrational state. A phonon is absorbed in the process, and the energy of the released photon is higher than that of the incident photon by a vibrational quanta.

The vibrational modes involved in the Raman process are highly specific to the chemical bonds in a compound and can thus be used to identify molecules. Vibrational modes are also probed by Infrared (IR) absorption techniques, such as fourier transform infrared spectroscopy (FTIR),

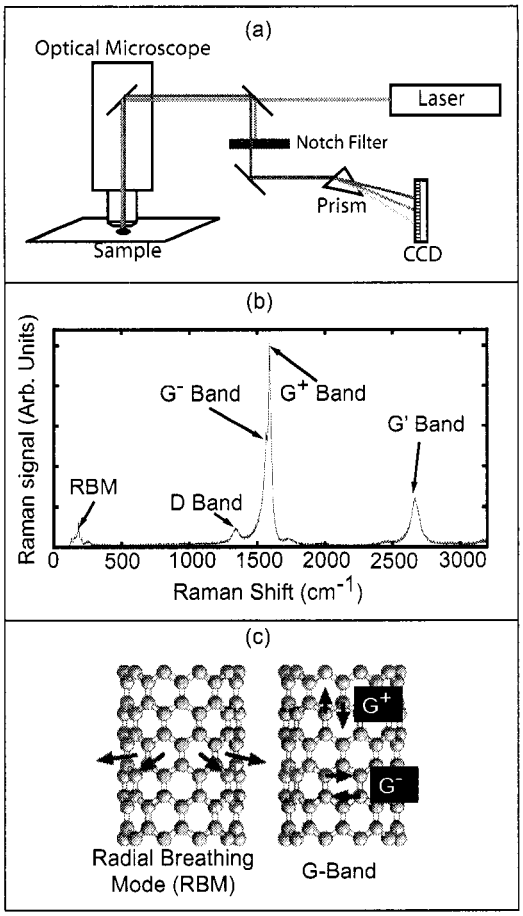

Figure 3.3: a) Simplified schematic of a Raman Spectrometer. b) Raman spectrum of CVD-grown carbon nanotubes from Thomas Swan (Elicarb SW batch 1713). Radial Breathing modes, D, G, and G' bands are depicted c) Schematic representation of the vibrational modes involved in the RBM and G bands of the nanotube Raman spectrum.

but transition selection rules differ between the two methods. As a result, molecules that absorb strongly in the IR may not be strong Raman scatterers, and vice-versa. Generally speaking, chemical groups that are asymmetric in their molecular structure and undergo a large change in electric dipole moment during molecular vibration tend to be strong FTIR absorbers and weak Raman scatterers. Materials that are symmetric in their molecular structure and undergo a large change in electron polarizability during vibration tend to be strong Raman scatterers and weak FTIR absorbers. Carbon nanotubes fall into the second category, and their Raman signal is significantly

stronger than their IR absorption spectrum.

In addition to the strong signal, Raman has several other advantages for nanotube analysis over IR absorption techniques. For one, Raman is a technique frequently performed under a microscope and very small samples can be studied. Spectra can be obtained from individual nanotubes or small aggregates without the need to disperse the nanotubes or mount the sample. Water and water vapor, which strongly absorb IR radiation, do not interfere as strongly in Raman scattering as in IR spectroscopy, resulting in cleaner spectra. Raman spectroscopy has thus become a standard tool in carbon nanotube characterization, and the spectra are well-understood and relatively easily interpreted. We note, however, that IR spectroscopy has been used effectively to study certain features of carbon nanotubes [91, 107, 147].

A schematic diagram of a typical Raman apparatus is shown in figure 3.3(a). On a basic level, Raman spectroscopy can be used to determine the diameters of individual carbon nanotubes or the distribution of diameters in bulk nanotube material. It can also be used to estimate the amount of nanotubes in a sample in relation to other forms of carbon.

The main features of a typical carbon nanotube Raman spectrum are shown in figure 3.3(b). Starting from the left side of the plot (lowest energy shift), the spectrum shows radial breathing modes (RBM) at wavenumbers $\sim$100-300 cm^{-1}, the D-band at $\sim$1350 cm^{-1}, the G-band at $\sim$1590 cm^{-1} and the G'-band at $\sim$2700 cm^{-1} [38–40, 78, 127].

The radial breathing modes (RBM) correspond to the radial vibration of carbon atoms in a nanotube perpendicular to the graphene plane. The resulting expansions and contractions of the nanotube are reminiscent of "breathing", as shown in figure 3.3(c), giving rise to the name. The energy of this mode is highly specific to the nanotube diameter - each type (diameter and chirality) of nanotube has a single, sharp RBM peak. RBM are therefore the best way to characterize

the diameter distribution in a sample. The Raman shift of a radial breathing mode is inversely related to the nanotube diameter by the relation $\omega_{RBM} = 248/d$, where ω_{RBM} is in cm^{-1} and d is in nm [79]. Typically, the notch filter in the spectrometer designed to cut out the excitation laser wavelength (0 cm^{-1}) also strongly attenuates the signal up to about 100 cm^{-1}. In such systems, carbon nanotubes with diameters greater than ~2.5 nm will not resolved. RBM peaks are sometimes seen at ~250-400 cm^{-1}, corresponding to diameters of ~0.6-1 nm. These very small-diameter nanotubes are consistent with the small interior tubes of double- and few-wall carbon nanotubes, and may be an indication of the presence of such nanotubes. This is the case with the CVD sample in figure 3.3(b) [13].

The G-band derives its name from the main feature seen in Raman spectra of graphite [45]. In graphite, the feature is centered at 1582 cm^{-1}, and is the result of in-plane vibrations of carbon atoms within the graphite layers. The curvature of carbon nanotubes causes this peak to split into several features, dependent on nanotube diameter, chirality, and the direction of the vibrations with respect to the nanotube axis. Because of degeneracy, two main peaks are frequently evident, a lower-frequency G^- peak associated with in-plane vibrations perpendicular to the long axis of the nanotube, and a higher-frequency G^+ peak for vibrations along the long axis of the nanotube, as seen in figure 3.3(c). Although the splitting depends on several nanotube properties, degeneracy makes it difficult to distinguish individual nanotube properties in a bulk nanotube sample. RBM, described above, are better suited for such analysis. However, the presence of RBM and a split G-Band is a strong indication of the presence of carbon nanotubes in a sample.

The D-band, or disorder-induced band, is a relatively broad feature in the Raman spectrum at ~1350 cm^{-1} that is an indication of the amount of disordered (non-graphitic) carbon present in the sample. There are no detailed studies thus far that correlate the D-band structure to different

defect types, such as vacancies, dislocations, kinks, or other types of carbon morphologies. In bulk nanotube samples, the height of the D-band peak relative to the G-band is an indication of the purity of the sample. A G-band that is 10 to 100× stronger than the D-band indicates a relatively pure nanotube sample.

The G'-band, at ~2700 cm^{-1}, is a second-order, double-resonance feature in the Raman spectra of graphite and nanotubes and is related to the D-band [127].

3.2.2 Thermogravimetric analysis

Thermogravimetric analysis (TGA) is the study of the weight changes in a sample as a function of temperature [139]. A schematic of a TGA apparatus is shown in figure 3.4(a). The apparatus consists of a temperature-controlled furnace and dual balance beams with sample pans and attached thermocouples. The furnance is usually continuously purged with a gas, such as air, oxygen, nitrogen, or argon. In a typical experiment, a small amount (~3-5 mg) of powdered sample is placed in one of the sample pans, while the other pan serves as a reference. The temperature of the furnace is slowly increased, while the temperature of each pan and the instantaneous sample mass are recorded. Both loss and gain of mass can be observed with increasing temperature. Loss of mass is attributable to vaporization of the material, whereas a mass gain most likely indicates a reaction with the gas, such as oxidation.

Several factors can influence the accuracy of the measurement. The heating rate must be slow enough for temperature gradients within the sample and the furnace to be minimized. Increasingly rapid heating rates will appear to shift the features to higher temperatures and to broaden them. This effect will be more pronounced in larger or denser samples. It is therefore desirable to use powdered samples in very small quantities and to heat them slowly. To facilitate this, balances

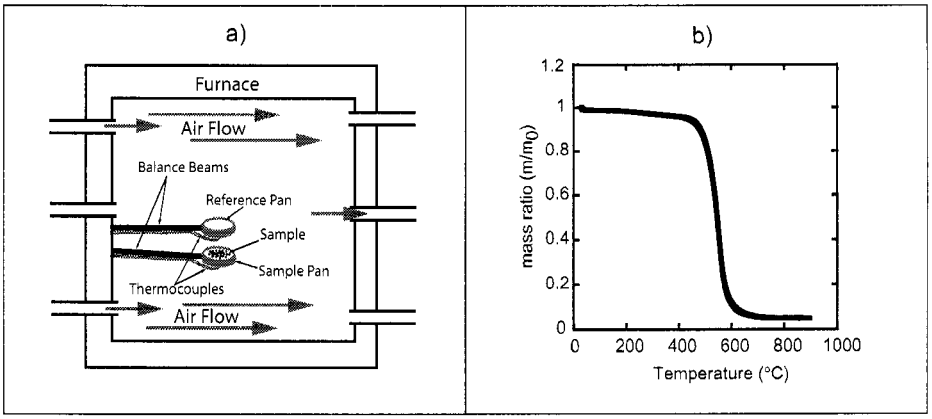

Figure 3.4: a) Schematic of Thermogravimetric Analysis (TGA) apparatus. Two identical balance beams and pans are housed inside a furnace. The temperature of each pan is monitored with a thermocouple. Powdered sample is placed in one pan, while the second pan serves as the reference. Air (or another gas, depending on the application) is flowed through the sample area, while the furnace temperatrure is slowly raised. b) TGA results for a 3 mg sample of CVD-grown nanotubes from Thomas Swan (Elicarb SW batch 1713). The temperature is ramped from room temperature to 900°C at 3°C/min. The ratio of the sample mass to the initial sample mass is plotted vs. temperature. The carbonaceous material vaporizes around 600°C, which is typical of a high-quality nanotube sample. Above 800°C less than 5% of the initial mass remains. This remaining mass is typically attributed to the metal catalyst particles.

used in TGA systems are highly sensitive, with resolutions as fine as 0.1 μg. For SWNTs, samples of 1-3 mg and heating rates of 3-5°C/min are usually adequate.

A second consideration, partly compensated for by system design, involves the change in the density of the gas with temperature and the resultant change in buoyancy of the sample pan and convective currents. For example, the apparent change in mass for a sample and pan with volume 1 cm^3 due solely to buoyancy effects in air between 20°C and 1000°C is 0.5 mg [139]. Since the typical sample mass is of the same order, these buoyancy effects must be considered. In addition, temperature gradients result in convection currents of gas within the sample chamber that can affect accurate measurements. While different TGA systems use different methods to compensate for these effects, the system used for our experiments used an identical reference pan, which is assumed to stay at constant mass, and fluctuations of the reference pan are subtracted off. Gas is flowed through the narrow furnace horizontally to reduce convection. Finally, all TGA systems are

calibrated with known standards to give more accurate readings.

The routine TGA measurement for SWNT samples is the quantification of the metal catalyst particle content. The measurement is typically done in (flowing) air between room temperature and ~900-1000°C. In the process, nanotubes and other carbon oxidize into gas (e.g. CO_2). Gold or platinum TGA pans must be used for the measurements, with gold pans being only marginally sufficient to withstand the high temperatures. Figure 3.4(b) shows a typical TGA plot for a relatively pure carbon nanotube sample. Most of the mass loss occurs in a single, narrow temperature range around 600°C. At high temperature, above ~800°C, less than 5% of the initial mass remains. Typically, this residual mass is due to metallic catalyst particles, and the value can be used to quantify the amount of metallic impurities in the sample. It is important to note that for some catalysts, such as iron, the particles will be partially, or entirely, oxidized. Thus, the residual mass is in the form of iron oxide, Fe_2O_3, (rust), and not metallic iron. The iron content is approximately 70% of the iron oxide content, assuming that the iron is fully oxidized. Unanticipated impurities, such as SiO_2, might also remain in the sample and skew the results.

Interpreting the vaporization temperatures of the carbon material can also yield useful information. However, distinguishing nanotubes from other forms of carbon by vaporization temperatures is difficult or impossible, since the apparent vaporization temperatures are strongly dependent on the metal catalyst content [93]. In particular, metal particles will themselves oxidize under high temperatures in an exothermic reaction. The additional heat shifts the apparent vaporization temperature of the carbon material to lower values, overwhelming any differences between the various forms of carbon. The metallic particles may, in turn, be encapsulated in carbon and may not oxidize until the carbon layer itself vaporizes. For this reason, specific vaporization temperatures cannot be assigned to different carbon species in the sample. Nonetheless, some conclusions may be drawn.

Highly purified SWNTs tend to oxidize at higher temperatures than raw SWNT material (typically 500-600°C vs. 350-500°C), largely because of low metal catalyst content. Lower vaporization temperatures are also observed in acid-treated samples that contain few metallic impurities. In this case, the reduced vaporization temperature is attributed to damaged SWNTs which vaporize more easily. In pure SWNT samples, vaporization occurs in a single step over a narrow (tens of degrees) temperature range, whereas shallower vaporization curves and variable slopes may be observed in samples that contain significant metallic or carbonaceous impurities or damaged SWNTs.

The TGA equipment used in the present measurements (TA Instruments model SDT 2960) also performs differential thermal analysis (DTA) simultaneously with TGA measurements. The DTA data contains information about temperature differences between the sample and reference pans giving insight to exothermic or endothermic reactions that take place. Since SWNT samples are not homogeneous, however, the bulk temperature of the sample is not representative of the local temperature near an oxidized catalyst particle, and does not provide sufficient information about the sample to distinguish between carbon species.

3.2.3 Atomic force microscopy

Atomic force microscopy (AFM) is a type of scanning probe microscopy (SPM) in which the surface topography of a sample is imaged by measuring the force exerted on a cantilever tip scanned across the sample surface [102]. The principle is somewhat analogous to the record player stylus. As the cantilever is moved over a surface, it bends or is deflected when it encounters a surface feature. The deflection is monitored by a laser reflected from the top surface of the cantilever and imaged onto a quadrant photodiode, as seen in figure 3.5(a). A small displacement of the cantilever results in a greatly magnified displacement of the laser spot on the photodiode, and thus

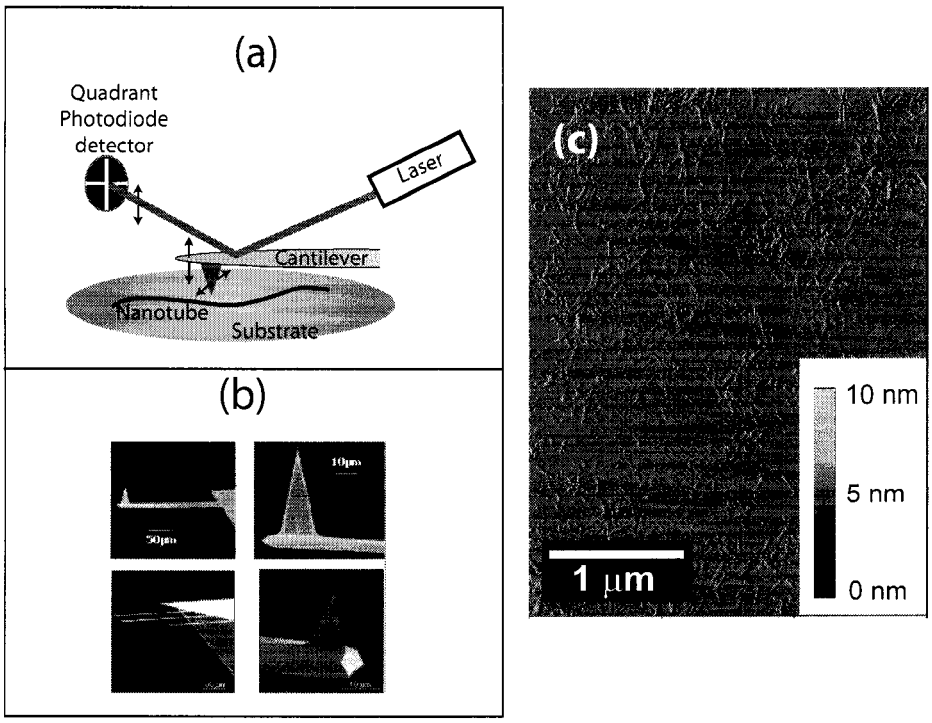

Figure 3.5: a) Schematic of a tapping-mode atomic force microscope. An oscillating (tapping) cantilever is scanned across the substrate, and is deflected up or down as it encounters topological features, such as a nanotube. A laser reflected from the top surface of the cantilever is imaged onto a split diode detector that can sensitively monitor the position of the laser. b) Electron microscope images of AFM tips. c) Tapping-mode AFM image of SWNTs deposited from DMF solution onto an HMDS-treated silicon wafer.

very small cantilever deflections can be observed. The photodiode signal contains information about the normal force, the bending force, and the twisting force on the tip [102].

Figure 3.5(b) shows several AFM tips. AFM tips are made photolithographically from silicon. The flexible cantilevers are derived from thin layers of SiO_2 or Si_3N_4 deposited on the silicon wafer prior to etching. Frequently, the cantilevers are also coated with a reflective metal such as platinum after etching to enhance reflection of the laser. The rounded radii of modern AFM tips have diameters of 1-50 nm, and can therefore be used to probe fine lateral detail. However, even finer detail can be obtained from the height information. Lateral AFM resolution is limited by the tip diameter and the accuracy of the piezoelectric positioners used to move the tip. In contrast,

height information can be obtained to sub-nanometer resolutions because it mainly depends on the displacement of the laser spot on the photodiode.

AFM has two basic modes of operation: contact mode and tapping mode. In contact mode, the cantilever tip is dragged across the surface of the sample with a constant force. In tapping mode, the tip is driven to oscillate at its natural resonant frequency, typically of order 10^4 Hz. The amplitude of the sinusoidal oscillations is kept constant by a feedback mechanism, which keeps the separation between the tip and the surface constant. The feedback signal is a measure of the topography of the surface [32].

AFM imaging of carbon nanotubes usually involves depositing the nanotubes from a dilute suspension in a solvent onto a smooth surface, such as a silicon wafer. Since the thin oxide layer present on all silicon wafers carries a net negative charge and is hydrophilic, it is usually necessary to treat the surface of the wafer to make it compatible with the hydrophobic nanotubes. One method to achieve this is through silanization, or covalent bonding of hydrophobic groups onto the surface of the oxide layer by means of a silane-derived compound. Silane, the silicon analogue of methane, has the chemical formula SiH_4, and reacts readily with the oxide layer. Compounds used for silanization usually replace several of the hydrogens with hydrophobic groups, and may also use higher-order structures based on silane, such as silazane or siloxane. In our work, we used hexamethyldisilazane (HMDS) [137], as seen in figure 3.6.

The silanization procedure aims to obtain a single, uniform monolayer of hydrophobic groups on the wafer surface. In a typical process, the wafer is cleaned (e.g., washed with Alconox detergent and deionized water, followed by a rinse with acetone) and placed in a vacuum jar. A small, open dish or bowl with HMDS ($\sim$1-5 mL) is also placed in the vacuum jar near the wafer, but not in contact with it. The vacuum jar is then pumped out and left for several hours or overnight. The

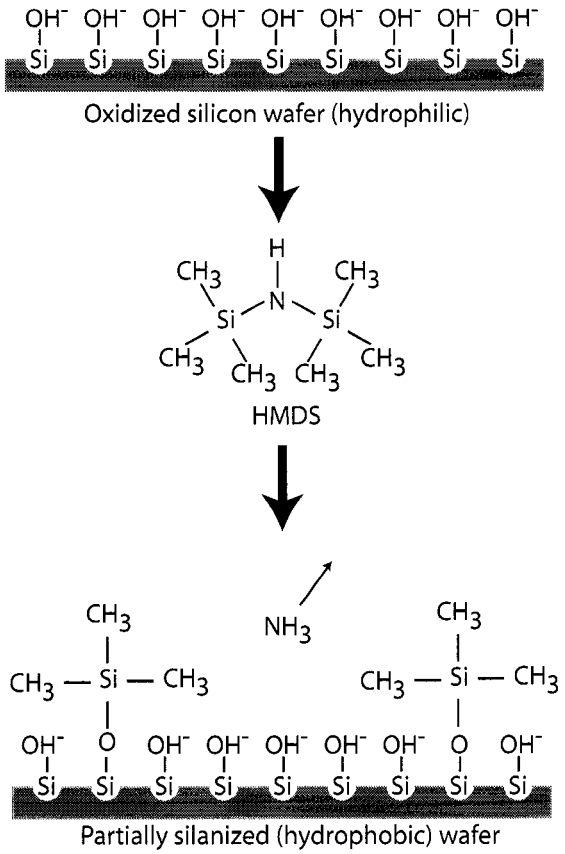

Figure 3.6: A thin hydrophilic oxide layer is typically present on silicon (top). Treatment with Hexamethyldisilazane (HMDS), middle, can render it hydrophobic. Nitrogen in the HMDS molecule reacts with two hydrogens (possibly from the surface layer), splitting the molecule and creating ammonia. Each half of the original molecule bonds to oxygen atoms on the surface with the methyl groups pointing up, rendering the surface hydrophobic.

liquid HMDS evaporates, and coats exposed surfaces. The degree of silanization is time dependent - the longer the wafer is left under vacuum, the more hydrophobic the surface becomes as the available surface groups become filled over a period of hours. This procedure gives better results and more control over the resultant surface properties than simply dipping the wafer into liquid HMDS. For one, any moisture present on the wafer surface upon dipping will inhibit silanization, resulting in patchy coverage. Also, drying the HMDS after dipping results in films forming on the silicon surface that are difficult to wash away.

Once the wafer is silanized, nanotubes can be deposited by simply placing the wafer into a

solution of nanotubes. For dilute dispersions of bare nanotubes in a solvent such as DMF, leaving the wafer in the solution for ~30 s, or up to 30 minutes, will result in light to heavy nanotube coverage, respectively [21]. Fig. 3.5(c) shows a tapping-mode AFM image of SWNTs deposited onto an HMDS-treated wafer from a DMF solution over a period of 30 minutes, using the procedure described above. For nanotubes covered in surfactant or functionalized with charged groups or polymers, longer periods or alternative surface chemistries may be required. For example, to deposit negatively-charged surfactant-stabilized or functionalized nanotubes, the wafer surface may be modified to carry a net positive charge by an analogous treatment with an amine-group terminated silane such as 3-Aminopropyltriethoxysilane (AMPTS).

AFM imaging of carbon nanotubes is typically performed in tapping mode. Both individual SWNTs and bundles of nanotubes can be visualized. Useful information includes the length and diameter distribution of nanotubes in a sample, and the amount of bundling in a nanotube dispersion. Accurate diameter measurements require that only the height information be used; diameters measured from lateral dimensions can result in significant overestimates due to the finite size of the probing AFM tip. In addition, individual SWNTs sometimes look similar to small bundles. Distinguishing between them usually requires establishing a cut-off height - e.g. features <1.2 nm in height can be considered individual SWNTs, while features >1.2 nm in height are bundles [75].

Other SPM methods, such as scanning tunneling microscopy (STM) [38] and scanning conductance microscopy (SCM) [141] are also useful for nanotube imaging, but were not used in this work.

3.2.4 Electron microscopy

Both scanning electron microscopy (SEM) and transmission electron microscopy (TEM) are useful tools for studying carbon nanotubes. Both types of electron microscopes use high voltage to accelerate electrons from an electron gun towards a sample. TEM images the electrons that pass through the sample, while SEM images the electrons that scatter from the sample. SEM is therefore useful for imaging surface features of bulk samples, such as fractured sections of composites or bulk nanotube material, while TEM is used for imaging through thin (<100 nm) sample sections. SEM resolution is typically limited to a few nanometers, and is usually not sufficient to resolve individual SWNTs. However, SEM is useful for determining many properties of SWNT materials, such as the distributions of small SWNT bundles in a composite [21] or the pore structure in SWNT aerogels [22]. TEM, on the other hand, is capable of achieving sub-nanometer resolutions, and, along with AFM, is the best tool for imaging individual SWNTs. Unlike AFM, TEM can image the interior of carbon nanotubes, resolving individual graphene layers in MWNTs or other interior features such as buckyballs (C_{60} molecules) inside nanotube "peapods" [63], for example.

Three main types of electron gun designs are available [122]: thermionic, Schottky, and field emission. The thermionic gun is the oldest. It consists of a cathode that is heated to 1400-3000K. Thermally excited electrons from the Fermi level can overcome the work function ϕ_w at the surface of the material and be ejected toward the anode. Thermionic guns are frequently made from tungsten, either in the form of a sharp tip or a wire bent into a hairpin. Other filament materials include Lanthanum hexaboride (LaB_6) and cesium hexaboride (CeB_6), which are chosen for their lower work functions and lower operating temperatures. The second gun type, Schottky-emission, takes advantage of the work function dependence on electric field (Schottky effect). The work function for a given material decreases in high electric fields $\phi_{eff} = \phi_w - e\sqrt{\frac{e|\mathbf{E}|}{4\pi\epsilon_0}}$, where e is

the electron charge, and $\mathbf{E}$ is the electric field, and thus lower operating temperatures are required. This effect can be neglected in thermionic guns. In Schottky-emission guns, a very sharp (0.1 to 1 μm tip diameter) cathode is used to increase the electric field strength at the tip ($|\mathbf{E}| \approx U/r$) to values of order 10^6V/cm, significantly lowering the work function. The cathodes are usually made from ZrO coated tungsten. The cathode is surrounded by a negatively biased suppressor electrode and the electrons are extracted by applying a 4-8kV bias to an extractor anode. The third type of gun is the field emission gun. The operation of this type of gun depends on even stronger local electric fields, for example more than 10^7V/cm at a 0.1 μm diameter tungsten tip. The high fields decrease the width of the potential wall in front of the cathode to a few nanometers, and electrons from the Fermi level can escape the potential barrier through quantum tunneling, without exceeding energies to overcome the work function. Field emission guns can operate at room temperature, but are frequently heated to 1000-1500K to avoid gas adsorption at the tip. The main advantages of field emission guns are the substantially higher gun brightness and smaller effective source diameter, which translates to better resolutions with simpler optics. Field-emission SEMs usually provide resolutions of order 1 nm, while thermionic SEMs are usually limited to tens of nanometers. To obtain useful information about SWNTs from SEM imaging, a field-emission SEM is usually required.

The optics in electron microscopes are electromagnetic coils that deflect the passing electrons. Similarly to optical lenses, electron lenses suffer from spherical and chromatic aberrations, astigmatism, and diffraction. Various lens designs aim to minimize these, but all electron microscopes require significant alignment and stigmation prior to every use. This is a broad topic that is outside the scope of this thesis. Both SEM and TEM operate under vacuum, and, with the exception of so-called environmental SEMs (ESEM), samples must be dry, free of volatiles, and able to withstand

a vacuum.

Basic image formation in TEM is somewhat analogous to transmission optical microscopy. The electron beam floods the sample plane and passes through to be imaged onto a phosphorescent screen below, or onto a scintillator crystal that is then imaged by a CCD camera. In SEM, on the other hand, a focused electron beam is rapidly scanned across the sample. A detector located at an angle above the sample picks up scattered or secondary-emission electrons. The image is then reconstructed based on the instantaneous positions of the scanning beam and the number of electrons picked up by the detector.

Accelerating voltages in TEM range up to 200kV or more, and typical resolutions are of order 0.2-0.5 nm. SWNTs are best imaged at lower accelerating voltages, typically 80kV, as higher energies tend to quickly destroy nanotube samples. Sample preparation involves depositing thin slices or very small pieces of a sample onto a grid, such as "holey carbon" grids produced by Structure Probe, Inc. (SPI Supplies). The grids consist of a supporting disk, 3.05mm in diameter, typically a fine micromachined copper mesh (See Fig. 3.7(a)). The mesh is overlaid with a thin ($\sim$10 nm) carbon film. The carbon film has roughly micron-sized holes, either random in size and shape or micromachined into regular patterns (See Fig. 3.7(b)). The carbon film is mostly transparent to the electron beam and serves as a support for the sample. The holes permit imaging samples that extend over the hole without interference from the carbon film. TEM imaging requires that only very small samples are deposited onto the grid. Samples are deposited onto the side of the disk covered by the carbon film, which typically appears less shiny than the uncoated side. For solid samples, slices 100 nm thick or less are cut using a microtome. Powder samples should be finely ground in an agate mortar and very lightly sprinkled over the grid. It is not necessary to see the powder on the grid - any piece visible with the naked eye is too large to be imaged well in the

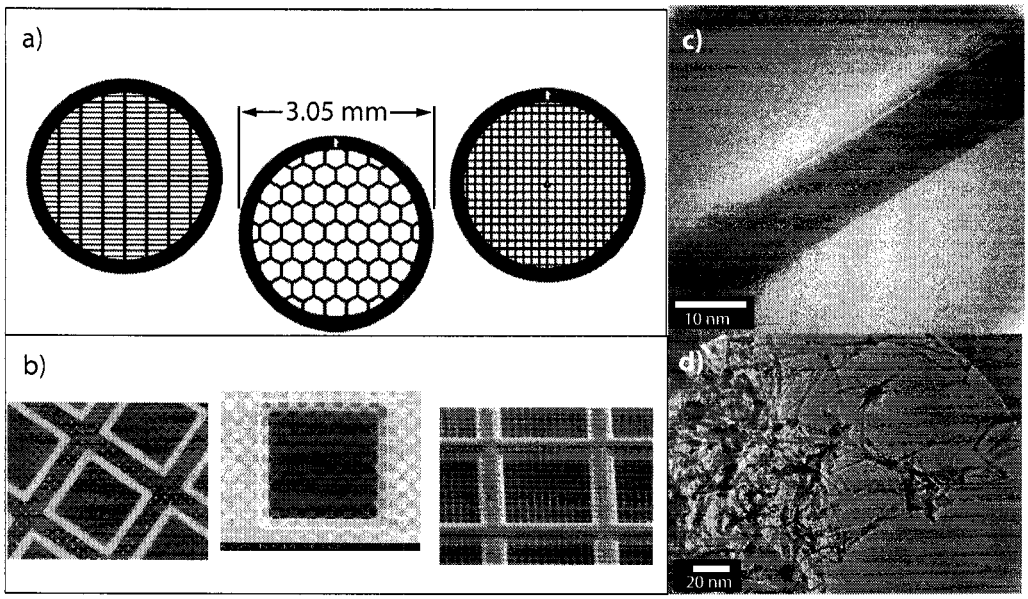

Figure 3.7: Holey carbon TEM grids. a) some patterns of the micromachined support disks. b) Optical (left) and SEM (center and right) images of the carbon films on holey carbon TEM grids. These examples feature microfabricated films with regular hole patterns. c) TEM image of a MWNT. Individual graphene layers are clearly visible. d) TEM image of a cluster of SWNTs over a hole on a holey carbon grid. The supporting carbon film is visible in the top right corner of the image.

TEM. Liquid samples can also be deposited onto the grid and dried out. For SWNT suspensions, the suspension should be diluted to a SWNT weight fraction of $\sim 10^{-6}$, and a drop of the dilute solution applied to the grid and dried. CNT aerogel samples were successfully deposited onto TEM grids by shredding (pulling apart) larger aerogel pieces held a few cm above a grid. TEM images of a MWNT and entangled SWNTs are seen in Fig. 3.7(c) and (d).

SEM accelerating voltages are lower than those used for TEM, typically 5-25kV. Carbon nanotubes are frequently best imaged at $\sim$10kV, but this can depend on the sample. Unlike TEM, SEM can image large and thick samples. Samples are mounted on aluminum posts with the use of electrically conducting tape (e.g., carbon tape), or conducting glue. The samples themselves must also conduct electricity to prevent charge buildup from the incident electrons. Insulating samples are

coated with a thin conductive layer prior to imaging. Coating is performed by sputtering or evaporating gold, gold-palladium (Au-Pd), or carbon. Sputtering is the simplest and quickest coating method, while evaporation can provide more uniform coatings with better adhesion. In sputtering, a sample is placed in a vacuum chamber. The chamber is pumped out with a roughing pump, and purged with Argon to a pressure of $\sim$0.1 Torr. The Argon is ionized to form a plasma by applying a potential between a cathode made of the coating material (e.g., gold) and an anode on which the sample is placed. Argon ions strike the cathode target, ejecting small metal particles. These particles are then deposited on the anode and other surfaces, including the sample. Sputtering is quick. The rough pumpdown takes only a few minutes, and the coating is usually done in under one minute. Typically, gold or Au-Pd targets are used. Au-Pd provides more uniform coatings with better adhesion, but cannot be removed after imaging. For samples that have to be reclaimed, a gold coating is usually preferred, since it is easily removed with a chemical gold etch. Evaporation provides higher quality coatings but is significantly more time consuming. A sample is placed into a vacuum chamber and evacuated to high vacuum. High vacuum ($<10^{-5}$ Torr) is achieved with the sequential use of roughing, turbo, and cryogenic or diffusion pumps, and the process requires several hours. A crucible or tungsten "boat" containing the coating material is heated above the boiling temperature of the material either by applying a current across the boat or by bombardment with a strong electron beam. Heating must be done slowly, since rapid heating causes thermal stresses, potentially destroying the crucible or boat. This is the most common error made with evaporation, and is usually quite costly. The heated material evaporates and coats all line-of-sight surfaces within the chamber. Layer thickness is monitored by an oscillating crystal, whose oscillation frequency decreases as it is coated with the evaporated material. For SEM imaging, coatings of 5-10 nm in thickness are usually adequate. Carbon nanotubes are electrically conductive, and

therefore do not require coating by themselves. However, coating is usually required when looking at polymer composites, for example. In our SEM studies of epoxy composites, the samples were coated with a sputtered layer of Au-Pd. The carbon nanotube aerogels described in this thesis did not require coating.

3.2.5 Energy-dispersive x-ray spectroscopy

Energy-dispersive x-ray spectroscopy (EDX or EDS) is a method used to identify the chemical composition of samples from x-ray energy spectra [122]. Among many other uses, it can determine the types of impurities present in a nanotube sample prior to purification. In our experiments, EDX was used to establish the efficiency of various methods in removing dry surfactant from aerogel samples. EDX is frequently implemented as an extension of scanning electron microscopy, often built directly into scanning electron microscopes, but is also available in stand-alone units. When accelerated electrons hit a sample, the sample can become ionized by ejecting an inner-shell electron to create a void. The void is filled by a higher-energy electron from an outer electron shell, and an x-ray is emitted in the process (see Fig. 3.8(b)). The energy of the emitted x-ray is the de-excitation energy between the two states, and is unique to the element. Multiple x-ray lines arise from the different possible transitions for each element. They are frequently classified by Siegbahn notation, according to the electron shell in which the ionization occurred, followed by a Greek letter and numerical subscript attributed to the spectral line. Frequently, the strongest observed line is denoted α, and corresponds to transitions between the nearest shells, but the notation is not entirely consistent or intuitive. Electron shells are labeled alphabetically, beginning with the letter K, and are defined by the principal quantum number n: K (n=1), L (n=2), M (n=3), etc. Each electron shell with $n > 1$ has multiple energy levels that depend on the azimuthal (quantum

number l) and total angular momentum (quantum number j) of the states. For example, Kα_1 transition corresponds to an electron in the L shell with l=1, j=3/2 (the third and highest energy level in the L shell, or L_{III}), filling a void in the K shell. The energy of the Kα_1 transition depends on the atomic number and, along with other spectral lines, can be used to identify elements. Typical electron energies used for EDX are 10-20kV, so the upper limit of the emitted x-rays is also 10-20keV. Energies below $\sim$100eV are not resolvable. Boron is the lightest element with resolvable spectral features, at atomic number $Z = 5$. All heavier elements up to uranium ($Z = 92$) can be identified within this energy range. Carbon, with $Z = 6$, has a resolvable Kα_2 transition at 282eV (see Fig. 3.8(a)). This is the only spectral line for this element. In the 10-20kV energy range, the electrons typically penetrate $\sim$0.5-2 μm into a sample, depending on sample type and density. X-ray emission is therefore also confined to this skin depth. An example of an EDX spectrum obtained for NaDDBs surfactant coated SWNTs is shown in Fig. 3.8(c).

Quantitative elemental analysis that gives relative proportions of each element in a sample can be obtained. Usually, the process is automated within the EDX software. The most common algorithm for extracting quantitative information is called "ZAF", for Z (atomic number), absorbance, and fluorescence. The algorithm fits a Gaussian curve to each spectral line, determines the area under the curve, and then compensates for known variations in emission according to the atomic number and interactions between the elements due to absorbance and fluorescence. Another, significantly more difficult method uses standard samples for calibration.

Another useful feature of EDX is the ability to create element maps of a sample. Since the analysis is typically done in an SEM, the SEM image can be overlaid with a corresponding image map for each element. Thus, the precise location of each element in a sample can be obtained, down to the resolution of the SEM.

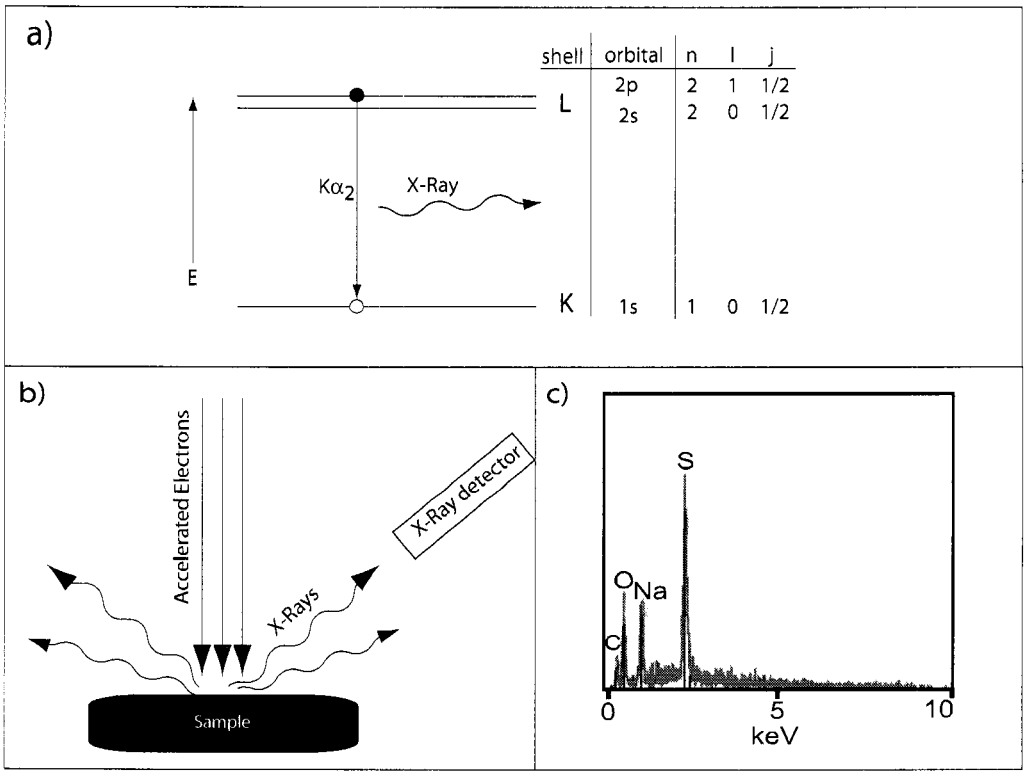

Figure 3.8: Energy Dispersive X-ray spectroscopy (EDX). a) The $K\alpha_2$ transition in carbon. A void created in the K electron shell is filled by an electron from the L shell, releasing an X-ray in the process. The quantum numbers, n, l, and j that correspond to the energy levels are also shown. b) Electrons are ejected from the sample by a beam of high-energy electrons, such as those from a scanning electron microscope, emitting x-rays in the process. An EDX X-Ray detector is mounted above the sample. c) Example of an EDX spectrum of NaDDBs-coated SWNTs. The presence of carbon, oxygen, sodium, and sulfur peaks are consistent with the composition of the surfactant.

The most common type of EDX detector is the silicon drift detector, or SiLi, so called because the silicon is doped with lithium. An x-ray incident on the semiconductor generates a photo-electron. As the photoelectron travels within the material, it generates electron-hole pairs, whose number depends on the photoelectron energy. The generated electrons and holes travel to opposite ends of the silicon under a strong electric field. The corresponding current depends on the energy of the incident x-ray. To reduce electronic noise, the detector is typically cooled with Peltier coolers or liquid nitrogen.

3.2.6 Optical microscopy

The resolution of optical microscopy is limited by the diffraction of visible light. As such, objects smaller than a few hundred nanometers cannot be resolved, including individual nanotubes. Nonetheless, optical microscopy can be useful for quickly evaluating nanotube dispersions and for characterizing bulk features, such as nanotube aggregates or agglomerates [21], or nematic ordering [72]. Since carbon nanotubes strongly absorb light in the visible spectrum, bulk quantities are easily observed. Bright-field, transmission mode optical microscopy is best suited for observing carbon nanotubes.

3.2.7 Optical absorption

The optical absorbtion spectrum of SWNTs in solution can be used to quantify the relative proportions of carbon nanotubes to other carbonaceous impurities in a sample, but only in relation to a reference sample which is assumed to be "pure" [76].

Near-infrared (NIR) absorption spectra of SWNTs have prominent features associated with transitions between the principal mirror spikes in the electronic density of states (DOS) [83]. The strongest observed transitions are $S_{11}=2a\beta/d$ and $S_{22}=4a\beta/d$ for semiconducting SWNTs, and $M_{11}=6a\beta/d$ for metallic SWNTs. Here, a is the carbon-carbon bond length (0.144 nm), β is the transfer integral between pπ orbitals ($\sim$2.9 eV), and d is the SWNT diameter in nanometers. The S_{11} transition is observed at $\sim$5500 cm^{-1}, S_{22} is at $\sim$9800 cm^{-1}, and the M_{11} transition is at $\sim$13800 cm^{-1}. Since many types of SWNTs (chiralities and diameters) contribute to the signal in a typical sample, the peaks are usually broad, of order 2000-3000 wavenumbers, and can be shifted somewhat depending on the type of SWNTs used. The peaks are superimposed on a linearly increasing background that is common to all forms of carbon. The NIR spectra of other

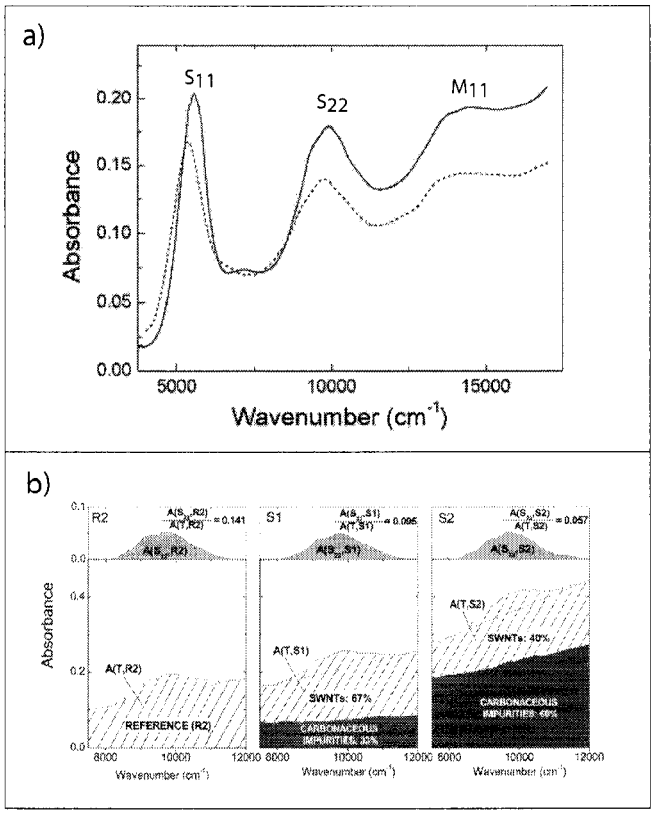

Figure 3.9: Near-IR Absorption spectra of SWNTs from Ref. [76]. a) Absorption spectra of two SWNT samples of different purity. The S_{11}, S_{22}, and M_{11} peaks are evident. The solid line is the sample with a higher purity. b) Quantitative analysis of the S_{22} peaks of three different samples to determine the content of the carbonaceous impurities. The reference sample is on the left and is assumed to be 100 % pure. The middle and right samples are compared against the reference sample to obtain relative purity (see text).

forms of carbon, however, do not exhibit the transition peaks. The absorption instead increases linearly with increasing wavenumber.

Any of the above three transitions can be used to evaluate purity, but S_{22} is usually chosen. The S_{11} transition is more sensitive to doping and other chemical changes than the S_{22}, such as the changes that result from acid purification, and is therefore less useful for tracking the purification process. The M_{11} transition is usually broader and less pronounced than the other two.

Quantitative analysis of the carbonaceous impurities requires a reference sample whose purity is assumed to be 100%. The total area under the S_{22} peak is first computed for the reference

sample. A linear baseline subtraction is then performed, as shown in Fig. 3.9(b). The area under the curve of the S_{22} peak after the baseline subtraction is then found. The ratio of the two areas, i.e., the ratio of area of the S_{22} peak without the background $A(S_{22},R2)$ to the total area under the peak, A(T,R2), where R2 is here the name of the sample, is then found. For the reference sample R2, this ratio is 0.141 as seen in the left plot of Fig. 3.9(b). This ratio decreases linearly with decreasing sample purity, as the background signal from other forms of carbon increases. To determine the purity of an unknown sample, an identical calculation is performed. For example, the ratios for unknown samples S1 and S2 (middle and right plots in Fig. 3.9(b)) are 0.095 and 0.057. The SWNT content is simply the ratio of the value for the unknown sample to the reference sample, for example 0.095/0.141 = 0.67 for the middle plot in Fig. 3.9(b).

The significant drawback of this method is the need for a 100% pure reference sample. The R2 sample and the computed ratio of 0.141 presented here has become a somewhat standard reference used in the nanotube community, but its purity is not 100% as assumed. As SWNT production and purification methods have since improved, it is not uncommon to see quoted SWNT purities significantly exceeding 100% with respect to the R2 reference. These strange results stem from applying the above formula to samples of higher purity than the reference, and while this is not a perfect standard, it does permit cross-comparison of SWNT material between different research groups.

3.2.8 Fluorescence

Fluorescence is the emission of light from a material upon excitation with another, usually higher-frequency, light source. A molecule can absorb a photon by becoming electronically excited, i.e., by moving an electron to an excited state. Fluorescence occurs when the molecule then relaxes

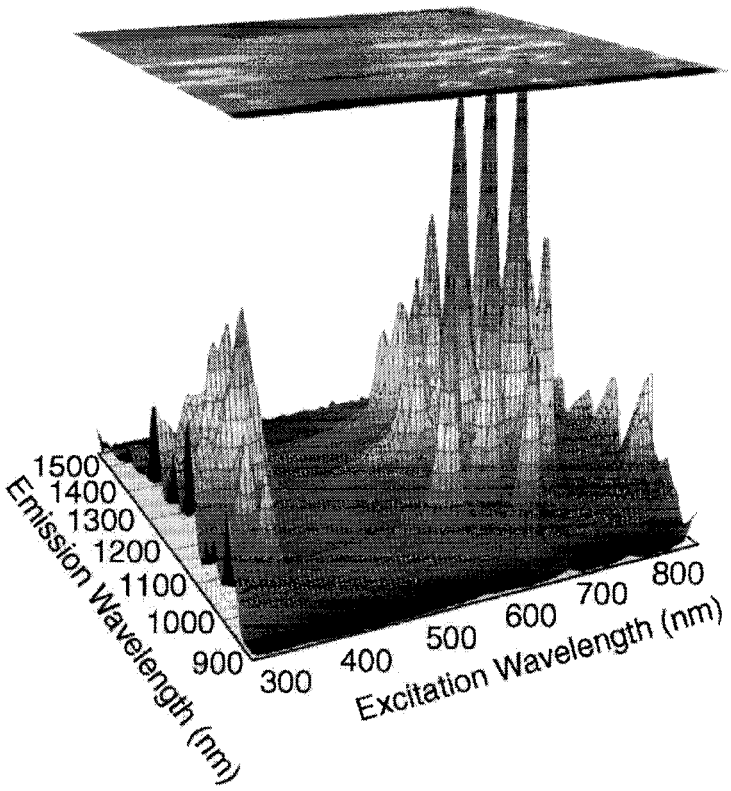

Figure 3.10: Fluorescence map of SWNTs in a sodium dodecyl sulfate suspension from reference [80]. Each peak represents a distinct (n,m) nanotube species.

back to its ground state by emitting another photon. Semiconducting SWNTs have been shown to fluoresce in the near-infrared region [8, 56, 110] upon excitation with a laser. In many semiconducting materials, fluorescence is a result of electron-hole recombination across the bandgap, but this picture is not consistent with some experimental observations of SWNT spectra. An alternative picture was proposed by Eugene Mele and Charles Kane at Penn [82], among others, which suggests that the fluorescence in carbon nanotubes is due to a decay of excitons, and not the recombination of unbound electron-hole pairs. The theory has been confirmed experimentally [152], and is now generally accepted by the nanotube community. Excitons are quasi-particles consisting of bound electron-hole pairs. As a result, an exciton has slightly less energy than an unbound electron

and hole pair, and may also have several possible energy levels.

Exciton energies are tied to the band structure of SWNTs, and differ depending on SWNT chirality. Spectral measurements of the fluorescence of isolated SWNTs, like the measurement shown in Fig. 3.10, permit the identification of individual SWNTs by their (n,m) indices. Here, individual SWNTs are dispersed in dilute solution with SDS surfactant. The excitation wavelength is varied, and the emission spectrum is taken at each excitation wavelength to create a map. Each peak corresponds to a resonance within an individual (n,m) SWNT species. The indices of the SWNT producing each peak can be identified from the exciton model. SWNT bundling disturbs the electronic structure of individual nanotubes, and can be detected in fluorescence spectra as a broadening of the peaks, or by their absence [110].

3.2.9 X-ray diffraction

In x-ray diffraction, a collimated beam of x-rays is passed through a sample and the resultant diffraction pattern is imaged. The diffraction pattern contains information about the structural properties of the sample near the atomic level. This simple but powerful technique can be used to identify the type of crystal lattice and determine the spacing between crystalline planes. Among its many successes, x-ray diffraction was used to determine the double-helical structure of DNA from crystallized DNA samples, and is also instrumental in determining the structures of complex molecules such as proteins [6].

For samples with well-defined periodic (crystalline) structures, the diffraction pattern contains sharp peaks that are a result of Bragg's law. Constructive interference of x-rays diffracted by successive planes of a crystal produce maxima at points where the Bragg condition $2dsin(\theta) = n\lambda$ is satisfied. Here, d is the spacing between the crystal planes, θ is the scattering angle, and λ is the

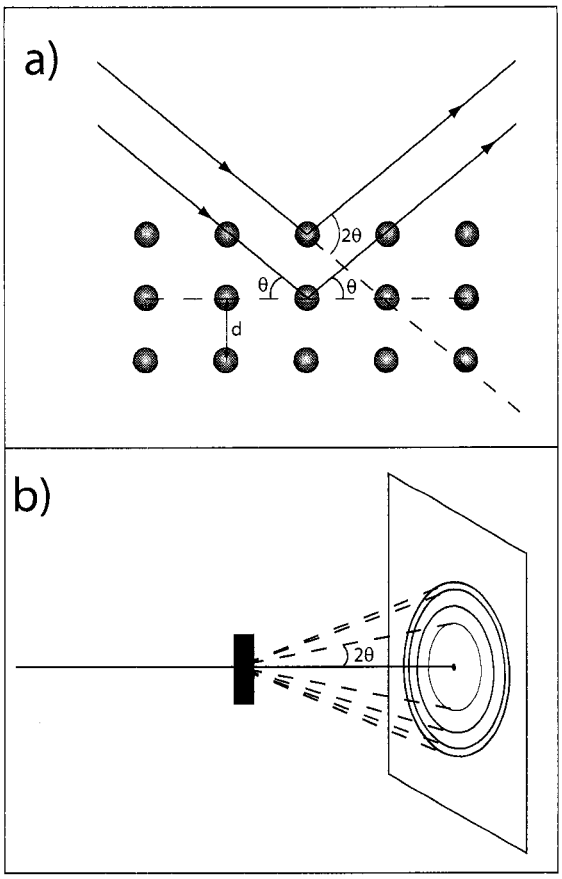

Figure 3.11: a) Schematic of x-rays scattered from a crystal structure. X-rays incident on successive crystal planes interfere constructively when the Bragg condition, $2d\sin(\theta) = n\lambda$, is satisfied, forming a bright spot in the diffraction pattern. b) Typical ring diffraction pattern from a powder scattering measurement.

wavelength of the x-rays, as shown in Fig. 3.11.

Glassy or amorphous samples, on the other hand, lack the exact periodicity of crystals. However, some characteristic spacing is also frequently present. Signatures of amorphous materials appear as broad peaks in the diffraction spectrum. The location of the peak determines the average spacing of atoms in an amorphous sample, while the width reflects the amount of deviation from the mean.

X-ray diffraction is frequently classified into Wide Angle X-ray Scattering (WAXS) and Small Angle X-ray Scattering (SAXS) to differentiate between diffraction patterns observed at large and

small angles from the incident beam. The two types of scattering usually require different equipment or configurations. WAXS probes the crystalline structure of materials at length scales of order 0.1 to a few nanometers, and is useful for determining atomic structures. SAXS probes larger length scales of tens to hundreds of nanometers and can be used to determine the structures of porous networks like aerogels, for example.

A common x-ray scattering technique is powder diffraction which looks at powdered or microcrystalline samples. As opposed to diffraction from a single crystal, where each crystallographic plane can be imaged independently, diffraction patterns of powdered samples depend on the particles being randomly oriented and probe all the possible crystallographic directions at once. A monochromatic x-ray source is typically used. To obtain good statistics, meaning that all possible orientations are indeed probed, many thousands of particles are required and the sample is often rotated about its axis during exposure. Powder diffraction patterns appear as concentric rings centered around the direction of the incident beam. The distance from the center of the pattern to each ring and the distance from the sample to the detector determines the scattering angle from a particular crystal plane. This angle is typically denoted as 2θ, where θ corresponds to the angle defined by Bragg's law. The factor of 2 is a result of the fact that the angle is measured with respect to the incident beam, and not the orientation of the crystal plane, as seen in Fig. 3.11. The spacing between the crystallographic planes can then be determined from Bragg's law.

In carbon nanotube samples, powder diffraction scattering can be used to determine the crystallinity of SWNTs in ropes, and can be used to estimate the amount of graphitic and amorphous carbon impurities. In general, the method can detect phases in the sample that are present in quantities above 5 wt%. The signature of graphite is observed at 3.4 Å, which corresponds to the spacing between the graphitic planes. The presence of this peak in SWNT samples implies the presence

of graphitic impurities or MWNTs, where spacing between the walls is the same as in graphite. Amorphous carbon is observed as a broad peak around 1.5Å, which is a typical carbon-carbon bond length. The peak is broad since amorphous carbon contains sp^2 and sp^3 bonds, as well as numerous "dangling" bonds that are not connected to other carbon atoms to form a lattice. Other features may be evident, for example, from buckyballs (e.g., C_{60} molecules), whose diameters are smaller than SWNTs, down to about 4 Åand metal catalyst particles at. The absence of these features in a SWNT sample implies that the carbonaceous impurity is less than 5 wt%.

Small-angle X-ray scattering (SAXS) is, in principle, appropriate for studying the structure of SWNT suspensions and networks, but the data can frequently be confusing or misleading. The length scales involved in measurements such as determination of the mesh size of nanotubes in a gel or the shape of the nanotubes in solution are of order tens to hundreds of nanometers, which falls within the SAXS regime. Of particular importance in this thesis is the question about whether gels and suspensions of SWNTs may be modelled as hard-rod systems. The scattering intensity, I, of isolated hard-rods with diameter d and length L in solution should scale with the scattering wave vector Q ($Q = 2\pi/\lambda$) as Q^{-1} in the regime $2\pi/L < Q < 2\pi/d$ [163]. In contrast, flexible rods or polymers should produce a scattering profile with a slope of Q^{-2}, while point-like objects produce Q^{-4}. Fig. 3.12(a) shows the results of a SAXS measurement of a carbon nanotube aerogel that contains no other material besides nanotubes (0.75 wt% CNT, see Chapter 7). The scattering intensity falls off nearly as a power law with scattering angle, but while a Q^{-1} or a Q^{-2} behavior might have been expected, a fit to the curve in Fig. 3.12(b) reveals that the exponent is closer to -2.7. One interpretation for this anomaly is that strong scattering from point-like catalyst particles on the nanotubes, which by itself would produce a Q^{-4} profile, contributes here to the larger exponent. It is thus not possible to determine the structure of the gel. Anomalous exponents are

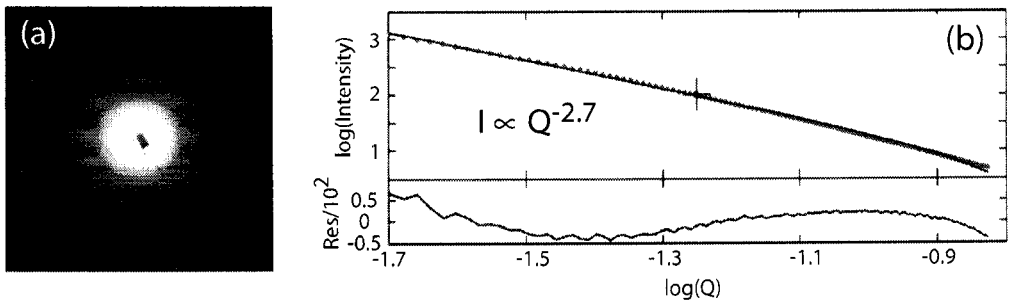

Figure 3.12: a) Raw SAXS data from a critical-point dried nanotube aerogel (0.75 wt% CVD CNT, 0% PVA, ~5 wt% catalyst) from which the surfactant has been removed with water. b) log-log plot of the intensity profile vs. scattering vector, Q, of the image in (a). The plot is nearly linear with a slope of -2.7. Bottom part of the plot shows the residuals of the fit.

also observed in SAXS patterns of surfactant-stabilized suspensions of nanotubes. Fig. 3.13 shows the SAXS intensity for several concentrations of NaDDBs-dispersed HiPco SWNTs. Here, the catalyst content is very low (< 0.7 wt%), but the intensity still falls of as Q^{-2}. Since carbon does not scatter X-rays strongly, it is believed that the scattering contribution from the carbon atoms within the surfactant interferes with the nanotube signal.

Therefore, while SAXS can, in principle, determine the structure of nanotube gels and suspensions, we did not have much success with this method. A complementary technique more appropriate for these systems is small angle neutron scattering (SANS), which will be described in the next section.

3.2.10 Small Angle Neutron Scattering

The de Broglie wavelength of neutrons can be varied within a range similar to the wavelength of X-rays by modifying their momentum. Neutron scattering is therefore a complementary technique to X-ray scattering, able to probe similar length scales, but with several differences.

In contrast to X-rays, which scatter from the electron shells of atoms, neutrons scatter from atomic nuclei and the scattering cross section does not depend on the atomic charge. However, the

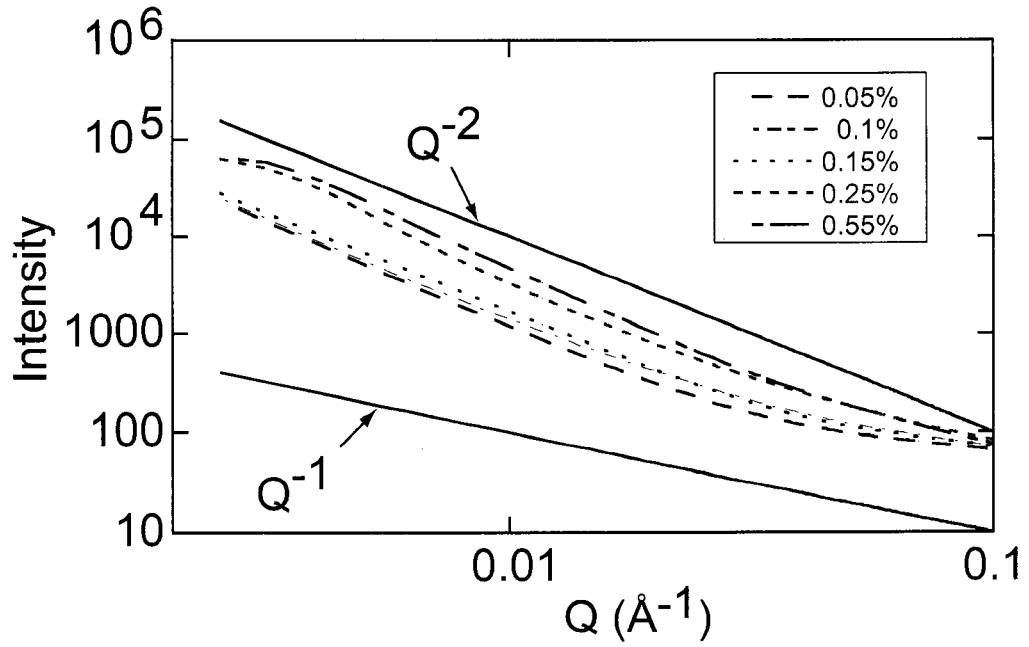

Figure 3.13: Log-log plot of SAXS intensity profiles for NaDDBs-dispersed HiPco SWNT gels. The catalyst content is < 0.7 wt%. Q range corresponds to real-space lengths of $\sim$5.5 to 250 nm. Throughout most of this range ($\sim$17-250 nm), the scattering intensity falls off as Q^{-2}, which is inconsitent with hard-rod scattering. This may be due to interference from the surfactant or to catalyst particles.

scattering cross section can vary significantly from one isotope to another. Neutron scattering is more appropriate for studying lighter elements such as carbon, especially in the presence of heavier atoms, such as iron catalyst. Since neutrons are not charged, they can also penetrate much deeper into the sample than X-rays.

Small angle neutron scattering (SANS), a method analogous to Small Angle X-ray Scattering (SAXS) described above, has been successfully used to probe the structure of nanotube suspensions [163]. Fig. 3.14 shows the scattering intensity versus wave vector Q, revealing the Q^{-1} behavior characteristic of hard-rod suspensions for Q between 0.003 and 0.02 $Å^{1}$, which corresponds to 31-160 nm in real-space. 160 nm is comparable to individual measurements of the nanotube length. At lower Q, i.e., longer lengths, a Q^{-2} scaling is observed. This may be connected to tube-tube

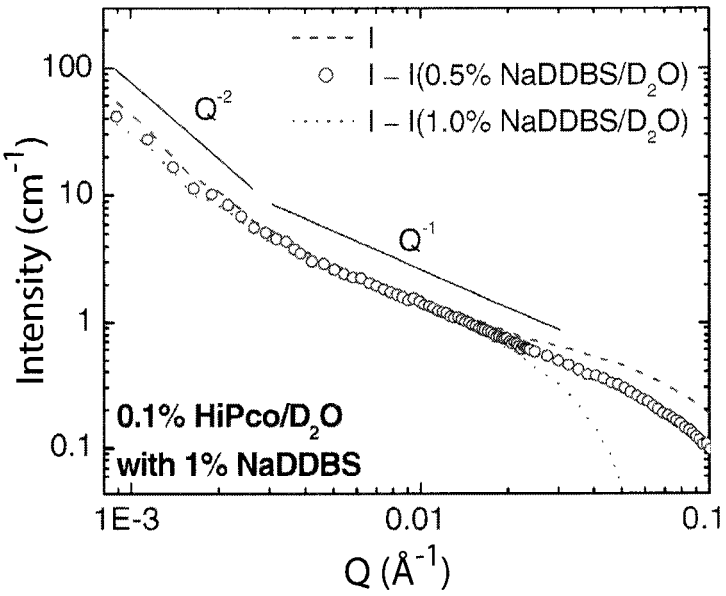

Figure 3.14: SANS scattering of SWNT dispersion from Reference [163]. Data is for a 0.1% HiPco SWNT solution dispersed with 1% NaDDBs surfactant. The curve reflects the scattering intensity after subtraction of the surfactant contribution, with the assumption that some surfactant is adsorbed onto the nanotubes while some remains as free micelles in solution. Dashed and solid lines reflect extreme assumptions of no excess surfactant in solution and no surfactant on nanotubes, while solid circles represent the best intermediate assumption. The curve reveals a Q^{-1} scaling for Q between 0.003 and 0.02 $Å^1$ (31-160 nm) and Q^{-2} scaling at lower Q (larger lengths).

interactions which lead to the formation of a loose 3-D network at long length scales. This network may be somewhat akin to the semi-dilute phases of flexible polymer solutions.

These data show that SWNTs in solution may indeed be modelled as hard-rod systems, in turn enabling us to extract useful information about percolating nanotube networks described in this thesis.

3.3 SWNT purification

As-produced carbon nanotube material contains many impurities, including non-nanotube forms of carbon and metallic catalyst particles. Depending on the process used to synthesize the nanotubes, non-nanotube carbon, such as buckyballs, amorphous carbon, and planar graphite, can account

for a significant part of a batch, sometimes exceeding the nanotube content itself. Heavy catalyst particles are present in significant quantities in all raw SWNT material. For example, as-produced HiPco SWNTs (Carbon Nanotechnologies, Inc.) are sold with the claim of <25 wt% iron content. Our characterization of HiPco batch R0519 by Thermogravimetric analysis (TGA) reveals iron content ~26 wt% (see Fig. 3.17). Purification typically refers to the removal of the non-nanotube carbonaceous material and metallic impurities. Due to the low purity of raw materials, and the inevitable loss of some nanotubes during the process, as much as 80-90% percent of the starting mass is usually lost during purification.

Various nanotube purification methods have been developed [38, 100, 124], most involving an acid treatment to dissolve the metallic impurities and oxidizing treatments to remove the non-SWNT carbonaceous material. Other purification approaches include laser irradiation [9] and H_2O Plasma treatment [68] for removing amorphous carbon, and magnetic fractionation by flowing a SWNT suspension over a strong magnet [74] to remove iron particles.

After purification, the SWNTs are frequently subjected to a high-temperature anneal in vacuum to repair damage from the purification procedures [77].

Different SWNT types usually require different purification approaches that depend on the type of impurities (e.g. type of catalyst) and initial SWNT content. Since the composition of raw SWNT material can differ significantly from batch to batch, even for the same type of nanotube, it is important to characterize the material prior to purification and keep track of the composition during purification, adjusting the procedure as necessary to obtain optimal results.

Current purification methods are not standardized, with different research groups using different approaches, and the methods are rapidly evolving. Notably, whereas earlier purification

techniques involved very aggresive treatments, including refluxing (boiling) the SWNTs in concentrated nitric and sulfuric acids (HNO_3 and H_2SO_4)for 48 hours [124], newer procedures call for a brief (<30 min) reflux in dilute nitric [77] or hydrochloric acids [164]. This trend toward gentler treatments is a reflection of both higher quality SWNT material and optimization of the purification procedures.

In our samples, purification typically starts with pulverizing the raw material in an agate mortar, followed by a wet air burn with hydrogen peroxide (H_2O_2). The material is then refluxed in dilute nitric acid, followed by a second reflux in hydrogen peroxide [77]. The last two steps are repeated several times as necessary. Finally, the nanotubes are subjected to a high temperature anneal [77] and magnetically fractionated to remove remaining magnetic catalyst [74]. A flowchart of a typical purification procedure is shown in Fig. 3.15. The electrical properties of the purified SWNTs are not significantly affected by purification [77]. The following example for HiPco SWNTs will serve to elucidate the process. The purification described here was only marginally successful, but it serves to illustrate the details of the process and to elucidate the challenges and judgement calls associated with the process.

3.3.1 HiPco purification example

Two grams of raw HiPco, batch R0519, was obtained from Carbon Nanotechnologies, Inc. The material is shipped as "fluff", a very light powder that is readily carried away by slight air currents, and therefore very difficult to work with. The material was transferred to a glass jar containing a small amount of water ($\sim$1 cm on the bottom). The procedure was done in a sealed glove box. The jar was then lightly capped, removed from the glove box, and placed on a hot plate to boil. After about 15 minutes of boiling, the SWNT fluff was saturated with water. The water was then

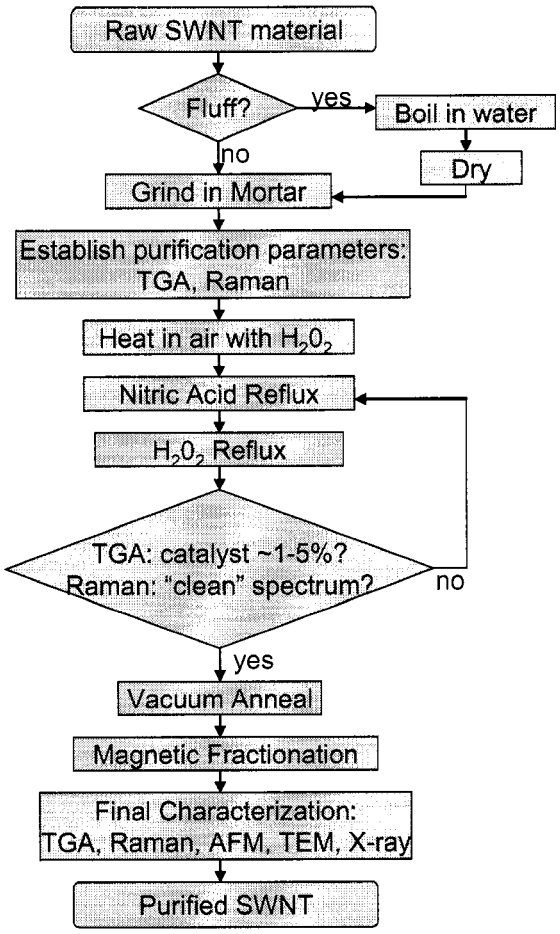

Figure 3.15: Flowchart of a typical purification procedure. After purification, the nanotubes may be dispersed according to the procedure in Fig. 3.2.

evaporated off, resulting in a hard nanotube cake. The cake was pulverized in an agate mortar to a fine powder. Small samples (~3 mg) were characterized by TGA (Fig. 3.17) to determine the catalyst content.

TGA analysis revealed that maximum mass loss occurred between 300-400°C. An increase in sample mass below 300°C was also observed, and is likely due to oxidation of the iron catalyst particles. ~37% of the initial sample mass remains at high temperatures, suggesting iron catalyst content of ~26 wt% if complete oxidation of the iron is assumed (see section on thermogravimetric analysis in this chapter).

Throughout the purification process, the sample is divided into smaller parts and each step of the process is tested on a fraction of the total sample to hedge against potential mistakes.

The first step in the purification aims to expose iron catalysts to acid treatment by removing some of the encapsulating carbon material. The SWNT material is saturated with 30% hydrogen peroxide solution in a ceramic crucible, and placed in a furnace. The furnace temperature is chosen based on the initial TGA data to be close to, but below, the vaporization temperature of the sample. The Hydrogen peroxide improves oxidation and is thought to enhance the vaporization of amorphous carbon. Initially, a 0.5 g portion of the sample was placed in the furnace at 300°C for 5 hours. This temperature turned out to be too high, with more than 90 % of the carbon mass being vaporized (as determined subsequently by TGA), and this portion of the sample was abandoned. Subsequently, the remaining 1.44 g of the sample was placed in the furnace at 250°C for 3.5 hours. The mass of the sample increased to 1.52 g (~6%), presumably due to oxidation of some of iron catalyst. In retrospect, this may have been sufficient for the initial step, since the mass gain indicated that a significant portion of the catalyst was exposed to oxidation. However, the furnace temperature was instead increased to 275°C, and the sample was baked overnight. The sample mass decreased to 0.78 g (~54% of the initial value), which is much larger than the few-percent loss that was aimed for.

The SWNT material was then subjected to reflux in nitric acid. This step is potentially dangerous. Although only moderately concentrated acid is used here, nitric acid easily forms explosive compounds when mixed with common materials such as cellulose. Refluxing (boiling) the acid increases its reactivity and releases dangerous fumes. Therefore, special precautions must be taken. For completeness, it should be noted that, when diluting any concentrated acid, the acid should be poured slowly into a container of water, never the opposite. Water should not be poured into acid

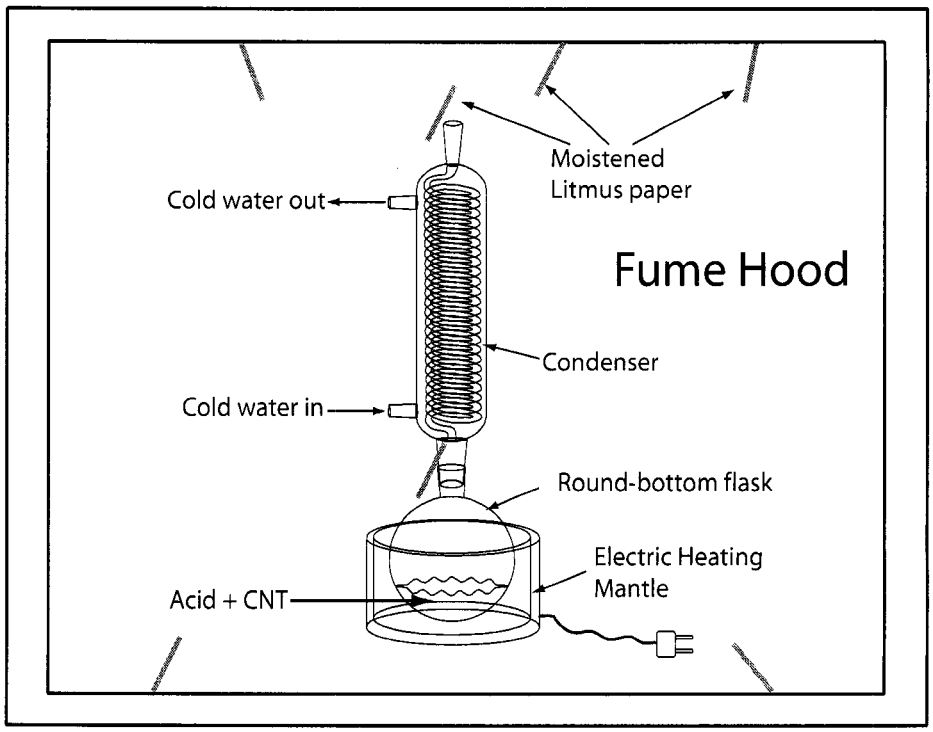

Figure 3.16: Setup for performing acid reflux during carbon nanotube purification.

since strong heating can cause splashing or an explosion. A schematic of the acid reflux setup is shown in Fig. 3.16. The reflux was performed inside a fume hood. A round-bottom Pyrex flask containing the acid was connected to a condenser through which cold water was circulated. This captured most of the emitted acid fumes. The top of the condenser was open to the air to prevent pressure buildup. The flask was placed inside an electric heating mantle that closely matched the dimensions of the flask. Litmus papers moistened with water were taped to the setup near places where acid fumes were most likely to be emitted. This included the open condenser top, the connecting joint between the flask and condenser, and in several places along the access window at the front of the fume hood. The litmus paper was monitored throughout the reflux procedure for the presence of acid. 0.521 g of the sample left from the last step was placed in a 300 mL round-bottom Pyrex flask with 75 mL of 2.5M HNO_3 (nitric acid). Typically, $\sim$150 mL of acid per gram

of SWNT material is used [124]. The acid was brought to a slow boil, and boiling continued for 20 min. The acid was then cooled and decanted from the SWNT material. The remaining acid and SWNT material were diluted with water to the capacity of the bottle, and neutralized to pH 7 with NaOH pellets. The product of this reaction is $NaNO_3$ (a food preservative and a component of gunpowder) and water, and can be safely discarded. Dissolved iron re-precipitates upon neutralization, so it is advantageous to decant as much of the acid as possible prior to neutralization. After neutralization, the SWNTs were filtered through a fine stainless steel mesh ($\sim$150 μm grid), and rinsed with water. The mesh retained virtually all of the SWNT material while allowing the solvent and any precipitated iron to pass through.

The SWNT material was again placed in the reflux setup. This time, 75 mL of 30% hydrogen peroxide (H_2O_2) was used in place of nitric acid, and the solution was refluxed (boiled) for ten minutes. This process aims to dissolve more carbonaceous material. As before, the SWNT were filtered through the stainless steel mesh and rinsed with water. After the acid and peroxide refluxes, the mass of the sample was 0.162 g. About 70% of the sample mass was lost during the acid and peroxide reflux.

A small ($\sim$3 mg) sample of the material was taken and TGA was performed. The TGA curve, shown in Fig. 3.17, shows that the metal particle content decreased to $\sim$12 wt%, assuming full oxidation of the iron. The initial mass loss at low temperatures ($<100^\circ$C) is due to water, meaning that the sample was not properly dried prior to the TGA measurement. To compensate for the presence of water in estimating the metal particle content here, the initial CNT mass was taken to be the mass measured at 150°C, not at room temperature. Note that the vaporization temperature of the carbon decreased slightly from the raw material. Since less catalyst is present, the decrease suggests that the nanotubes and other stable forms of carbon were damaged during the reflux and

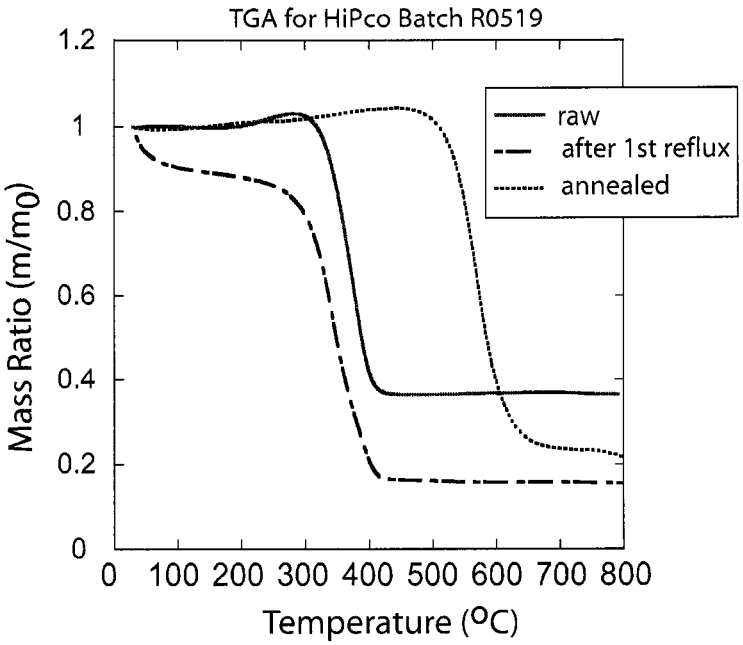

Figure 3.17: Three TGA curves obtained during purification of HiPco batch R0519.

thus oxidized more readily.

The same SWNT material was again refluxed in nitric acid and peroxide, as above. After the second reflux, the sample mass was 0.10 g, down from 0.18 g, a 44% loss.

After the second reflux, the sample was placed in a vacuum furnace and a high-temperature anneal was performed. A graphite crucible was used to contain the SWNT material. The sample was slowly heated to 200°C over a period of two hours (drying). The temperature was further increased in steps up to 1150°C, and held at this temperature for 1.5 hours. The furnace was then allowed to cool overnight. In the absence of oxygen, SWNT do not vaporize (Carbon sublimates above 3727°C). 1150°C is near the temperature at which the nanotubes were initially produced, and it is believed that the carbon-rich environment provides a certain amount of carbon vapor that can 'repair' damage done during the purification process.

A third TGA measurement was performed after annealing (see Fig. 3.17. As expected, temperature at which the SWNT vaporized increased by about 200°C over the raw and refluxed material to 500-600°C. The increased vaporization temperature can be attributed to two effects. First, remaining catalyst particles are likely all oxidized and therefore don't lower the apparent vaporization temperature as they did in the raw material. Second, since the catalyst particles were likely already oxidized after the reflux phase when no increase in vaporization temperature was observed, the increase here suggests that the annealing process successfully repaired the SWNT damage caused during reflux.

Two unexpected features are seen in the curve of the annealed SWNTs, however. First, a slight increase in mass is observed prior to the vaporization of carbon. Second, the remaining mass at high temperatures is greater than that in the refluxed samples, and appears to decrease even above 750°C. Both of these features are not consistent with oxidized catalyst particles, which are expected to remain inert throughout the heating, and most likely suggests that some unanticipated impurity was introduced into this sample. It is therefore not appropriate to draw conclusions about the catalyst content from the residual mass in this curve.

The net mass loss after the purification was in excess of 90% and did not provide satisfactory results. However, significant insight was gained into this particular batch, suggesting modifications to the procedure. First, the initial wet peroxide burn should be done at 250°C and not 275°C done here. The burn can possibly proceed for longer than the 3.5 hours used, perhaps up to 6 hours. The mass loss after the second reflux (44%) was less than the mass loss after the first reflux (70%). Additional reflux cycles would likely continue the trend, with less material being lost in each cycle, and would likely be advantageous for obtaining higher purity. Finally, the annealing process seems to be effective without changes.

Full characterization of the purification process includes Raman spectroscopy and x-ray analysis to estimate the amount of carbonaceous impurities. By using the procedure outlined above, other HiPco batches were purified to $>$ 95 wt% SWNTs, $<$ 5 wt% carbon-derivative, and $\leq$ 0.7 wt% magnetic catalyst [21, 73].

Chapter 4

Percolation and effective medium theories

In this chapter, two theories are presented that describe the properties of inhomogeneous media such as composites. The two models, percolation and effective medium approximations, are based on different premises and are usually applicable in different regimes. While much effort has been made to unify them [31, 85, 126], they remain largely incompatible with each other. In the context of the present thesis, percolation theory is useful for providing a description of the electrical conductivity of SWNT/epoxy composites, because the electrical conductivities of the SWNTs and epoxy are very dissimilar; a sharp transition from insulator to conductor is observed with increasing SWNT concentration. By contrast, effective medium theory is useful for modeling the thermal conductivity of our SWNT/epoxy composites. Here, a sharp transition from insulator to conductor is not observed. The thermal conductivity of SWNTs is comparable to that of epoxy and the composite thermal conductivity is further limited by the presence of an interfacial thermal resistance at the SWNT/epoxy interface. In contrast to percolation theory, effective medium theory can describe

the continuous variation of thermal conductivity and enables us to include interfacial resistance in the description.

4.1 Percolation

Percolation theory describes how particles or other objects such as rods form clusters and networks. It is a study of the connections between such particles and how this connectedness affects the properties of the whole system at length scales much larger than the particle size. In this thesis, we are interested in the properties of carbon nanotube networks at macroscopic length scales, and percolation theory is one of the best tools available to describe these systems. The sections below describe percolation theory. First, the basic results of percolation theory for model systems are presented. In these systems, the percolation threshold and other quantities of interest can be calculated explicitly, laying the foundation for the less ideal problem of carbon nanotube percolation. Second, percolation models for a three-dimensional system of randomly-oriented rods is discussed. The percolation of non-interacting hard rods in three dimensions is relatively well understood [11, 12, 24], but since carbon nanotubes are strongly interacting, this model does not necessarily describe carbon nanotube networks accurately. To account for the interactions, we present a simple model for the percolation of carbon nanotubes. Our model predicts a range of concentrations at which the threshold should be observed, and is consistent with our experimental observations.

As an illustration of the general concept, consider a large empty box, as in Fig. 4.1. Particles are randomly placed in this box, one at a time. Initially, each particle is isolated, but as the density of particles increases, clusters begin to form. For simplicity, we assume that the particles can overlap without displacing other particles, and a cluster is two or more particles that overlap with

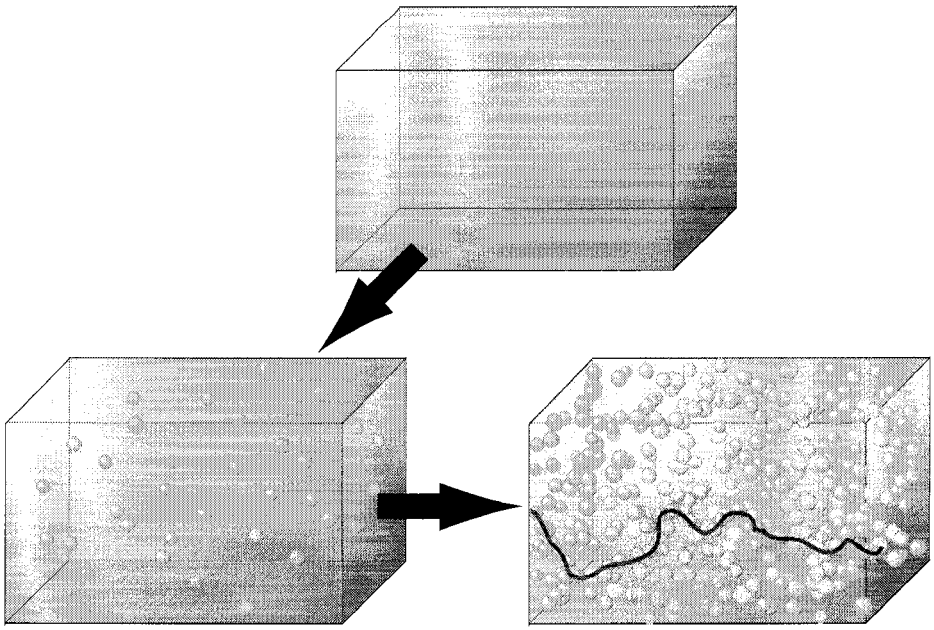

Figure 4.1: Percolation of particles placed randomly in a (zero-gravity) box. As the particle density increases, clusters of particles begin to form. Above a certain particle concentration p_c, a continuous path of particles forms through the matrix. If the particles are electrical conductors, a current will flow from one end of the box to the other above p_c. Below this threshold concentration, the material is insulating.

each other. The average cluster size is small at first, but grows rapidly as more particles are added and individual clusters combine to form larger ones. When a certain particle density is reached, a continuous cluster, also called a "spanning" or "infinite" cluster, will form. The particle density at this point is called the percolation threshold, p_c. If the particles are conductors, a current will be able to pass from one end of the box to the other for densities above p_c [85]. Continuing to add more particles reinforces the infinite cluster, providing more pathways for current to pass and increasing its conductivity. Percolation theory aims to describe these systems quantitatively in terms of the particle density. Quantities of interest include the distribution of cluster sizes, the threshold fraction, p_c, the size of the infinite cluster, and the conductivity of the system above threshold.

Unfortunately, exact solutions for the above random-particle system do not exist. Percolation

theory offers analytical solutions for a limited number of model systems, wherein "particles" are placed at well-defined locations on a lattice. Such lattices include the one-dimensional lattice, a few two-dimensional lattices and the theoretical construct called the Bethe Lattice or the Cayley Tree (see Fig. 4.2 and table 4.1). Three-dimensional lattices and systems that lack a regular periodicity cannot be solved analytically. In such cases, computer simulations and some theoretical assumptions are used to approximate the quantities of interest.

4.1.1 Lattice percolation

In this section, the basic concepts of percolation theory are presented for some one- and two-dimensional model systems. The study of these systems, although somewhat removed from the percolation of carbon nanotubes, lays a foundation that will facilitate the discussion of carbon nanotube percolation in the following section.

Consider a very large empty lattice. Some relevant types of lattices are presented in Fig. 4.2. The sites in the lattice can be randomly filled by "particles", in a manner similar to the example of the previous section. This is an instance of *site percolation*. Alternately, the sites can be thought of as intersections of the bonds between adjacent sites. *Bond percolation* describes the situation where the bonds between each site are connected randomly. The distinction affects the mathematical treatment of the two situations. Whereas each bond connects only two adjacent sites, a site can connect to more than two other sites, depending on the number of nearest neighbors in the lattice. In general, site and bond percolation yield different results. The number of nearest neighbors is known as the *coordination number*, Z. For example, a square lattice has four nearest neighbors, or $Z = 4$ (Fig 4.2(d)), whereas a honeycomb lattice has three nearest neighbors, or $Z = 3$ (Fig 4.2(c)). Site and bond percolation are identical only in certain situations, including the one-dimensional

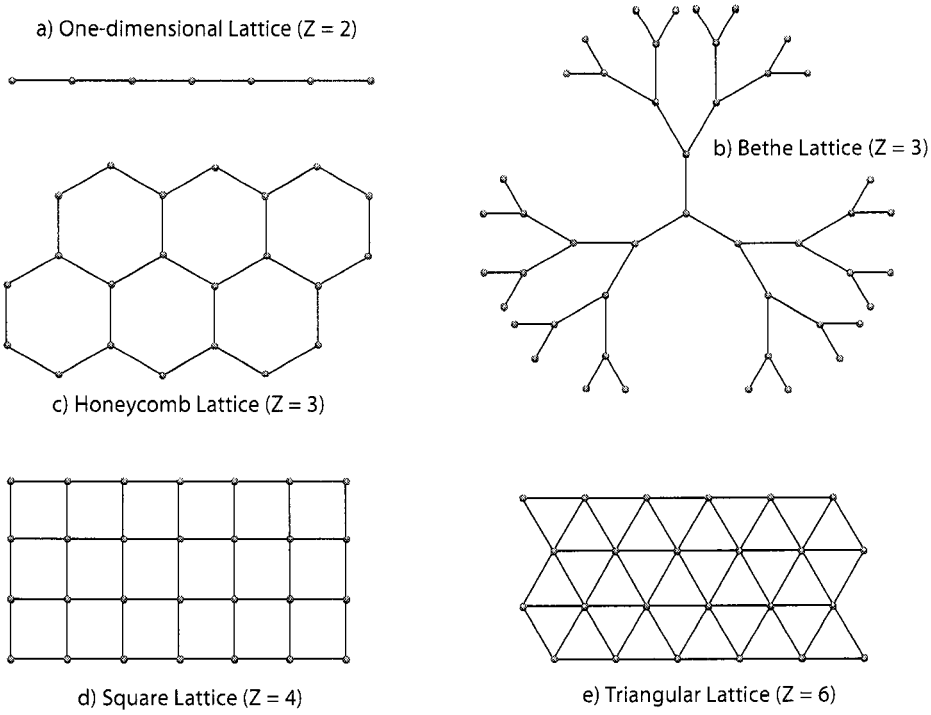

Figure 4.2: Some lattices for which exact solutions of percolation theory exist. Z denotes the coordination number of each lattice.

(Fig 4.2(a)) and the Bethe (Fig 4.2(b)) lattices, which are useful starting points in a discussion of percolation.

In one-dimensional percolation, a series of sites on a line is considered, as in Fig. 4.2(a). The probability of any site being filled is p, with $0 \leq p \leq 1$. Since the sites are occupied randomly, the probability of any two adjacent sites being occupied is p^2, for three adjacent sites it is p^3, and so on. The probability of a site having one empty neighbor is $(1-p)$. It follows that the total probability for a given site to be at a certain position in a five-particle cluster, noting that the cluster has an empty site at either end, is $p^5(1-p)^2$. For a cluster of arbitrary size, the cluster number n_s is defined such that $n_s = p^s(1-p)^2$. The cluster number defines the probability for any given site to be in a particular position in a cluster of s particles. The probability for a site to simply be in a cluster of size s, irrespective of position, is s times greater, or $n_s s = sp^s(1-p)^2$. The average

cluster size $S(p)$ is [142]

$$S(p) = \sum_s \frac{n_s s^2}{\sum_s n_s s}. \tag{4.1}$$

The definition stems from the following reasoning. The probability that a site belongs to a cluster of size s is $n_s s$, as before. The probability that it belongs to any finite cluster is $\sum n_s s$. Therefore, $w_s = n_s s / \sum n_s s$ is the probability that the cluster to which an arbitrary occupied site belongs contains exactly s sites. The average cluster size is then $S(p) = \sum w_s s$. This result is valid for systems of higher dimensionality also, for $p < p_c$. In one dimension, summing the geometric series for $p < 1$ results in [142]

$$S(p) = \frac{(1+p)}{(1-p)}. \tag{4.2}$$

The percolation threshold in the one dimensional lattice is $p_c = 1$, the situation where all the sites are occupied. Removing just one site creates two semi-infinite clusters, and theoretical current will no longer flow from one end of the lattice to the other. As a result, the one dimensional system can only be described below the percolation threshold.

Lattice	Z	p_{cb}	p_{cs}
1-D	2	1	1
Bethe	3	1/2	1/2
2-D Square	4	1/2	0.5927 (a)
2-D Honeycomb	3	$1 - 2sin(\pi/18) \simeq 0.6527$	0.6962 (a)
Triangular	6	$2sin(\pi/18) \simeq 0.3473$	1/2

Table 4.1: Table of percolation thresholds for bond (p_{cb}) and site (p_{cs}) percolation for some lattices where the exact thresholds can be found. Z is the coordination number for each lattice. In site percolation, values followed by (a) are approximate, based on computer simulations. No exact solutions have been found for these lattices [126].

The next simplest lattice, from a percolation theory point of view, is the somewhat unphysical Bethe lattice, also known as the Cayley tree, seen in Fig. 4.2(b). The lattice is constructed by starting at a central point or origin that has Z bonds, where Z is the coordination number. Each of the bonds ends in a site that splits into $(Z-1)$ bonds, such that the total coordination number at the new site is again Z. This splitting process continues for each branch out to infinity. Each level of branching is sometimes called a generation. The number of sites in a Cayley tree increases exponentially with the distance from the origin. For $Z = 3$, the first generation contains 3 sites, the second has 6 sites, the third has 12, the fourth has 24 sites, and so on. For this reason, the lattice is sometimes described as an infinite-dimensional system. In particular, for a large number of generations, the surface area (i.e., the number of sites on the surface) scales with the volume (i.e., the number of sites in the interior). The dimensionality of an object is frequently defined by comparing the surface area of the object to its volume by the relation $surface \propto volume^{(1-1/d)}$, where d is the dimensionality. For the Bethe lattice, the proportionality holds if $d \to \infty$.

In spite of its infinite dimensionality, the Bethe lattice is the simplest lattice for percolation theory because it contains no loops. In other words, by starting at any given point and moving randomly through the lattice, the same site is never encountered without direct backtracking. To determine the percolation threshold, we start at the origin and move outward along occupied sites. At each branch away from the origin, there are $(Z-1)$ sites in the next generation. The probability of any site being filled is p as before. Thus, on average, at each generation there are $p(Z-1)$ occupied sites. As in the one-dimensional case, the probability that successive sites along a path are occupied is the product of the individual probabilities. Here, the probability of finding a path of length n is $(p(Z-1))^n$. If $p(Z-1) < 1$, the probability of finding a continuous path approaches zero as the path length approaches infinity. Thus, for a continuous path to exist, $p > \frac{1}{Z-1}$, and the

percolation threshold in a Bethe Lattice is

$$p_c = \frac{1}{Z-1}. \tag{4.3}$$

For $Z = 3$, $p_c = 1/2$. Note that the origin itself may not be occupied, or otherwise may not be a part of the infinite cluster. This does not nullify the above result. Although it is convenient to define an origin, the Cayley Tree is an infinite lattice and the coordination number is the same at all sites. The origin is therefore not a "special" point, and an infinite cluster can still exist in the higher-order branches of the tree.

Unlike the one-dimensional case, we can consider here what happens above the percolation threshold. One quantity of interest is the percolation probability, $P(p)$. This is the probability that an arbitrary site belongs to the infinite cluster, and can be thought of as a description of the "strength" of the infinite cluster in relation to the density of filled sites, p. To calculate $P(p)$, consider an arbitrary site and one of its neighbors in a Bethe lattice with $Z = 3$. The site is connected to the neighbor by one bond, and the neighbor has two other sub-branches not connected to the original site. Q is defined to stand for the probability that a site is not connected to the infinite cluster through one branch originating from it, and is a function of p. The probability that the two branches of the neighbor are not connected to infinity is Q^2. The probability that the neighbor site is occupied but not connected to infinity through either of its sub-branches is pQ^2. Further, the probability that the neighbor is not occupied is $(1-p)$ as usual. Thus, the total probability that the original site is not connected to the infinite cluster through one of its neighbors is $Q = (1-p)+pQ^2$. Solving for Q yields two results, $Q = 1$ and $Q = (1-p)/p$. The first result apparently describes the infinite cluster below the threshold and is not applicable. Continuing, the probability that the site is occupied but not connected to the infinite cluster through any of its three

branches is pQ^3, which is also equal to $(p - P(p))$, so $P(p) = p(1 \quad Q^3) = p(1 \quad (\frac{1-p}{p})^3)$ or

$$\frac{P(p)}{p} = 1 - [\frac{1-p}{p}]^3. \tag{4.4}$$

At the percolation threshold, where $p = p_c = 1/2$, $P(p) = 0$, as expected. The Bethe lattice is one of very few systems where quantities such as $P(p)$ can be found explicitly for all values of p. For most systems, it is usually only possible to determine the power-law behavior of $P(p)$ and other percolation quantities near the percolation threshold in the form $P(p) \propto (p - p_c)^{\beta_p}$, where β_p is called the critical exponent for $P(p)$. This power-law dependence of percolation quantities near the threshold is central to percolation theory.

Unlike the percolation threshold, p_c, critical exponents are universal, meaning they depend only on the dimensionality of the system, and not on the particular lattice, coordination number, or microstructure. For the Bethe lattice just above the percolation threshold, a Taylor expansion of $P(p)$ in powers of $(p - p_c) = (p - 1/2)$ yields a non-zero first-order term, such that

$$P(p) \propto (p - p_c). \tag{4.5}$$

Therefore, $\beta_p = 1$. Table 4.2 summarizes some relevant percolation quantities and the critical exponents for two- and three-dimensional systems and the Bethe lattice [126].

Of particular importance to this thesis is the effective conductivity, $g_e(p)$. At first glance it may seem that the effective conductivity is similar to the percolation probability, or the "strength" of the infinite cluster as defined above, and the two should at least have the same exponent. However, this is not the case. The reason for this is that the infinite cluster contains many "dangling bonds", or dead-ends through which no current is carried. A site that is part of the infinite cluster might not

carry any current and might not contribute to the effective conductivity. Instead, the conductivity depends on the strength of the backbone, the sites that actually carry the current. In fact, most sites in an infinite cluster do not belong to the backbone, and the critical exponent for conductivity is therefore different [126]. For conductivity in three-dimensions, which includes the carbon nanotube composites described in this thesis, a percolation approach predicts a critical exponent of 2.0. Like other critical exponents, this value is independent of the microscopic details of the system and applies to all three-dimensional percolating networks. Note that this is an approximate value derived from computer simulations [109].

Experimental studies of carbon nanotube composites have frequently cited values [84, 113, 120, 131] between 1.3 and 2, while exponents of 3.1 were observed in disordered short carbon fiber composites [151].

In contrast to the exponents, the threshold value depends strongly on the microstructure. The next sections describe some theoretical efforts to determine the percolation thresholds of systems of rods which ultimately give insight to the thresholds seen in our nanotube composites.

4.1.2 Percolation of rods

Carbon nanotubes in suspension may be modelled as "sticky" hard rods. Geometrical percolation of non-interacting hard-rod systems is relatively well understood [11, 12] and predicts the percolation threshold to be inversely proportional to the rod aspect ratio, i.e., the threshold occurs at a

Percolation quantity	description	exponent	d=2	d=3	Bethe Lattice
$P(p)$	Percolation probability	β_p	5/26	0.41	1
$S_p(p)$	Average cluster size	$-\gamma_p$	-43/18	-1.82	-1
$g_e(p)$	Effective electrical conductivity	μ	1.3	2.0	3

Table 4.2: Table of some percolation critical exponents in two- and three-dimensions and the Bethe Lattice (d=∞). Exponents given as fractions are exact results. [126]

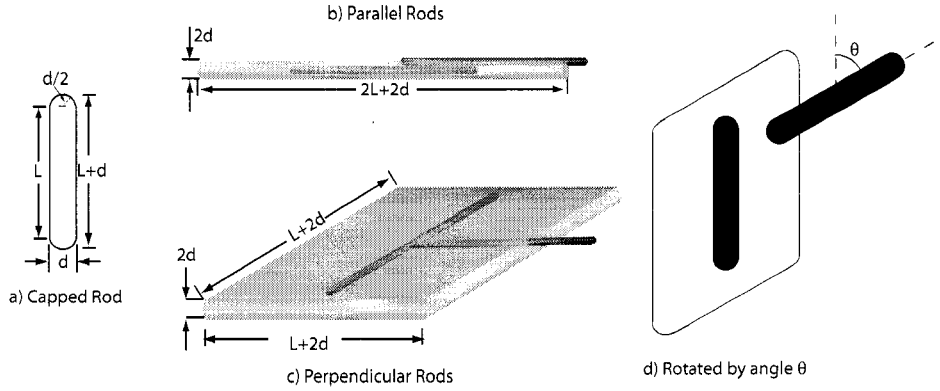

Figure 4.3: a) A rod of length L and diameter d capped by a hemisphere at each end. b) and c) The excluded volume for two identical rods depends on the relative orientation of the rods. For parallel, cylindrical rods (b), the excluded volume is a cylinder with volume $V_{excl\parallel} = (4\pi/3)d^3 + 2\pi(d)^2(L)$, while for perpendicular rods (c), $V_{excl\perp} = (4\pi/3)d^3 + 2\pi d^2 L + 2dL^2$. (d) When one of the rods is oriented at an angle θ, the excluded volume is $V_{excl}(\theta) = (4\pi/3)(d)^3 + 2\pi d^2 L + 2dL^2 \sin(\theta)$.

volume fraction $\phi_c \propto d/L$, where L is the rod length and d is the rod diameter. Experiments on carbon nanotube systems, including our data, frequently find significantly lower thresholds [21]. This is attributed to the interactions between nanotubes which are not taken into account in the above model. For attractively interacting hard-rods, the lower-bound to the percolation threshold is expected to be inversely proportional to the *square* of the aspect ratio, i.e., $\phi_c \propto d^2/L^2$, while the upper-bound is determined by the model for non-interacting rods described above. Our data are consistent with this interpretation; all thresholds are found between the lower- and upper-bounds. This section describes the models in more detail.

The percolation threshold of non-interacting, interpenetrable rods in three dimensions has been studied by computer simulations [11,12] and was found to be inversely proportional to the excluded volume of the rod, $p_c \propto 1/V_{excl}$. This conjecture was soon after confirmed to be valid analytically [24].

The excluded volume of an object is the volume defined around its center that cannot be occupied by the center point of an identical object. This volume arises entirely from geometrical constraints. For example, the centers of two identical spheres cannot be closer together than their diameter, d. The excluded volume of a sphere is therefore a sphere with radius d, or $V_{excl} = (4/3)\pi d^3$, which is eight times the physical volume of the sphere. In the case of two rods, the relative orientation of the two rods is also important. Consider a cylindrical rod of length L and diameter d capped at each end by a hemisphere, as in Fig. 4.3(a). When two such rods are parallel, the centers of the rods cannot be closer together than their diameter when the rods rods are next to one another, and not closer than the rod length if they are brought together tip-to-tip. Because of the hemispherical caps, the excluded volume is also a cylinder terminated by spherical caps at each end. The diameter of this cylinder is $2d$, and the length is $2L$, excluding the hemispherical caps, as seen in Fig. 4.3(b). Thus, for parallel rods, the excluded volume is

$$V_{excl||} = (4\pi/3)d^3 + 2\pi d^2 L. \tag{4.6}$$

Here, the first term comes from the two caps, and the second term comes from the cylinder.

For perpendicular rods (Fig. 4.3(c)),

$$V_{excl\perp} = (4\pi/3)d^3 + 2\pi d^2 L + 2dL^2. \tag{4.7}$$

Here, each of the four corners of the excluded volume is a quarter-sphere of radius d, which together add up to a full sphere (first term). The four narrow edges are half-cylinders of length L and radius d. Together they add up to the second term. The third term is the remaining rectangular area with sides L and thickness $2d$. These results have been generalized for two rods oriented at

an angle θ to each other (Fig. 4.3(d)). In this case, the excluded volume is

$$V_{excl}(\theta) = (4\pi/3)d^3 + 2\pi d^2 L + 2dL^2 \sin(\theta). \tag{4.8}$$

In a system of many rods, the average excluded volume per rod is calculated by averaging over all possible solid angles θ in three dimensions, i.e., it is the average of $|\vec{\mathbf{u}}_i \times \vec{\mathbf{u}}_j|$, where $\vec{\mathbf{u}}_i$ and $\vec{\mathbf{u}}_j$ are unit vectors along the axes of the corresponding sticks. [11].

$$\langle V_{excl}(\theta) \rangle = (4\pi/3)d^3 + 2\pi d^2 L + 2dL^2 \langle \sin(\theta) \rangle. \tag{4.9}$$

If the rods are isotropic, i.e., randomly oriented, the averaging is found to yield $\langle \sin(\theta) \rangle = \pi/4$ [11]. Furthermore, for very long and thin rods, $L \gg d$, such as nanotubes, the first two terms become negligible. The equation then reduces to

$$\langle V_{excl} \rangle = (\pi/2)dL^2. \tag{4.10}$$

The critical volume fraction is found by comparing the excluded volume per rod calculated above to the physical volume of the rod. The physical volume of each rod is

$$V_{rod} = \pi(d/2)^2 L + (4\pi/3)(d/2)^3 \simeq \frac{\pi}{4} d^2 L \tag{4.11}$$

and the critical volume fraction, which we will call ϕ_1, at which the percolation threshold is predicted can be found by dividing the volume of the rod by the average excluded volume per rod

$$\phi_1 = \frac{V_{rod}}{\langle V_{excl} \rangle} = \frac{(\pi/4)d^2 L}{(\pi/2)dL^2} = \frac{d}{2L}. \tag{4.12}$$

Note that the critical volume fraction scales as the inverse of the aspect ratio L/d of the rod. Therefore, the longer and narrower the rods, the lower the critical volume fraction. Carbon nanotubes typically have aspect ratios $L/d \sim 100 - 1000$. The excluded volume picture presented here predicts a percolation threshold $\phi_1 \sim 10^{-2} - 10^{-3}$, which is about two orders of magnitude higher than we observe in our experiments with SWNT composites [21]. The reason for this discrepancy is that SWNTs are strongly interacting and "sticky", readily clustering together to form networks, as shown schematically in Fig. 4.4(a). The excluded volume approach presented above is only valid for non-interacting rods. It turns out that the excluded volume prediction constitutes an upper-bound to the threshold for a random system of rods, as will be discussed later in this section. In order to estimate the lower-bound, we consider the lowest possible concentration of homogeneously distributed rods at which a continuous network is possible.

As seen in Fig. 4.4(a), attractive rods at densities that are nominally below a critical threshold can reorient themselves to create a continuous network. Given this freedom to rotate and find their neighbors, we consider a sphere of radius $L/2$ and volume $\nu_0 = (4\pi/3)(L/2)^3$ that circumscribes each rod [26,27,116]. For homogeneously distributed rods, a continuous rod network is possible if at least one rod is present in each such volume. This formulation gives a lower-bound concentration necessary for a continuous network to form from randomly oriented rods. As before, a critical volume fraction, ϕ_0, can be obtained by dividing the physical volume of the rod by the volume of the sphere,

$$\phi_0 = \frac{V_{rod}}{\nu_0} = \frac{(\pi/4)d^2L}{(4\pi/3)(L/2)^3} = \frac{3}{2}\frac{d^2}{L^2}. \tag{4.13}$$

In this model, the critical volume fraction is proportional to the inverse of the aspect ratio *squared*, and predicts a significantly lower threshold for long and thin particles than the excluded

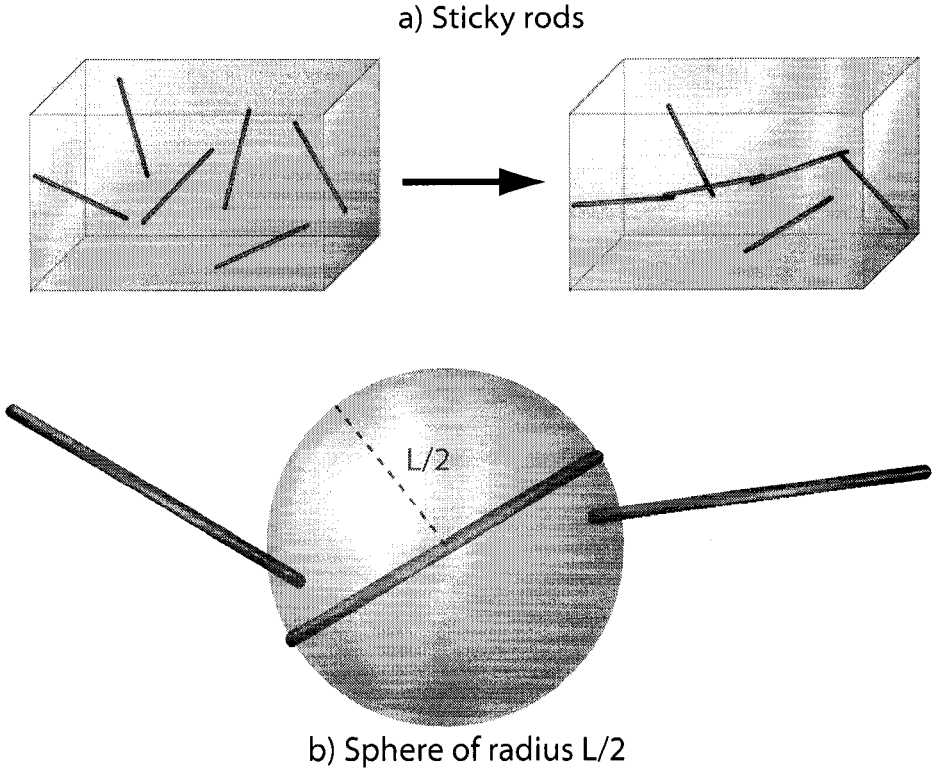

Figure 4.4: a) Schematic representation of how"Sticky" rods initially below a critical concentration (left) can cluster together to form a network (right). b) For homogeneously distributed attractive rods, a continuous network can form as long as there is at least one rod of length L per spherical volume $\nu = (4\pi/3)(L/2)^3$.

volume argument presented above. As before, for nanotubes with aspect ratios $L/d \sim 100 - 1000$, the predicted critical volume fraction is of order $\phi_0 \sim 10^{-4} - 10^{-6}$.

Interestingly, the same volume fractions arise in the study of liquid crystals. The Doi-Edwards theory [37] of liquid crystals describes concentration regimes of hard rods in suspension, as shown in Fig. 4.5. The transition from the dilute to semi-dilute regime occurs when the rotational motion of each rod is obstructed by the presence of other rods. This occurs at a volume fraction $\phi \approx \frac{d^2}{L^2}$. The transition from the semi-dilute to concentrated regime occurs at the isotropic packing limit, above which the rods align in anisotropic phases, such as the nematic phase, in order to accommodate the higher rod concentrations. The volume fraction at this transition is $\phi \approx \frac{d}{L}$. Using

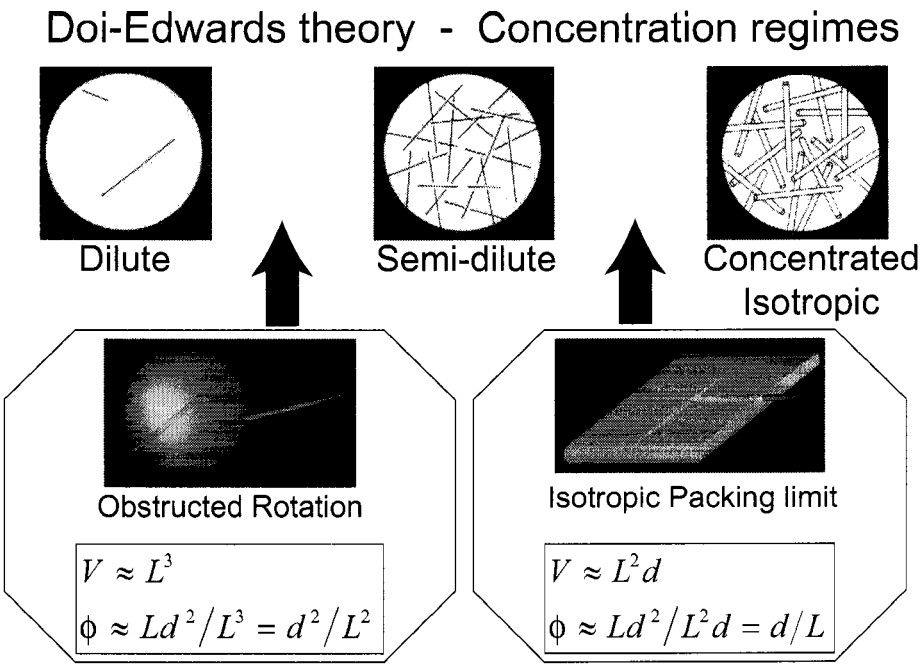

Figure 4.5: Concentration regimes for hard rods in solution, according to Doi-Edwards theory.

this terminology, the lower-bound for the percolation threshold of SWNTs occurs at the dilute to semi-dilute transition, while the upper-bound is at the semi-dilute to concentrated transition. The threshold might therefore be expected to lie in the semi-dilute regime, which is consistent with all of our data as will be seen in chapter 5 [21].

It is noteworthy that in rheological studies of surfactant-stabilized aqueous HiPco SWNT suspensions [65], a rigidity percolation threshold was observed at $\phi = .0026$, which agrees well with the excluded volume model. In this case, the surfactant greatly reduces the SWNT interactions, and the system more closely approximates the non-interacting rods scenario.

4.1.3 Summary - percolation of carbon nanotubes

Percolation theory, as presented above, predicts certain features about the conductivity of carbon nanotube composites. The predictions are summarized in Fig. 4.6. The composites are expected

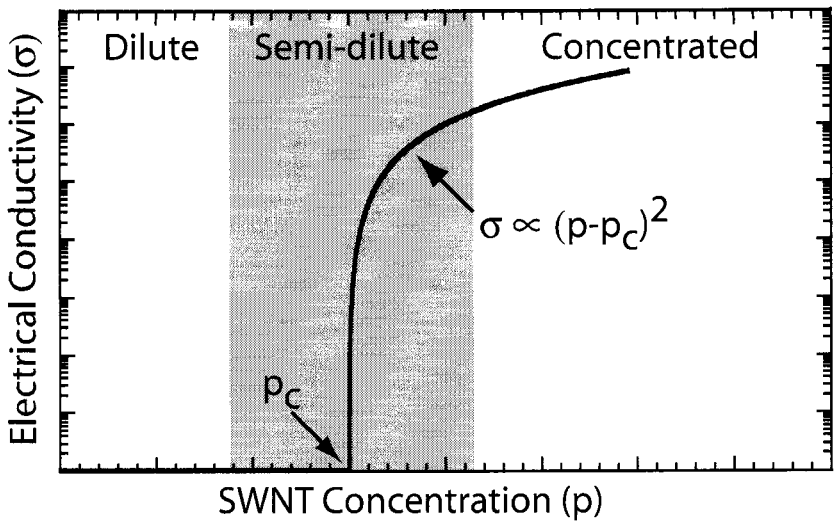

Figure 4.6: Predicted conductivity of CNT composites based on percolation theory, shown here on a semi-log plot.

to be insulating below a critical SWNT concentration - the percolation threshold, p_c. The location of the threshold is predicted to arise in the semi-dilute concentration regime, indicated by the gray shaded area in the figure. At SWNT concentrations above the threshold, conductivity should rise sharply according to a power law in the form $\sigma \propto (p - p_c)^2$, where σ is the conductivity and p is the SWNT concentration. These predictions are in good agreement with our experimental data presented in chapter 5.

4.2 Effective medium theory

4.2.1 Basic formulation

Effective medium theory approximates the bulk properties of inhomogeneous materials based on the properties of the constituents, as shown in Fig. 4.7(a). The original formulation developed by Maxwell (sometimes abbreviated MG-EMA for Maxwell-Garnett Effective Medium Approximation) concerns spherical particles of dielectric constant ϵ_1 in a matrix of dielectric constant ϵ_0, but

the results are applicable to a variety of steady-state problems in inhomogeneous media, including thermal conductivity. These equivalent problems are all governed by underlying Laplace/Poisson equations, and derivations of EMA for these systems exactly parallel the dielectric case presented herein. Some such problems are described in Table 4.3 [31]. Although in our work we are concerned with a thermal conductivity, it is useful to present the derivation in its original form using dielectric constants. This approach makes the derivation easier to follow, since the various concepts and quantities, such as scalar potential and electric field, are more easily recognizable from electrostatics. The goal is to determine an "effective" dielectric constant, ϵ, of the inhomogeneous system. The basis for the theory is the Claussius-Mossotti equation that relates the microscopic polarizability of an object to the macroscopic dielectric constant of an ensemble of such objects:

$$\frac{\epsilon - 1}{\epsilon + 2} = \frac{4\pi}{3} \sum N_j \alpha_j. \tag{4.14}$$

where N_j is the number of particles of species j, α_j is the microscopic polarizability of species j. If only one type of inclusion is considered equation 4.14 becomes

$$\frac{\epsilon - 1}{\epsilon + 2} = \frac{4\pi}{3} n\alpha, \tag{4.15}$$

Problem	Potential ϕ	$\mathbf{E} = -\nabla\phi$	ϵ	$\mathbf{D}$
Electrostatics	Electric Potential	Electric Field	Permittivity	Electric Displacement
Magnetostatics	Magnetic Potential	Magnetic Field	Permeability	Magnetic Induction
Electricity	Electric Potential	Electric Field	Electrical Conductivity	Current Density
Heat Conduction	Temperature	Temperature Gradient	Heat Conductivity	Heat Flux
Diffusion	Density	Density Gradient	Diffusion Constant	Particle Current Density

Table 4.3: Table of mathematically equivalent problems for which effective medium theory can be used directly. These steady-state systems are described by the Laplace equation that forms the basis of EMA.

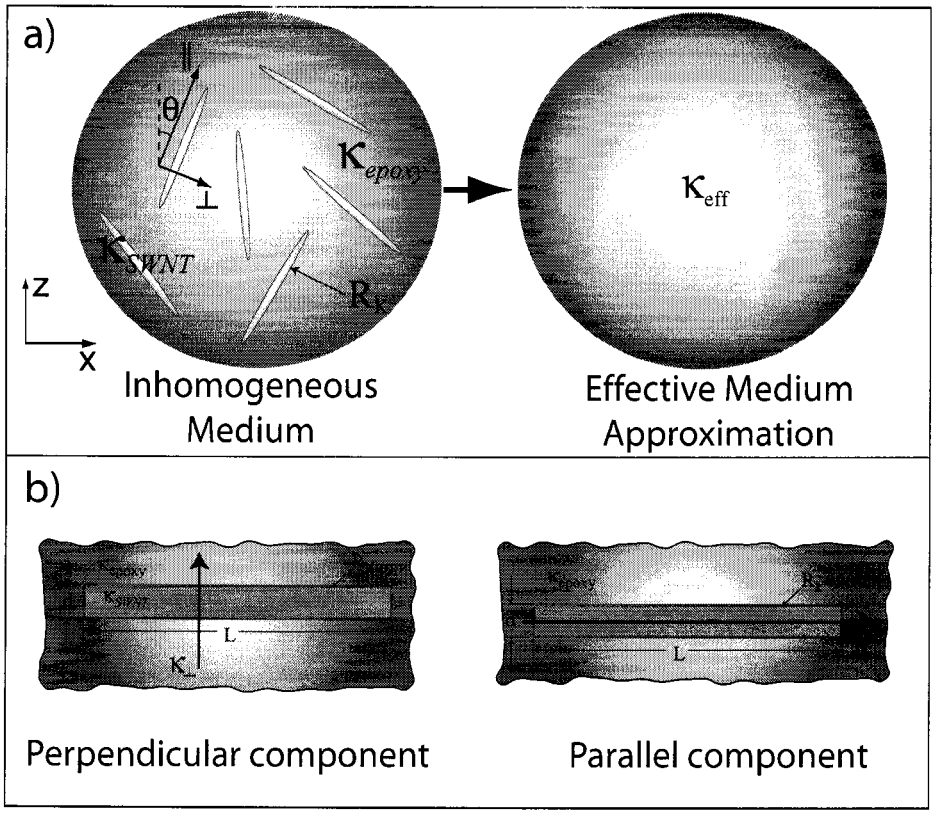

Figure 4.7: a) Schematic representation of the effective medium theory description of our SWNT-epoxy composites. The inhomogeneous composite (left) contains epoxy of thermal conductivity κ_{epoxy} and nanotubes, here approximated as ellipsoidal inclusions, with thermal conductivity κ_{SWNT} and thermal interface resistance (Kapitza resistance) R_K. Effective medium theory approximates this system as a homogeneous medium with effective thermal conductivity κ_{eff} (right). b) The thermal conductivity perpendicular and parallel to each nanotube is considered in the formulation.

where n is the number of particles with polarizability α. For a spherical particle of dielectric constant ϵ_1 and radius a, the polarizability is

$$\alpha = (\frac{\epsilon_1 - 1}{\epsilon_1 + 2})a^3, \tag{4.16}$$

and using $\phi = n\frac{4\pi}{3}a^3$ for the particle volume fraction, equation 4.15 becomes

$$\frac{\epsilon - 1}{\epsilon + 2} = \phi\frac{\epsilon_1 - 1}{\epsilon_1 + 2}. \tag{4.17}$$

Taking the background dielectric constant to be ϵ_0 equation 4.17 can be re-written as [31]

$$\frac{\epsilon - \epsilon_0}{\epsilon + 2\epsilon_0} = \phi \frac{\epsilon_1 - \epsilon_0}{\epsilon_1 + 2\epsilon_0}. \tag{4.18}$$

Solving for the effective dielectric constant ϵ yields

$$\epsilon = \epsilon_0 + \frac{3\phi\gamma_1}{1 - \phi\gamma_1}\epsilon_0, \tag{4.19}$$

where

$$\gamma_1 = \frac{\epsilon_1 - \epsilon_0}{\epsilon_1 + 2\epsilon_0}. \tag{4.20}$$

This is the original MG-EMA formulation. It describes the effective dielectric constant of an inhomogeneous system in terms of the individual dielectric constants of the constituents and the effective volume fraction. It should be noted that the above formulation has some significant limitations. For one, it does not predict any threshold concentration like percolation theory does, frequently producing incorrect results at high particle densities. While there have been many attempts to reconcile EMA with percolation [31, 85, 126], the two theories remain incompatible in many situations. Furthermore, the above formulation gives unreasonable results for systems with more than two distinct phases. Finally, the result is asymmetric, meaning that a different effective dielectric constant is obtained when the two phases are switched, i.e., when the "inclusions" are considered to be the "background" and vice versa. These limitations suggest that the formulation is not universally valid. The reason for the strange behavior is the Clausiuss-Mossotti relation itself, which depends on the concept of the Lorentz local field, $\mathbf{E}_{loc} = \mathbf{E}_0 + (4\pi/3)\mathbf{P}$, where $\mathbf{E}_{loc}$ is the local electric field inside a material, $\mathbf{E}_0$ is an external field, and $\mathbf{P}$ is the polarization of the

material. The derivation of the local field concept requires some assumptions that ultimately lead to incorrect results in the context of effective medium theory. Among these is the assumption that the local electric field is not strongly modified by the presence of a particle, which is not valid for highly dissimilar materials [31].

A more rigorous treatment based on the variational principle [31, 57] that does not use the Lorentz field concept reveals that equation 4.19 is valid in certain regimes, including systems of dilute spherical inclusions. In addition, it reveals that the effective dielectric constant for all isotropic systems will fall between the so-called Hashin-Shtrikman bounds

$$\epsilon_1 + \frac{\epsilon_1 \phi_2}{\frac{\epsilon_1}{\epsilon_2 - \epsilon_1} + \frac{\phi_1}{3}} < \epsilon_{eff} < \epsilon_2 + \frac{\epsilon_2 \phi_1}{\frac{\epsilon_2}{\epsilon_1 - \epsilon_2} + \frac{\phi_2}{3}}, \tag{4.21}$$

where ϵ_1 and ϵ_2 are the dielectric constants of the constituents and ϵ_{eff} is the effective dielectric constant of the material.

4.2.2 Ellipsoidal particles with interfacial thermal resistance

For carbon nanotube composites, we are interested in a formulation of effective medium theory valid for inclusions of long and thin rodlike particles of thermal conductivity κ_p embedded in an epoxy matrix of thermal conductivity κ_m. In addition, the formulation requires that the interfacial thermal resistance (or Kapitza resistance) between the carbon nanotubes and the epoxy be considered. Kapitza resistance, denoted R_K, is a temperature discontinuity across the interface between two dissimilar materials. The discontinuity is a result of imperfect thermal coupling between the materials, for reasons such as poor mechanical contact or thermal expansion coefficient mismatch, and will be discussed further in chapter 6.

The complex particle shapes require an approach based on Green's functions, a mathematical tool for solving boundary value problems with non-trivial geometries. Such an approach was used [106] to obtain an expression for the effective conductivity of composite materials with ellipsoidal inclusions and a thermal interfacial resistance. The ellipsoids (more precisely spheroids, i.e., ellipsoids of circular cross section perpendicular to the long axis) have aspect ratio $p = a_{\|}/a_{\perp}$, where $a_{\|}$ is the major axis of the spheroid and $a_{\perp}$ is the minor axis. Ellipsoids approximate carbon nanotubes in our system in the limit $p \to \infty$. The geometry of the problem is presented in Fig. 4.7(a). The effective thermal conductivity of the inhomogeneous medium is found to be [106]

$$\kappa_x = \kappa_m \frac{2 + \phi[(\beta_{\perp} 1 - L_{\perp})(1 + \langle\cos^2(\theta)\rangle) + \beta_{\|}(1 - L_{\|})(1 - \langle\cos^2(\theta)\rangle)]}{2 - \phi[\beta_{\perp} L_{\perp}(1 + \langle\cos^2(\theta)\rangle) + \beta_{\|} L_{\|}(1 - \langle\cos^2(\theta)\rangle)]}, \tag{4.22}$$

$$\kappa_z = \kappa_m \frac{1 + \phi[\beta_{\perp}(1 - L_{\perp})(1 - \langle\cos^2(\theta)\rangle) + \beta_{\|}(1 - L_{\|})\langle\cos^2(\theta)\rangle]}{1 - \phi[\beta_{\perp} L_{\perp}(1 - \langle\cos^2(\theta)\rangle) + \beta_{\|} L_{\|}\langle\cos^2(\theta)\rangle]}, \tag{4.23}$$

where subscripts x and z denote the principal axes in the coordinate system of the composite, while the subscripts $\perp$ and $\|$ are in the coordinate system of an individual spheroidal inclusion (see Fig. 4.7(a)). $\langle\cos^2(\theta)\rangle$ relates the two coordinate systems such that $\langle\cos^2(\theta)\rangle = 1$ for all the particles aligned along the z-axis, $\langle\cos^2(\theta)\rangle = 0$ for all particles aligned along the x-axis, and $\langle\cos^2(\theta)\rangle = 1/3$ for an isotropic distribution. In the above,

$$L_{\perp} = \frac{p^2}{2(p^2 - 1)} - \frac{p}{2(p^2 - 1)^{3/2}} \cosh^{-1}(p) \quad \text{for p} > 1, \tag{4.24}$$

and

$$L_{\|} = 1 - 2L_{\perp} \tag{4.25}$$

are geometrical factors that stem from the spheroidal particle shape.

$$\beta_i = \frac{\kappa_i^c - \kappa_m}{\kappa_m + L_i(\kappa_i^c - \kappa_m)} \tag{4.26}$$

are dimensionless factors that relate to the thermal conductivities of the matrix and the particles, including the interfacial resistance,

$$\kappa_i^c = \kappa_p/(1 + \gamma L_i \kappa_p/\kappa_m). \tag{4.27}$$

The exact physical significance of these factors will be discussed later in this section. Here, i is either the perpendicular $\perp$ or parallel $\parallel$ component with respect to the long axis of the spheroid and

$$\gamma = (2 + 1/p)\alpha, \tag{4.28}$$

where

$$\alpha = a_k/a_\perp. \tag{4.29}$$

a_k is called the Kapitza radius that is related to the Kapitza resistance by

$$a_k = R_K \kappa_m. \tag{4.30}$$

In this general formulation, the theory is valid for oriented and misoriented oblate ($p \geq 1$) spheroids. It is interesting to note that the theory of reference [106] reduces to equation 4.19 for the case of $p = 1$ and $R_K = 0$. Further, for long fibers aligned along the z axis of the composite,

the theory reduces to

$$\kappa_z = \phi\kappa_p + (1-\phi)\kappa_m, \tag{4.31}$$

where κ_p is the thermal conductivity of the particles. This is the simple space-filling model frequently presented in basic texts on the conductivity of composite materials [25]. Here, only the relative volume fractions of the constituents determine the effective conductivity, which varies linearly from the matrix value κ_m at $\phi = 0$ to the particle value κ_p at $\phi = 1$. For misoriented fibers in which the conductivity is isotropic, this model is sometimes augmented by a factor of 1/3 such that

$$\kappa_{eff} = (1/3)\phi\kappa_p + (1-\phi)\kappa_m, \tag{4.32}$$

but this is a very crude approximation and is only valid for small ϕ.

For SWNT composites, we concentrate on the case of long, misoriented fibers. With $\langle\cos^2(\theta)\rangle = 1/3$ for an isotropic orientation of the spheroids, the effective conductivity of the composite is also isotropic, and equations 4.22 and 4.23 become equal, $\kappa_x = \kappa_z = \kappa_{eff}$, such that

$$\kappa_{eff} = \kappa_m \frac{3 + \phi(2\beta_\perp(1-L_\perp) + \beta_\parallel(1-L_\parallel))}{3 - \phi(2\beta_\perp L_\perp + \beta_\parallel L_\parallel)}. \tag{4.33}$$

Furthermore, we can take the large aspect ratio limit, $p \to \infty$, and use the fact that the thermal conductivity of the nanotubes is much greater than that of the epoxy matrix so that

$$\lim_{p\to\infty} L_\perp \to 1/2 \tag{4.34}$$

and

$$\lim_{p\to\infty} L_{\|} = 1 - 2L_{\perp} = 0. \tag{4.35}$$

So

$$\lim_{p\to\infty} \kappa_{\perp}^{c} \to \frac{\kappa_p}{1 + \frac{a_k}{a_1}\frac{\kappa_p}{\kappa_m}} \tag{4.36}$$

and

$$\lim_{p\to\infty} K_{\|}^{c} \to \kappa_p \tag{4.37}$$

and

$$\kappa_{eff} = \kappa_m \frac{3 + \phi(\beta_{\perp} + \beta_{\|})}{3 - \phi\beta\perp} \tag{4.38}$$

where

$$\beta_{\perp} = \frac{2(\kappa_{\perp}^{c} - \kappa_m)}{\kappa_{\perp}^{c} + \kappa_m} \qquad \beta_{\|} = \frac{\kappa_{\|}^{c}}{\kappa_m} - 1 \tag{4.39}$$

The above derivation requires a correction. Equation 4.37 reveals an artifact of using ellipsoidal particles as the starting point in the large-p limit, i.e., the interfacial resistance at the narrow particle ends goes to zero, or $K_{\|}$ is simply the particle conductivity and is independent of R_K. A more appropriate expression for $K_{\|}$ would include the interfacial resistance at the ends. In fact, based on the schematic in Fig. 4.7(b), it should have the same form as $K_{\perp}$. Based on this argument, the perpendicular and parallel components for this system should be written as [105]

$$\kappa_{\perp} = \frac{\kappa_p}{1 + \frac{2a_k}{d}\frac{\kappa_p}{\kappa_m}} \qquad \kappa_{\|} = \frac{\kappa_p}{1 + \frac{2a_k}{L}\frac{\kappa_p}{\kappa_m}}, \tag{4.40}$$

where d and L are the rod diameter and length, respectively. A physical way to understand these

values (see Fig. 4.7(b)) is as a simple series addition of the interface/nanotube/interface conductivities, i.e.,

$$\frac{1}{\kappa_{\perp}^{c}} = \frac{2R_K}{d} + \frac{1}{\kappa_p} \qquad \frac{1}{\kappa_{\parallel}^{c}} = \frac{2R_K}{L} + \frac{1}{\kappa_p}. \tag{4.41}$$

Equation 4.38 used in conjunction with equations 4.39 and 4.40 is a useful formulation of EMA to describe the thermal conductivity of carbon nanotube composites. This formulation is applied in chapter 6 to estimate the value of the Kapitza resistance R_K in our SWNT/epoxy composites by using current estimates of SWNT thermal conductivity (see chapter 2 for κ_p and our measured values for the thermal conductivity of epoxy for κ_m. We find the Kapitza resistance to be a significant limiting factor in the enhancement of epoxy thermal conductivity by nanotubes, but we also find that it is variable, determined by the processing methods used.

Chapter 5

Electrical conductivity of SWNT/Epoxy composites

5.1 Background

Electrically conducting composites are typically made by embedding conductive particles in an otherwise insulating matrix. The resulting materials often exhibit percolation-like electrical conductivity [85] with a well-defined insulator-conductor transition as a function of filler concentration. Applications for these composites include static charge dissipation [138], RF shielding, and field emission sources [154, 157]. Table 5.1 summarizes the properties of some commercially available conductive epoxies. Recently, single wall carbon nanotubes (SWNTs) have emerged as an attractive option for conductive composite materials. Their small size, large aspect ratio, and high conductivity make it possible to create conductive composites at very low filling concentrations and with smaller inhomogeneities than can be achieved with larger particles. Lower filling fractions imply smaller perturbations of bulk physical properties such as strength or optical

transparency, as well as lower costs. We describe here a simple procedure for making conductive SWNT in epoxy composites that result in exceptionally low threshold concentrations with minimal modification of the epoxy matrix material.

Composites made with carbon nanotubes are heavily researched due to their vast application potential. While both single-wall carbon nanotubes (SWNTs) and multi-wall carbon nanotubes (MWNTs) are used for creating nanocomposites, SWNTs hold potential for better properties. They are significantly (10 - 100×) smaller than MWNTs, have higher aspect ratios, are stronger, and can be more conductive than MWNTs. Thus, SWNTs can be used to make more homogeneous nanocomposites with improved physical properties and conductivity compared to MWNT nanocomposites. Thus far, studies of SWNT/polymer composite electrical conductivity [5, 15, 16, 19, 41, 51, 54, 67, 84, 92, 98, 108, 111, 113, 120, 121, 129, 134, 140, 165] have reported low thresholds at volume fractions ranging from [134] $\sim 1 \times 10^{-4}$ to several percent [92], in some cases outperforming current technologies such as carbon-black based composites. Multiwall carbon nanotubes have also been widely studied in epoxy composites [14, 130, 131]. Many aspects of the problem, however, are poorly understood and full optimization remains elusive. The starting formulations of dispersed SWNTs frequently contain dense aggregates of nanotubes, as well as amorphous carbon and metallic impurities that can persist throughout processing and affect performance. Stabilizing the nanotubes in suspension can reduce aggregates, but introduces other problems. For example, covalent stabilization modifies the intrinsic SWNT conductivity, while steric stabilization can degrade contacts between nanotubes and generally introduces additional impurities into the composite. In addition, although well-dispersed SWNTs typically have a higher length-to-diameter ratio than aggregates, which is important for obtaining low thresholds [12], in some instances aggregation can be beneficial to creating percolating networks. Network formation

Epoxy brand name	Filler type	Electrical conductivity (S/cm)	Tensile strength (MPa)
Creative Materials 106-21	Carbon	10^{-2}	~60
MG Chemicals 8331	Silver	2.6	~6
EpoxySystems 672	ceramic	10^{-6} - 10^{-4}	~30

Table 5.1: A comparison of some commercially available conductive epoxies. The values quoted are provided by the manufacturer. The tensile strength of Epon 828 epoxy with EpiKure 3234 crosslinker is approximately 73 MPa.

through particle chaining, in particular, can be a key factor in lowering threshold concentrations. In carbon black composites, for example, the threshold can be lowered by inducing particle aggregation [133] and through the formation of diffuse, or 'fluffy' agglomerates [125]. Long, flexible ropes of aligned multi-wall nanotubes (MWNTs) have also been used to make composites with threshold volume fractions as low as $\sim 2 \times 10^{-5}$ albeit with millimeter-scale inhomogeneities [131]. In such cases, as in most real composites, the relationship between particle aspect ratio and threshold concentration becomes difficult to predict. In SWNT composites these effects remain largely unexplored.

Here we show how SWNT length-diameter aspect ratio and spontaneous formation of nanotube networks affect the conductivity of bulk SWNT-epoxy composites. We compare two types of SWNTs with different mean aspect ratios, and introduce two nanotube-epoxy processing methods that inhibit or promote the formation of networks. We observe conductivity thresholds at SWNT volume fractions as low as 5.2 $(+1.9/-0.5)\times 10^{-5}$, nearly 10 times lower than values quoted in previous reports on SWNT composites in epoxy matrices [84]. All conductivity thresholds fall within the semidilute concentration regime, but the effect of nanotube aspect ratio on the threshold concentration is only marginally explained by simple models for rod percolation.

The key to this work is a dilute, 0.004 wt%, metastable dispersion of pure SWNTs in N,N-Dimethylformamide (DMF) (see Fig 5.3(a)). SWNTs remain well dispersed in this suspension

either in isolation or in small SWNT bundles while under sonication (see Fig. 5.7(g)), but the SWNTs slowly re-aggregate when sonication is turned off. The absence of stabilizing agents and formulation metastability permit networks to form prior to curing; the low SWNT concentration reduces aggregation, and so enables us to benefit from the high aspect ratio of the isolated SWNTs. In addition to being an effective dispersing agent for SWNTs, DMF is miscible with Epon 828 resin, and the SWNT-DMF dispersion can be effectively mixed with the resin. The DMF is evaporated off as the the mixture is added, leaving only a mixture of SWNTs and resin, which is then cured. The samples were processed under a variety of sonication conditions, during which time the dilute SWNT/DMF solution was slowly added to the epoxy resin, and the DMF was allowed to evaporate. Continuous sonication produced more disaggregated composites, while stoppage of sonication prior to curing permitted networks to form. Taken together, the use of pristine SWNTs and sonication enabled us to produce fairly homogeneous composites with minimal perturbation of the high strength epoxy. Interestingly, composites in which nanotubes were allowed to reaggregate exhibited lower electrical conductivity thresholds compared to more homogenized composites.

5.2 Materials

5.2.1 Single Wall Carbon Nanotubes

The SWNTs studied were laser-oven (Tubes@Rice) and HiPco (Carbon Nanotechnologies, Inc.). Nanotubes were obtained in raw form and purified according to procedures largely described in references [124] and [52], and in chapter 3 of this thesis. The suspensions were magnetically fractionated, reducing the magnetic catalyst fraction to $\leq$ 0.7 wt%, and then the nanotubes were annealed at 1150°C as described in chapter 3. A combination of x-ray and thermogravimetric

analysis (TGA) measurements suggest that the resultant purified nanotubes contain > 95 wt% SWNTs and < 5 wt% carbon-derivative (amorphous carbon, graphite) impurities in addition to the above mentioned small quantities of catalyst particles. Details of the TGA and X-ray analyses are given in references [73] and [164], respectively. Atomic force microscopy (AFM) characterization showed that the laser-oven (HiPco) SWNTs had average length, $L = 516 \pm 286$ nm (167 ± 90 nm), and average diameter, $d = 1.35 \pm 0.15$ nm (1.1 ± 0.3 nm) [75]. These dimensions cover the typical range of SWNT sizes available today.

5.2.2 Epoxy

Epoxies are a class of epoxide-based polymers that can be cured (crosslinked) to create very strong materials which are widely used as structural components and adhesives. Various types of epoxy are available commercially, typically as two-component systems, consisting of a liquid resin and a crosslinker. Upon mixing, the crosslinker reacts (covalently bonds) with epoxide groups in the resin to create a densely crosslinked network. Epoxy is a thermoset plastic, meaning that it cures (irreversibly polymerizes and crosslinks) into a stronger form through the addition of energy, here an exothermic chemical reaction. In contrast to so-called thermoplastics, thermosets cannot be melted or significantly softened by heating and are typically much stronger.

The epoxy used in the present experiments is Shell Epon 828 (Miller Stephenson, density 1.16 g/cm^3) resin with EpiKure 3234 cross-linker (Miller Stephenson, density 0.98 g/cm^3). Epon 828 resin is a diglycidyl ether of bisphenol-A (DGEBA), also called a bisphenol-A/epichlorohydrin resin, and it is one of the most basic and most widely used types of epoxy. It is frequently synthesized by reacting bisphenol-A with epichlorohydrin, as shown in Fig. 5.1(a). The reaction results in one or more Bisphenol-A molecules arranged in a chain, with epoxide groups at each end, as

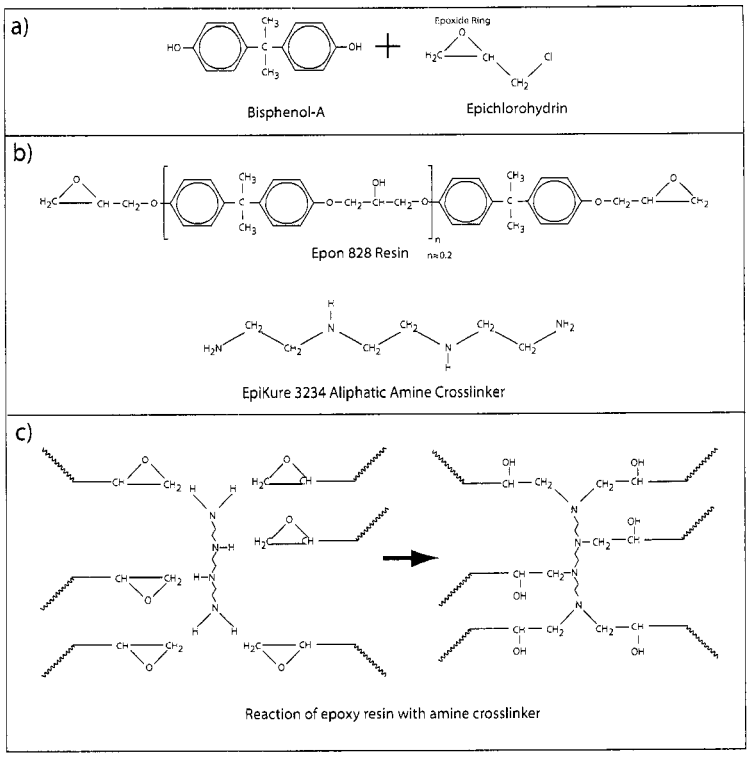

Figure 5.1: a) Epon 828 is frequently made by reacting Bisphenol-A with epichlorohydrin. b) The structure of Epon 828 resin consists of a short linear chain of bisphenol-a groups terminated by epoxide rings at either end. The aliphatic amine crosslinker used in our composites (EpiKure 3234) contains two primary and two secondary amine groups. Each primary amine can ideally react with two epoxide rings, while each secondary amine can react with one epoxide group. c) schematic of the reaction between Epikure 3234 amine crosslinker and epoxide rings. Each molecule of EpiKure 3234 can react with up to six epoxides, but usually the molecules become immobile before all groups are able to react (see text).

in Fig. 5.1(b). The average number of Bisphenol-A groups per molecule can be estimated by considering the epoxide equivalent weight, or the weight of the resin per epoxide group. For Epon 828, the epoxide equivalent weight is found experimentally to be 185-192 g/eq [58], meaning each 185-192 grams of resin contain one mole of epoxide groups. Since Epon 828 is a diepoxide (i.e., there are two epoxide groups per molecule), the average molecular weight of an Epon 828 molecule is ideally twice the equivalent weight, or 370-384. The average number of Bisphenol-A units in the chain is then found to be $\sim$1.2. This direct calculation is an estimate, since it does not

take into account impurities in the resin. Such impurities are included in the empirical equivalent weight measurements. The equivalent weight is therefore a more relevant quantity from a practical point of view, and is used to determine the stoichiometry between the resin and crosslinker. The crosslinker used in our experiments is EpiKure 3234 (Triethylenetetramine), which has two primary and two secondary amine groups, as shown in Fig. 5.1(b). A schematic of the reaction of the epoxides with the crosslinker is shown in Fig. 5.1(c). In principle, each crosslinker molecule can react with up to six epoxides, creating a very densely crosslinked network that is responsible for the high strength of the epoxy. In reality, however, the amount of crosslinking, especially for the secondary amines which are located on interior of the molecule, is limited by the mobility of the crosslinker which decreases as the number of crosslinks grows. Above a certain crosslink density, the molecules become immobile and the reaction cannot proceed. Therefore, some epoxide and amine groups typically remain unreacted. A calculation based on the epoxide equivalent weight and number of amine groups in the crosslinker determines that proper stoichiometry is obtained at a 13:100 EpiKure 3234 to Epon 828 weight ratio. This is the mixing ratio used in curing our composites.

5.3 Composite preparation

The purified nanotubes are dispersed in N,N-Dimethylformamide (DMF) using a low power, high frequency sonicator (Cole-Parmer model 08849-00, 1 pint, 17W) at concentrations of 0.004 wt% (40 μg SWNT per 1 g DMF) and 0.04 wt% (400 μg SWNT per 1 g DMF). To characterize the dispersion, we deposit SWNTs onto a hexamethyldisilazane (HMDS) treated silicon wafer by dipping the wafer into the SWNT suspensions and then measuring the height of the deposited nanotubes using atomic force microscopy. See chapter 3 for details on wafer preparation and AFM imaging.

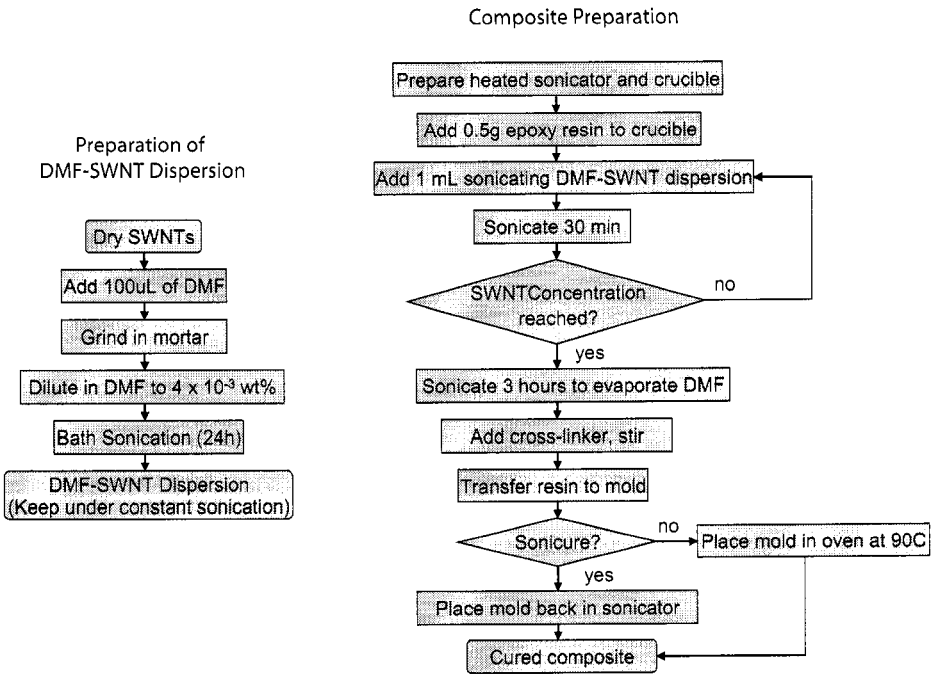

Figure 5.2: Flowcharts describing the preparation of a dilute SWNT-DMF dispersion and the process for making composites.

Fig.5.7(g) shows an AFM image of a wafer that was left in solution for 30 minutes; our quantitative dispersion data, however, are derived from similar images of wafers that are only briefly dipped into the solution, and therefore contain a much lower density of adsorbed SWNTs. The 0.004 wt% SWNT-DMF dispersion contains a mixture of isolated nanotubes ($< 10\%$) and small bundles ($> 90\%$, mean height < 6 nm), whereas the 0.04 wt% SWNT-DMF dispersion contains many significantly larger bundles. Flowcharts describing the preparation of the SWNT-DMF dispersion and the process for making composites are presented in Fig. 5.2

For each SWNT-composite sample, 0.5 g of epoxy resin was placed in a ceramic crucible in the bath sonicator described above, as shown in Fig 5.3(b). The sonicator temperature was maintained at 80°C. SWNT-DMF suspension is added into the heated and sonicating epoxy resin with a glass syringe in discrete 1 ml increments every 30 minutes, until the desired nanotube concentration

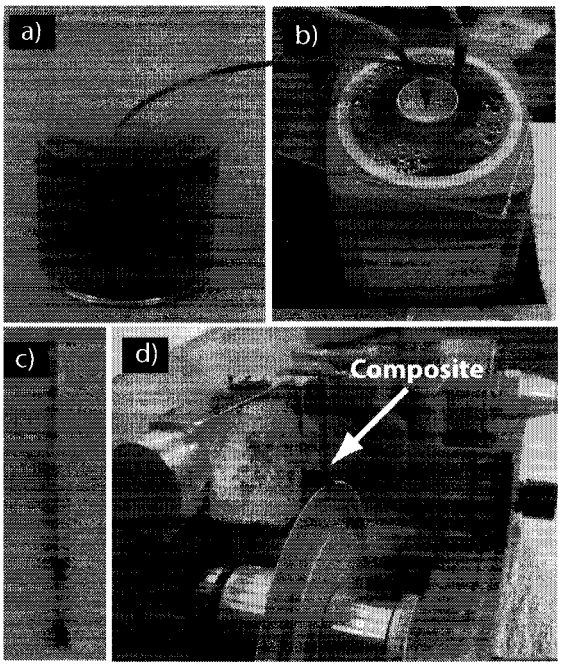

Figure 5.3: Process for making composites. a) A dilute dispersion of SWNTs in DMF. b) Sonicating epoxy resin. 0.5 g of epoxy resin in placed in the white crucible at the center of the picture. The sonicator bath is heated by circulating hot water through a coiled copper tube placed in the sonicator bath. A part of the heating coil is seen near the top of the picture. The sonicator bath is covered with a plexiglass cover to reduce evaporation of the bath water. A hole is cut in the middle of the cover to accommodate the crucible, such that the bottom of the crucible rests $\sim$1 cm below the surface of the bath water. The dilute suspension from (a) is slowly added to the sonicating resin in 1 mL additions each 30 minutes, until the desired concentration is reached. c) A 1 mL plastic syringe (inner diameter 4.7 mm) is used as a mold for the curing resin. The syringe tip is cut off, and both sides are sealed by a rubber syringe piston. In sonicured composites, the full syringe is placed back into the sonicator while the epoxy cures. d) The cured epoxy is cut into cylindrical pieces on a diamond saw.

is reached. The elevated sonication temperature reduced the viscosity of the epoxy resin; this step is necessary for effective sonication and fast DMF evaporation. We found that adding the SWNT-DMF solution slowly in small discrete steps, and allowing the DMF to evaporate between each step improved the sonication effectiveness. Sonication during processing tends to break up transient SWNT networks and inhibit the formation of new ones. The resultant sample is left in the sonicator for an additional 2-3 hours to ensure complete evaporation of DMF. We then add 65 μL

of cross-linker to the sonicating SWNT-epoxy resin mixture. We stir the mixture mechanically for two minutes, and then load it into a thin-walled cylindrical Teflon mold (1 mL plastic syringe, as shown in Fig. 5.3(c)). At this stage, the samples are divided into two categories. In the first set, samples are placed into a hot water bath to cure at 90°C for 30 min; curing proceeds without sonication. Hereafter, we refer to these samples as 'non-sonicured'. In the second set, samples are placed in the sonicator bath at 80°C, and are cured under sonication for 30 min. We refer to these samples as 'sonicured'. We found that 'sonicured' samples are more homogeneous than 'non-sonicured' samples, implying that SWNT networks which form during sample processing are successfully dispersed. All samples are subsequently annealed in an oven at 120°C for two hours. Thus prepared, the samples are cut with a diamond saw into 5.4 mm, 2.5 mm, and 300 μm thick pieces, as shown in Fig. 5.3(d), and the flat ends are polished on 5 μm grain polishing paper.

The density of cured epoxy was found to be 1.2 ± 0.02 g/cm^3. We use the cured epoxy density along with the calculated value of 1.4 g/cm^3 for nanotube density [113] to convert from units of weight percent to volume fraction. The volume fraction ϕ is obtained from the formula $\phi = \frac{1.2}{1.4} x \div 100 \approx 8.6 \times 10^{-3} x$, where x is the SWNT weight %.

5.4 Electrical conductivity measurement

5.4.1 Two-point and Four-point measurements

The simplest method for measuring the conductivity of a sample is with a two-point configuration, in which two electrodes are used for both applying a bias and taking the measurement. A voltage (or current) is applied across the sample, and the corresponding current (voltage drop) is measured with the same two leads, as shown in Fig. 5.4(a). The resistance R of the sample is calculated from

ohm's law, $R = V/I$, where V is the voltage drop across the sample and I is the current through the sample. The conductivity σ is calculated from the resistance and the sample dimensions $\sigma = (L/A)/R$, where L is the sample length and A is the cross-sectional area. Typically, multiple current/voltage combinations are used to obtain a current/voltage, or IV curve, as in Fig 5.5. For "ohmic" conductors, this curve is a straight line, but many materials deviate from this rule, and are called "non-ohmic". In our composite samples, the two-point conductivity in Fig. 5.5 is distinctly non-ohmic. It was found that this behavior does not stem from the composite samples themselves, but rather from the contact resistance between the silver-paint electrodes and the sample, which is eliminated by using a four-point measurement configuration as described below.

Since the two-point method uses the same leads for applying the bias and taking the measurement, the measured resistance includes the resistance of the leads and contacts, in addition to the resistance of the sample itself, as in Fig. 5.4(a). In cases where contact resistance is significant, such as our SWNT composites, a four-point method is frequently used. In this method, an outer set of electrodes is used to apply a known current, while a separate, inner set of electrodes is used to measure the corresponding voltage drop, as seen in Fig. 5.4(b). The geometry used in our samples is pictured in the insets of Fig. 5.5. A known current I_1 is applied to the outer electrodes (1 and 4 in Fig. 5.4(b)), and the voltage drop is measured between the inner electrodes (2 and 3). Current I_2 that flows between the inner electrodes and enables the voltage measurement is much less than I_1. The measured voltage drop across the inner electrodes is $V = (I_1 + I_2)R + I_2(2R_c)$, where R is the resistance of the sample in the gap between the inner electrodes, and R_c is the contact resistance of the inner electrodes. Since I_2 is small compared to I_1, it can be neglected in the first term, and the second term drops out completely. Thus, $V \approx I_1 R$, and the conductivity σ is computed similarly to the two-point measurement, $\sigma = (L/A)/R$, except that L is now the distance between

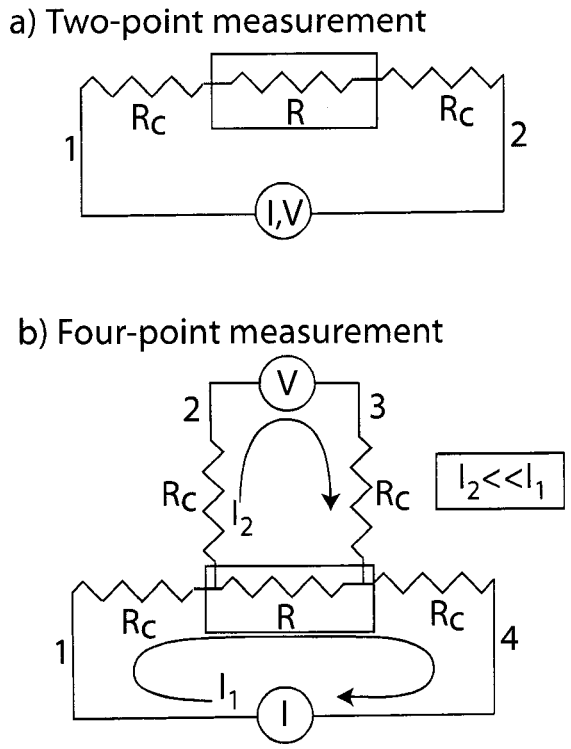

Figure 5.4: (a) In a two-point configuration, the resistance of a sample, R is measured by applying a voltage across the sample and measuring the resultant current (or by applying a current and measuring the voltage drop) using two contact points on the sample. If the contacts are not ideal, an additional resistance, R_c, exists, and the measured resistance will be $R + 2R_c$. (b) In systems where R_c is significant, a four-point configuration can be used. A known current I is applied across the sample, and a separate set of electrodes is used to read the voltage drop. Although a contact resistance, R_c is present at each contact, the true resistance of the sample, R, can be obtained (see text).

the inner electrodes, and not the length of the whole sample. When applied to our composites, the four-point measurement leads to linear IV curves, as shown in Fig. 5.5. All our composite samples with conductivities $\sigma > 10^{-10}$ S/cm were measured with the four-point method. For more insulating samples, it is more appropriate to use a specialized two point method as described in the next section.

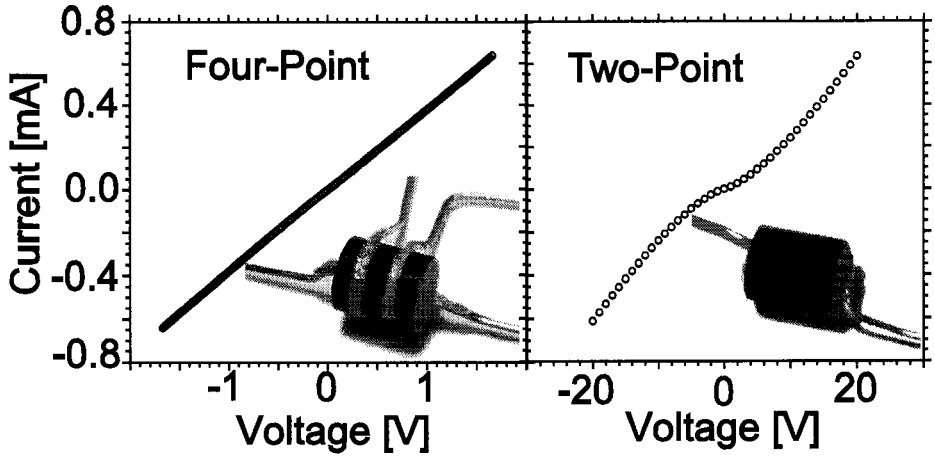

Figure 5.5: Two-point and four-point I-V curves for a non-sonicured HiPco SWNT composite at 1.6×10^{-4} SWNT volume fraction show a typical response of our samples. The insets show composite samples mounted for two- and four-point conductivity measurements. At a given current, the measured voltage in two-point measurements is significantly higher than in four-point due to both contact resistance and a larger separation between electrodes.

5.4.2 High impedance measurements

Accurate resistivity measurements of very highly resistive samples (More than $\sim 10^9$ Ω) require special precautions and methods. In such measurements, the current generated by the applied voltage is usually very small, of the order of nanoamperes. Therefore, background and leakage currents, as well as capacitative effects, can significantly distort the measurement. Background currents arise from charge stored in the material (dielectric absorption), static or triboelectric charge, or piezoelectric effects. These currents exist independently of the applied current, and can flow in either direction, changing the apparent conductivity up or down. To counteract these effects, as well as the effect of transient capacitative currents from the leads, contacts, electronics, and the samples themselves, an alternating polarity method was used in our measurements [4].

In this method, a DC voltage, $+V$, is applied across the sample for a set period of time (typically 30 s in our measurements). For highly resistive samples, the resulting measured current will be very small, and will not be constant. Instead, capacitative effects within the sample and the

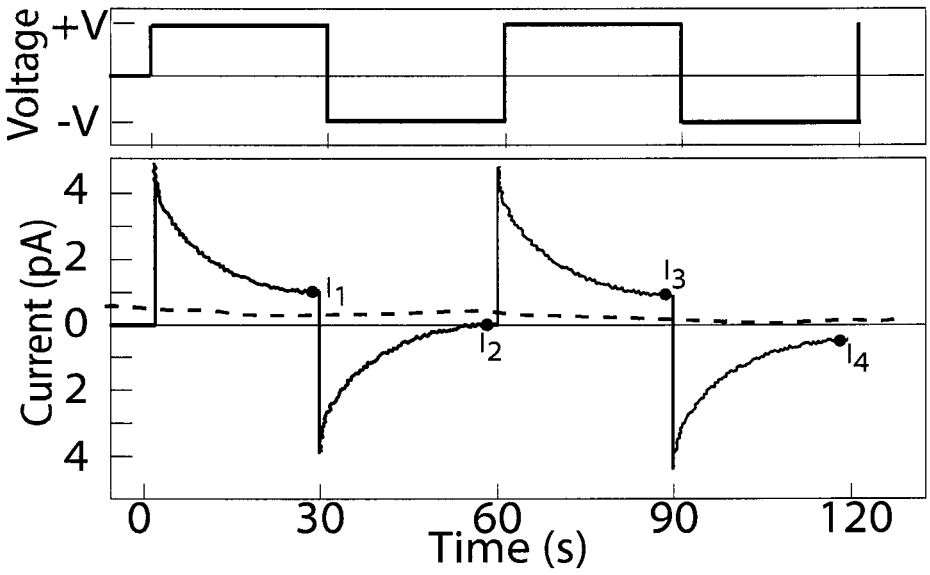

Figure 5.6: A two-point alternating-bias method is used to measure highly resistive composite samples. The applied voltage is alaternated between positive $(+V)$ and negative $(-V)$ values, and the measured current in each step approaches an asymptotic value. The method takes into account capacitative effects as well as a drifting background (dashed line) to establish the resistance of the sample, as explained in the text.

measurement electronics will cause an initial current spike, followed by an exponential decay, as seen in Fig. 5.6. The asymptotic value of this exponential decay curve may be found with relative ease, but this value may or may not reflect the true conductivity of the sample. For example, a DC current offset may be present due to instrumental limitations and static or induced charges in the material or measurement electronics. To counteract this effect, the polarity of the applied voltage is switched to $-V$, and the measurement is repeated. If no offset is present, a mirror-image of the first measurement will be produced around the zero-current axis. If an offset is present, the new measurement will be mirrored around the offset value, not zero. The constant offset can then be removed from the measurement by averaging the measured asymptotic current values of each segment. For example, a positive bias voltage $(+V)$ is applied for 30 s, a sufficient time to approach near the asymptotic current value, and the current (I_1) is read at the end of this time. A negative bias

$(-V)$ is then applied, and the current (I_2) is measured also at 30 s. The calculated current due to the voltage bias, minus any DC offset is $I_{calc} = (I_1 + (-I_2))/2$. It is frequently advantageous to repeat this procedure several times (4 - 6 cycles in our measurements) to obtain higher-order corrections with each flip of the polarity, as depicted in Fig. 5.6. While the first positive-negative segment pair cancels a DC offset, a third measurement will apply a correction to account for any drift in the DC offset, while a fourth measurement will further correct for curvature in the drift. Each subsequent $+V$ or $-V$ segment is averaged with the other measurements and weighted with the binomial coefficients of that order. For example, if three segments are measured - $(+V,I_1)$,$(-V,I_2)$, and $(+V,I_3)$ the calculated current due to the voltage bias is $I_{calc} = (I_1 + 2(-I_2) + I_3)/4$. If a fourth measurement $(-V,I_4)$ is added, $I_{calc} = (I_1 + 3(-I_2) + 3(I_3) + (-I_4))/8$, and so forth. Given the bias voltage and calculated current, the sample resistance is calculated from Ohm's law as usual.

Another potential difficulty in measuring samples of very high resistance is due to leakage current that can arise from several sources. These sources include insufficient insulation between the leads or inadequately shielded measurement electronics, surface contamination of the sample (even very thin layers of grease or other substances can have comparatively large conductivities), and high humidity. The Keithley 237 source meter used in all of our conductivity measurements is well suited to high resistance measurements. According to the operator's manual, the Keithley 237 is capable of measuring currents in the range ± 10 fA and ± 100 mA and voltage from ± 10 μV to ± 110 V, and can source currents from ± 100 fA to ± 100 mA and voltage from ± 100 μV to ± 110 V. Triaxial cables are used to connect the source meter to the sample. These cables have three concentric layers of conductors, with insulation between each layer. The outer conductor is the ground, and the middle wire is the "live" wire that carries the bias voltage. The conductor between these is called the guard, and is held at the same voltage as the inner conductor, but is

independent of it. Any leakage current to ground in the leads occurs between the guard and the outer conductor, and does not affect the measurements. Per specifications, the resistance between the live lead and the inner shield is $> 10^{15}\ \Omega$. It was discovered early on that surface contamination of the samples can significantly affect the measurements. All samples were cleaned with acetone and isopropyl alcohol immediately prior to measurement. Air humidity was not controlled in our measurements; however, since the epoxy surface is hydrophobic, water condensation on the sample is not a significant issue, though it might be with other materials. It was also found that minimizing air currents around the sample significantly reduced measurement noise, presumably by reducing static charge and heating effects.

5.4.3 Sample preparation

The electrical conductivities of the SWNT-epoxy composites are determined by two- and four-point contact direct-current (DC) conductivity measurements. Most of the measurements were obtained by the four-point method described above in order to eliminate contact resistance effects, while highly resistive samples, those with conductivities of less than 1×10^{-10} S/cm, were measured by the alternating-bias two-point method described above.

For two point measurements, the flat surfaces of the cylindrical composite samples were painted with conductive paint (product number 4929N, DuPont). For four point measurements, the samples were further prepared by roughening the curved surface of the cylindrical samples and painting conductive rings around their circumference with spacing of approximately 1mm. Copper leads were attached to these electrodes with the same conductive paint. (See insets in Fig. 5.5.) The measurement error for the conductivity was $\leq 1\%$, and the nanotube volume fraction was known to within 10%. The sensitivity limit of our apparatus was approximately 1×10^{-14} S/cm, as indicated

by the shaded gray areas in Fig. 5.8. We confirmed the conductivity was isotropic; conductivities measured along three perpendicular axes were within 25% of one another. Weak aging effects were also observed in our composites. After a period of two months, the conductivities of all samples were observed to decrease by approximately 50%. The conductivity recovered to 75% - 100% of its original value after heating at 110° C for one hour. To discount the possibility of ionic conduction through any remaining solvent, control samples were prepared that underwent the same processing with pure DMF in place of the SWNT/DMF dispersion. All of these control samples were insulating below the measurement noise floor.

5.5 Results

A series of composite samples with increasing SWNT concentration is shown in Fig. 5.7(a). Our SWNT-epoxy composites exhibit a range of microscopic morphologies evident from optical microscopy of thin sections and scanning electron microscopy (SEM) of fractured surfaces (see Fig. 5.7). An example of a 'non-sonicured' sample is shown in Figs. 5.7(b) and 5.7(d). Reaggregation of SWNTs is clearly evident as bright and dark regions in the optical images. These diffuse aggregates are roughly 10 μm in diameter. SEM imaging confirms that nanotube density varies on a similar length scale. Ropes of SWNTs are distributed in clusters on the fractured surfaces. These clusters are easily dispersed under continued sonication just prior to curing. An example of a disaggregated 'sonicured' sample is shown in Figs. 5.7(c) and 5.7(e). The optical and SEM images show the SWNT distribution is quite homogeneous down to a few micrometers, and although some aggregates are present, their density is relatively low. We suspect the epoxy resin itself partially stabilizes the suspension [135] once the DMF evaporates, facilitating this dispersion. It is important to distinguish the diffuse features in our 'non-sonicured' samples from dense

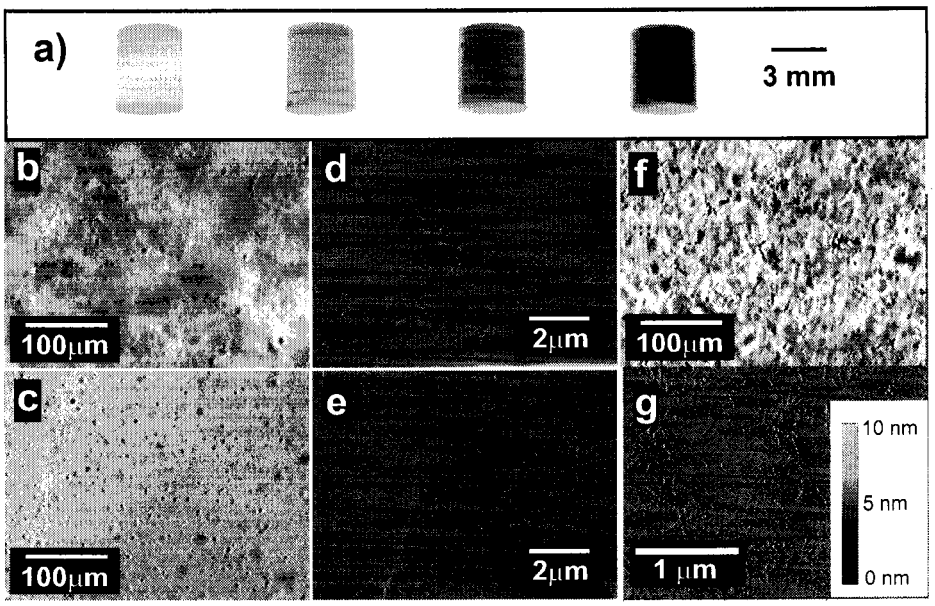

Figure 5.7: (a) Photographs of composites. SWNT volume fractions, from left to right, are 2.6×10^{-5}, 5.2×10^{-5}, 1.0×10^{-4}, and 1.5×10^{-4}. (b) - (f). Images of composites (SWNT volume fraction 2.1×10^{-4}). Information about SWNT distribution in the composites can be obtained from transmitted light microscopy through thin ($\sim$300 μm) slices ((b),(c), and (f)), and from scanning electron microscopy (SEM) of fractured surfaces ((d) and (e)). (b) In a *non-sonicured* sample, dark and bright regions correspond to high and low SWNT concentrations, respectively. (d) In SEM images of the same *non-sonicured* composite, SWNT ropes (white strips) appear in $\sim$10 μm clusters on the surface. Here, the ropes are present only in the lower left quadrant of the field of view. (c) The more uniform gray color in this *sonicured* composite implies a more uniform SWNT distribution than in (b). (e) SEM image of a *sonicured* sample shows that SWNT ropes are distributed more uniformly across the fractured surface than in (d). (f) Dense aggregates are seen in a *non-sonicured* composite made from a more concentrated SWNT/DMF starting dispersion at 0.04 wt% (see text). (g) Tapping mode AFM image of laser-oven SWNTs adsorbed over 30 minutes onto an HMDS treated silicon wafer from a well sonicated, dilute DMF-SWNT suspension.

aggregates that result from a poor initial dispersion. A sample made from a 0.04 wt% SWNT-DMF suspension, shown in Fig. 5.7(f), has substantially larger numbers of dense aggregates, which presumably exist in the more concentrated starting suspensions and persist throughout processing.

In Fig. 5.8 we show the conductivity, σ, of the non-sonicured and sonicured laser-oven and HiPco composites as a function of SWNT volume fraction ϕ. All four sets of composites exhibit a jump in σ of 2 to 6 orders of magnitude over a small change in ϕ, i.e., a percolation-like behavior.

Near this threshold, we find $\sigma \propto (\phi - \phi_c)^s$; hereafter we refer to ϕ_c as the threshold volume fraction. To determine ϕ_c and s, logarithms of the measured conductivity σ and volume fraction ϕ are compared to the equation $\log(\sigma) = \log(C_0 + A(\phi - \phi_c)^s \times \Theta(\phi - \phi_c))$ where C_0 is the constant background conductivity of the points below the threshold, A is a constant that depends on nanotube conductivity and network morphology, and $\Theta(\phi - \phi_c)$ is the Heaviside step function such that $\Theta(x) = 0$ when $x < 0$ and $\Theta(x) = 1$ when $x > 0$. Two-point measurements above the threshold are excluded from the fits to avoid systematic errors due to contact resistance.

A least-squares analysis of the fits show that ϕ_c for each set of composites is strongly bounded by the regions between the highest insulating and lowest conducting points. The exponent s, however, is not well bounded. The fit results for ϕ_c and s are summarized in Table 5.2. Plots of $\log(\sigma)$ vs. $\log(\phi - \phi_c)$ in the insets of Fig. 5.8 show the conducting composite samples with best-fit line whose slope provides the best-fit exponent s. The lowest measured threshold volume fraction is obtained for the non-sonicured laser-oven SWNTs; its value of 5.2 (+1.9/-0.5)$\times 10^{-5}$is approximately 10 times smaller than the lowest threshold concentration reported to date for SWNTs in epoxy [84]. Electrostatic dissipation applications typically require a conductivity of about 10^{-5} S/cm, which is reached when $\phi \approx 5 \times 10^{-4}$ ($\sigma \approx 10^{-4}$ S/cm at $\phi = 10^{-3}$). The magnitude of the conductivity is comparable to some results obtained for MWNT in epoxy composites; note, however that the length scale for inhomogeneity is $\sim$10 μm or less for sonicured and non-sonicured samples (Fig. 5.7), compared to $\sim$1 mm in MWNT epoxy samples [131]. Two other facts are clearly revealed in the data. First, the thresholds observed in the sonicured samples are higher (i.e., by $\sim 2\times$) than the non-sonicured samples. Evidently sonication disaggregates and homogenizes SWNTs better just prior to curing, but the more reaggregated composites percolate more readily. Second, the laser-oven SWNT composites have approximately twofold lower thresholds than corresponding

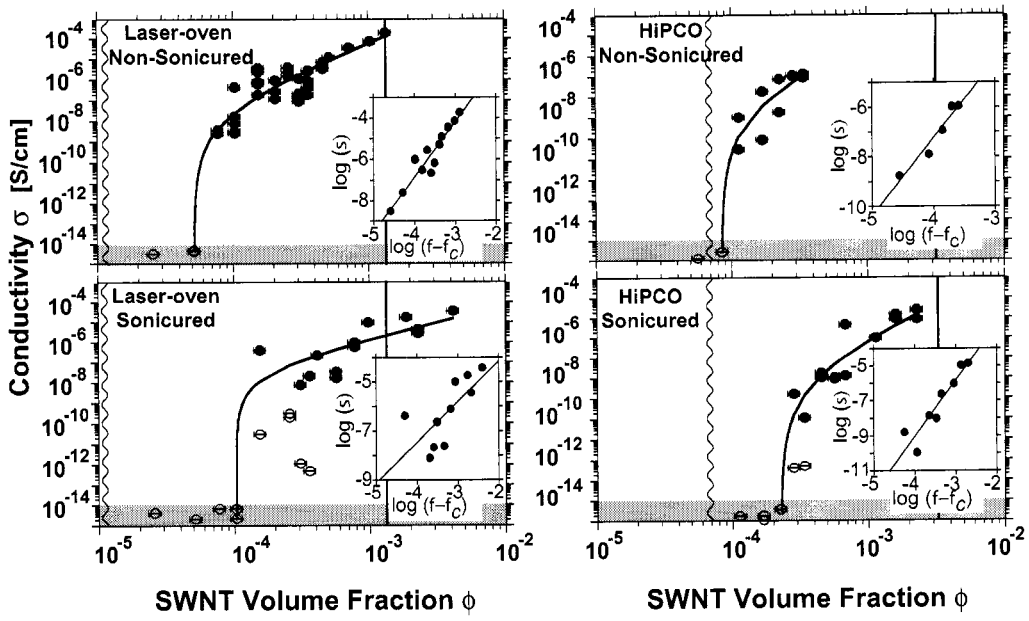

Figure 5.8: Conductivity σ as a function of SWNT volume fraction ϕ for non-sonicured and sonicured laser-oven and HiPco samples. The vertical lines on the charts indicate approximate transitions from dilute to semi-dilute regimes (wavy) and semi-dilute to concentrated regimes (solid). Each point on the plot represents a separately made composite. The observed scatter in conductivity is likely caused by small variations in processing conditions between samples. In contrast, the conductivities of different sections of the same sample were never more than 50% of each other. Filled circles represent four point measurements. Open circles depict two point alternating bias measurements. Points in shaded areas are below the baseline of our equipment. Connecting curves reflect the predicted behavior according to the best fits for the observed threshold ϕ_c and the exponent s. Insets show plots of $\log(\sigma)$ as function of $\log(\phi - \phi_c)$ for the same data sets, where multiple points at the same concentration have been binned prior to fitting. Best fit lines determining ϕ_c and s are shown.

HiPco SWNT composites. This trend is qualitatively consistent with the expectations of simple models for percolation in random rod networks discussed below, which scale with rod length and diameter.

5.6 Discussion

Since individual SWNTs behave somewhat like rigid rods in solution [163], it is useful to consider our observations in light of the predictions made by simple percolation models for isotropic dispersions of rodlike particles described in chapter 4. Such dispersions are classified by Doi-Edwards

theory into dilute, semi-dilute, and concentrated regimes [37], For non-interacting rods, the percolation threshold occurs near the transition between semi-dilute and concentrated regimes, where the rod number density is roughly the reciprocal of the excluded volume of the rod, v_{excl} [11, 12, 24], which here can be approximated by $v_{\mathrm{excl}} \approx \pi L^2 d/2$, where d and L are as defined earlier. The threshold is thus predicted to be at a volume fraction $\phi_1 \approx d/2L$. While valid for systems of non-interacting rods, this model has had limited success predicting the percolation-like behavior of strongly interacting nanotube systems. Attractive interactions can lower threshold concentrations when the particles assemble to form long chains. The simplest model for these attractive systems assumes that the limiting concentration at which continuous chains can form occurs near the transition between dilute and semi-dilute regimes, where the rotational motion of each rod is obstructed by the presence of other rods [26, 27, 116]. Here, the volume occupied by each rod is a sphere of diameter L, or $\nu_0 \approx \pi L^3/6$, and the critical volume fraction is $\phi_0 \approx 3d^2/2L^2$. This model predicts a significantly lower threshold than the excluded volume picture described above, and provides a lower-bound for the position of the threshold when the rods are distributed randomly. It is thus reasonable that the threshold should be observed in the semi-dilute regime between the two limiting cases described above.

Although these models oversimplify the situation in our composites, they do give a range of concentrations wherein the threshold can be expected. If we approximate our laser-oven (HiPco)

	Laser-oven		HiPco	
	Non-sonicured	Sonicured	Non-Sonicured	Sonicured
Threshold Volume Fraction ($\phi_c \times 10^{-5}$)	5.2 (+1.9/-0.5)	10 (+2/-1)	8.5 (+1.0/-0.9)	23 (+2/-2)
Best-fit Exponent (s)	2.7 (+0.4/-0.8)	1.6 (+0.5/-0.6)	3.1 (+1.2/-1.7)	3.2 (+0.5/-0.6)
Dilute/semi-dilute transition (ϕ_0)	1×10^{-5}	1×10^{-5}	6.5×10^{-5}	6.5×10^{-5}
Semi-dilute/concentrated transition (ϕ_1)	1.3×10^{-3}	1.3×10^{-3}	3.3×10^{-3}	3.3×10^{-3}

Table 5.2: Table of observed thresholds, exponents, and predicted thresholds for the four data sets. All numbers are given in terms of SWNT volume fraction.

samples as homogeneous rod distributions with length 516 nm (167 nm) and diameter 1.35 nm (1.1 nm), then we can define limiting theoretical percolation thresholds using the simple models outlined above. The wavy and solid lines in Figure 5.8 correspond to dilute/semi-dilute and semi-dilute/concentrated transition points, respectively. Thresholds for all four sets of composites are observed in the semi-dilute regime, as expected in a system of attractive rods. This result is also consistent with rheological studies of surfactant stabilized SWNTs in solution, where rigidity percolation was observed in the semi-dilute regime at $\phi = .0026$ [65]. The models also make quantitative predictions about the ratio of the HiPco threshold to the laser-oven threshold. The observed threshold ratio for our composites was 1.7 for non-sonicured samples and 2.2 for sonicured samples. If the samples were overlap volume limited (i.e., ν_0 limited), then the predicted ratio is 6.5. If the samples were excluded volume limited (i.e., $1/v_{\mathrm{excl}}$ limited), then the observed ratios are predicted to be 2.5. Although closer to the latter ratio, our observations do not agree with either model. Another testable prediction is the percolation exponent s. The confidence intervals for our exponents were large and their best fits ranged from 1.6 (+0.5/-0.6) to 3.2 (+0.5/-0.6). Computer models of conductivity percolation predict a critical exponent value [109] of 2. Other experimental studies of carbon nanotube composites have frequently cited values [84, 113, 120, 131] between 1.3 and 2, while exponents of 3.1 were observed in disordered short carbon fiber composites [151].

In summary, we have developed a methodology to disperse purified SWNTs into epoxy and we have investigated the electrical conductivity in these composites as a function of SWNT length, type, and dispersion homogeneity. All four varieties of our composites exhibited percolation-like thresholds in the semi-dilute concentration regime. The lowest thresholds were observed when SWNTs were allowed to re-aggregate, and these were significantly lower than have been previously reported for SWNTs in epoxy.

Chapter 6

Thermal Conductivity of SWNT/Epoxy composites

6.1 Background

The thermal conductivity of SWNTs possibly surpasses even that of diamond and multi-wall carbon nanotubes (see [17, 60, 62] and chapter 2). Thus there continues to be substantial interest in SWNTs as additives for enhancing the thermal conductivity of insulating materials. For instance, multi-functional materials that provide the physical strength and light weight of epoxy combined with high thermal and/or electrical conductivities would find numerous aerospace and semiconductor applications. While thermally conductive epoxy composites utilizing various fillers are commercially available, they offer relatively poor thermal enhancement, and often at the expense of mechanical strength. Table 6.1 summarizes the properties of some commercially available thermally conductive epoxies. The potential for carbon nanotubes to offer improvement over current technologies, however, will depend on better understanding and control of many factors including

Epoxy brand name	Filler type	Thermal conductivity (W/m-K)
Resin Technology Group TIGA F-715	Not avail.	1.4
3M TC2810	Boron Nitride (24 wt%)	0.8-1.4
TimTronics TIM-811 to TIM-816	Not avail.	1 - 1.8

Table 6.1: A comparison of some commercially available thermally conductive epoxies. The values quoted are provided by the manufacturer.

thermal interfacial resistances arising between SWNTs and the surrounding matrix, and the quality and nature of the nanotube network.

Thermal conductivity enhancements due to inclusions of raw (unpurified) carbon nanotubes in epoxy [19], silicon elastomer [99], and oil [30] have been reported. The degree of enhancement in these studies at 1 wt% loading varied substantially (from $\sim$15 % [99] to $\sim$160 % [30]), perhaps as a result of nanotube type (single- vs. multi-wall tubes), dispersion quality, nanotube purity and length, composite preparation, and thermal interfacial resistance, R_K. Indeed, R_K was found to be quite large in recent laser pump-probe measurements of dilute aqueous suspensions of SDS surfactant-stabilized SWNTs [69]. Theoretical models [28, 104–106] for these thermal transport processes and related simulations [47, 136] have also been developed.

We report on thermal conductivity measurements of *purified*-SWNT-in-epoxy composites in a comparative study of two practical starting formulations. Both achieve fairly homogeneous SWNT distributions within the epoxy matrix using either surfactant stabilized aqueous SWNT suspensions (surfactant-processed) or metastable SWNT / N-N-Dimethylformamide (DMF) suspensions (DMF-processed). To our knowledge, this is the first thermal conductivity study of SWNT composites to use highly purified SWNTs. Raw SWNT material often contains significant carbonaceous and metallic impurities on SWNT surfaces and in the bulk, which can adversely affect composite performance and complicate quantitative analysis of composite properties. The conductivity enhancements are (27 ± 5) % in the DMF-processed composites at SWNT volume fractions $\phi \sim 0.005$,

and (64 ± 9) % in the surfactant processed samples at $\phi \sim 0.1$. Analytical fits of effective medium theory to our measurements provide first estimates of SWNT interfacial resistance in solid composites, and demonstrate tenfold larger R_K in surfactant processed samples compared to DMF processed samples. The increase in R_K may be attributed to a surfactant layer coating the SWNTs.

6.2 Materials and Preparation

SWNTs produced by the high pressure decomposition of carbon monoxide (HiPco) method (Carbon Nanotechnologies, Inc., batch 79) are obtained in raw form and are purified as described in Ref. [77]. The purified material contains > 90 wt% SWNTs, < 5 wt% carbon-derivative, and ≤ 0.96 wt% magnetic catalyst [21, 73]. The electrical properties of the purified SWNTs were not significantly affected by purification [77]. Atomic force microscopy (AFM) measurements of the SWNT dimensions give a mean length of $L = 167 \pm 90$ nm and a mean diameter of $d = 1.1 \pm 0.3$ nm [75]. Longer laser-oven SWNTs ($L = 516 \pm 286$ nm, $d = 1.35 \pm 0.15$ nm) also used in this study are purified and processed in a similar way [74].

Both DMF- and surfactant-processed samples are prepared with identical procedures, differing only in the initial SWNT suspension. See chapter 5 for the details of the preparation.

DMF-processed samples use a very dilute (0.0004 wt%) suspension of SWNTs in DMF [21]. Surfactant-processed samples use a dilute (0.005 wt%) aqueous suspension of sodium dodecylbenzene sulfonate (NaDDBS) surfactant stabilized SWNTs [75]. The weight ratio of NaDDBS to SWNTs in these suspensions is 1:1. The starting suspension is added to the epoxy resin (Miller Stephenson Epon 828) and the solvent is allowed to evaporate prior to crosslinking (Miller Stephenson EpiKure 3234). Details of the process and electrical conductivity measurements for the DMF-processed samples are reported in Ref. [21]. In DMF-processing, the resin becomes highly viscous

at $\phi > 0.005$, while in surfactant processing SWNT volume fractions as high as $\phi = 0.1$ are possible. This difference may be attributed to the longer gelation time of the surfactant stabilized samples [65], but both types of processing produced homogeneous dispersions of SWNTs in the matrix, down to a length scale of a few μm. The SWNT volume fraction, ϕ, was determined by using the calculated value for SWNT density of [48] 1.4 g/cm^3 and the measured density of cured pure epoxy [21] (1.2 ± 0.02 g/cm^3).

6.3 Thermal conductivity measurement

Thermal conductivity measurements follow the 'two thermometer, one heater' method using a custom-built stage designed for the Quantum Design Physical Property Measurement System (PPMS). Cernox thermometers (LakeShore Cryotronics, Inc.) monitor the temperature of two polished oxygen-free high conductivity (OFHC) copper plates contacted to the ends of a cylindrical ($\sim$5.3 mm height $\times$ $\sim$4.7 mm diameter) sample. A 10 kΩ surface mount resistor heats the top plate (10 mm diameter $\times$ 1 mm thick) to a temperature T_{Hot}. Heat flows from the top plate, through the sample, and into the bottom plate which is thermally grounded to T_{Cold} by the PPMS. Apiezon N-grease enhances thermal contact to the sample [50]. A gold-plated radiation cap around the stage fixed at T_{Cold} and a high vacuum ($< 10^{-5}$ Torr) reduce thermal losses due to radiation and convection, respectively.

A typical measurement (see Fig. 6.2) consists of incrementing the heater current in four to five steps. Temperature differentials ($\Delta T = T_{Hot} - T_{Cold}$) of $\sim$0.2 to 2.5 K are allowed to stabilize between each step for $\sim$3 hours, and thermal conductivity, κ, is extracted from the slope of applied

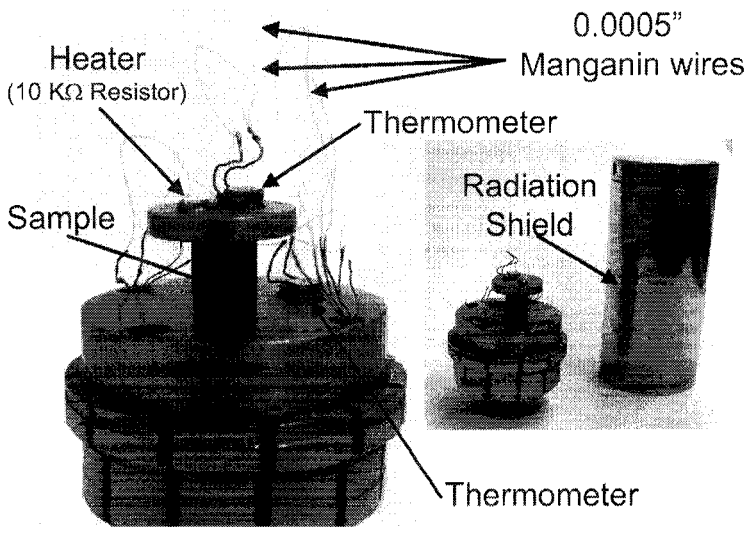

Figure 6.1: Photograph of thermal conductivity measurement setup

power I^2R versus ΔT according to

$$I^2R = (\frac{\kappa\pi r^2}{L} + K_{Loss})\Delta T + P_{Rad}, \tag{6.1}$$

where r and L are the cylindrical radius and length, respectively, and $K_{Loss}\Delta T$ is the total heat loss through the manganin electrical leads and residual gas.

The heat loss due to radiation, P_{Rad}, is estimated by the Stefan-Boltzmann Law,

$$P_{Rad} = (\epsilon_1\epsilon_2/(\epsilon_1 + \epsilon_2 - \epsilon_1\epsilon_2))\sigma A_H(T_{Hot}^4 - T_{Cold}^4). \tag{6.2}$$

Here, ϵ_1 and ϵ_2 are the emissivities of the hot and cold surfaces, σ is the Stefan-Boltzmann constant, and A_H is the area of the hot surface. This formulation is valid for reflecting concentric cylinders and parallel planes [132]. The maximum calculated radiative loss (at $\Delta T = 2.5$ K) from the heated top plate, given $A_H = 2 \times 10^{-4}$ m^2 and $\epsilon_1 = \epsilon_2 = 0.05$ for polished metal [117], is ~3 % of the applied power. Additional radiative losses also occur from the temperature gradient in the

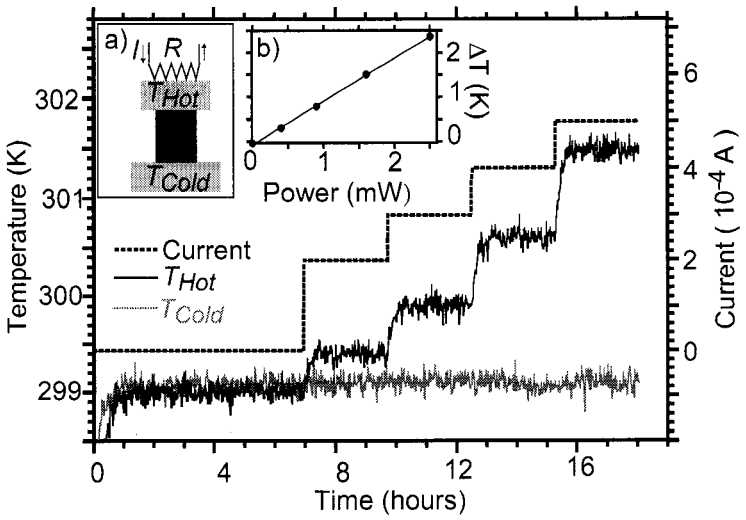

Figure 6.2: Inset (a) depicts the measurement setup. The main plot shows the applied current and corresponding temperature response of the top and bottom plates. In inset (b), the slope of the applied power (I^2R) versus the temperature differential (ΔT) gives the thermal conductance of the sample, from which thermal conductivity is extracted.

sample itself. Assuming a worst-case $\epsilon = 1$ for the samples, the maximum radiative loss from the sample surface is ~1.2 % of the applied power. K_{Loss} was estimated by measuring a styrofoam cylinder and a hollow polystyrene straw with geometries nearly identical to the composite samples. The experiments clearly indicated that $K_{Loss} \gg \kappa\pi r^2/L$ for these insulators, and K_{Loss} was determined to be $(4.18 \pm 0.09) \times 10^{-4}$ W/K.

6.4 Results and discussion

The measured thermal conductivities are shown in Fig. 6.3. DMF-processed samples exhibit a modest enhancement of κ in the range $\phi \approx 0.001$ to 0.005. At $\phi = 0.005$, the enhancement is about (27 ± 5) % over pure epoxy. In contrast, surfactant processed composites exhibit no measurable enhancement below $\phi \approx 0.01$, and (64 ± 9) % at $\phi = 0.1$. The electrical conductivity

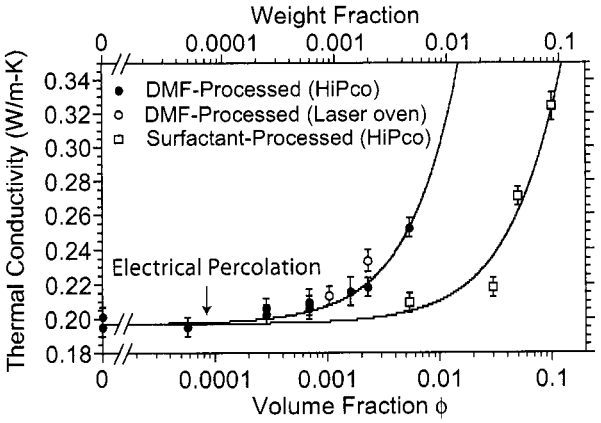

Figure 6.3: Thermal conductivity of DMF-processed and surfactant-processed samples. The fits shown assume SWNT dimensions ($L = 167$ nm, $d = 1.1$ nm), thermal conductivities of SWNTs ($\kappa_{swnt} = 3000$ W/m-K), and epoxy ($\kappa_m = 0.198$ W/m-K). The thermal interface resistance (R_K) is the free fit parameter. ϕ is known to within $\pm$ 10 %.

of DMF-processed composites undergoes a discontinuous change of about five orders of magnitude [21] near the threshold volume fraction of $\sim 1 \times 10^{-4}$, but no such discontinuity is observed in the thermal conductivity. Thus electrical percolation has no significant effect on the thermal conductivity enhancement, consistent with a phonon-dominated picture of SWNT thermal transport. Effective medium theory is suitable when percolation effects can be neglected, and enables estimation of the interfacial resistance R_K at the SWNT/matrix interface.

A formulation of effective medium theory appropriate to the present case [2] considers a system of randomly oriented rods in a host medium [105]. The effective thermal conductivity of the composite is

$$\kappa_{eff} = \kappa_m \frac{(3 + \phi(\beta_\perp + \beta_\parallel))}{(3 - \phi\beta_\perp)}, \tag{6.3}$$

where

$$\beta_\perp = \frac{2(d(\kappa_{swnt} - \kappa_m) - 2R_K\kappa_{swnt}\kappa_m)}{d(\kappa_{swnt} + \kappa_m) + 2R_K\kappa_{swnt}\kappa_m}, \tag{6.4a}$$

$$\beta_\parallel = \frac{L(\kappa_{swnt} - \kappa_m) - 2R_K\kappa_{swnt}\kappa_m}{L\kappa_m + 2R_K\kappa_{swnt}\kappa_m}, \tag{6.4b}$$

Composite type	enhancement	R_K (m^2K/W)
SWNT / epoxy (DMF)	80 % (fit)	$(2.4 \pm 1.3) \times 10^{-9}$
SWNT / epoxy (Surf.)	< 8 %	$(2.6 \pm 0.9) \times 10^{-8}$
SWNT / epoxy [19]	125 %	-
MWNT / silicone [99]	$\sim$15 %	-
MWNT / oil [30]	160%	8×10^{-8} (See Ref. [105])
SWNT / water [69]	-	8.3×10^{-8}

Table 6.2: Table of thermal conductivity enhancements and calculated interfacial resistances. Enhancements are quoted for 1 wt% nanotube loadings, except for Ref [30], which is quoted for 1 vol% SWNT.

and the thermal conductivities of the epoxy and SWNTs are κ_m and κ_{swnt}, respectively. Our measurements of pure epoxy give $\kappa_m = 0.198 \pm 0.005$ W/m-K. Published measurements and simulations bound κ_{swnt} between [62] 1750 W/m-K and [17] 6600 W/m-K. We use a value of 3000 W/m-K for fitting. AFM measurements of HiPco SWNTs give mean length $L = 167$ nm and mean diameter $d = 1.1$ nm. Given these parameters, we obtain fits to our data, as shown in Fig. 6.3, with $R_K = (2.4 \pm 1.3) \times 10^{-9}$ m^2K/W for DMF-processed samples and $R_K = (2.6 \pm 0.9) \times 10^{-8}$ m^2K/W for surfactant-processed samples. The enhancement predicted at 1 wt% SWNTs ($\phi = 0.012$) for DMF processed composites is 80%, compared to 125% obtained in earlier studies of similar SWNT epoxy composites [19]. The difference may be attributed to several factors, including the lower aspect ratio of HiPco SWNTs compared to laser-oven SWNTs [75] used in the previous study and the differences between raw and purified starting dispersions. Limited measurements of laser-oven SWNT DMF-processed composites (see Fig. 6.3) appear in the same range as the HiPco data. Table 5.2 compares our results to other studies.

The difference in the interfacial resistance between the DMF-processed and surfactant-processed samples is attributed to the surfactant which coats the SWNTs and reduces heat transfer. The value for R_K obtained by laser pump-probe measurements for SDS surfactant stabilized aqueous SWNT

suspensions was $R_K = 8.3 \times 10^{-8}$ m^{2}K/W [69], comparable to our surfactant-processed solid-epoxy results. Clearly, interfacial resistance limits the utility of SWNTs for enhancing thermal properties of insulating materials. Comparative measurements of this parameter, such as those presented here, can elucidate contributing factors and ultimately lead to materials with reduced interfacial resistance and higher composite thermal conductivity.

Chapter 7

Carbon Nanotube Aerogels

7.1 Background

Aerogels are ultra-light, highly porous materials typically made by subjecting a wet gel precursor to critical-point drying (CPD) or lyophilization (freeze drying) in order to remove background liquid without collapsing the network. Microscopically, aerogels are composed of tenuous networks of clustered nanoparticles, and the materials often have unique properties, including very high strength-to-weight and surface-area-to-volume ratios. To date most aerogels are made from silica [66] or pyrolized organic polymers [114, 115]. Practical interest in the former stems from their potential for ultra-light structural media, radiation detectors and thermal insulators [66], and, in the latter, from their potential for battery electrodes and supercapacitors [115]. Table 7.1 summarizes some key properties of silica an carbon aerogels. Here we investigate the properties of a new class of aerogels based on carbon nanotubes (CNTs). Small-diameter carbon nanotubes, such as single- and few-wall carbon nanotubes, are exciting candidates for electrically conducting aerogels. Individually, these nanotubes are extraordinarily stiff [38] and their electrical conductivity can be

Aerogel type	Electrical Conductivity (S/cm)	Thermal conductivity (W/m-K)	Density (g/cm^3)
Silica	N/A	$\sim$0.003	0.0019 - 0.1
Carbon	20	$\sim$0.4	$\sim$0.5

Table 7.1: Summary of some properties of carbon [114, 115] and silica [66] aerogels

very large [38, 89]. Furthermore, ensembles of such nanotubes make useful aerogel precursors. They form electrically percolating networks at very low volume fractions [21] and elastic gels in concentrated suspensions via van der Waals interaction mediated cross-linking [65, 148].

Here we report the creation of CNT aerogels from aqueous gel precursors by critical-point drying and freeze drying. Carbon nanotube aerogels have been produced previously as intermediate phases during the process of drawing nanotube fibers [96] from a furnace and during the process of making sheets from multi-wall carbon nanotube forests [160]. By contrast, our aerogels are derived directly from CNT networks in suspension, and we can readily manipulate the network properties as a result. The flexibility afforded by this process enables us to control CNT concentration, to utilize optimized CNT dispersion processes [75], to reinforce the networks with, for example, polyvinyl alcohol (PVA), and to infiltrate or backfill them with polymeric fluids. Here we describe these CNT aerogels, the processing methodologies used to synthesize them, and we characterize their electrical and mechanical properties. The CNT aerogels support thousands of times their own weight after PVA-reinforcement, and, depending on processing conditions, their electrical conductivity ranges as high as $\sim$1 S/cm. Although our starting chemical vapor deposition (CVD) nanotube material contains single- and few-wall carbon nanotubes (the latter being predominantly double-wall carbon nanotubes, DWNTs), the dispersion and preparation processes employed here are directly applicable to pure single-wall carbon nanotubes (SWNTs) [75]. The CNT aerogel electrical and structural properties reported here are also expected to be similar to pure SWNT

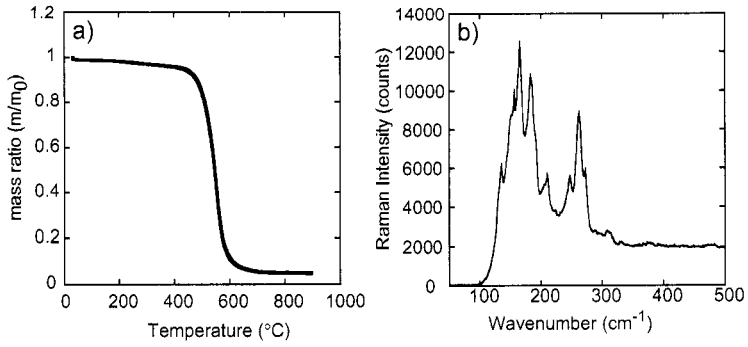

Figure 7.1: Nanotubes used in the experiment, Elicarb SW batch K1713 from Thomas Swan, Inc. are characterized by thermogravimetric analysis (TGA) and Raman spectroscopy. a) TGA analysis of the material reveals a metallic impurity content of <5 wt%. b) Raman spectroscopy (514 nm laser) exhibits some radial breathing modes (RBMs) at wavenumbers >250 cm^{-1}, suggesting the presence of DWNTs [13].

samples, because the electrical [156] and tensile [95] properties of bulk SWNTs and DWNTs are comparable.

7.2 Aerogel Preparation

7.2.1 Materials and wet gel preparation

CNTs were obtained from Thomas Swan, Inc. (Elicarb SW, batch K1713). The chemical vapor deposition (CVD) process used to produce this material aims to maximize single-wall carbon nanotubes (SWNTs), but some amounts of double- and triple-wall carbon nanotubes are also present [3]. We suspend the as-received CNTs in water with sodium dodecylbenzene sulfonate (NaDDBS) surfactant (Acros Organics) under 55KHz bath sonication [75]. In this solution, CNT weight fractions range from 0.005 to 0.013 (i.e., 5 to 13 mg/mL) and the surfactant:CNT weight ratio is 5:1. Higher CNT concentrations are impractical with this method because of aggregation. The CNT solution is poured into a cylindrical mold (4.7 mm diameter) and left overnight to set into an elastic gel [64, 65]. The gel is transferred to and then soaked in a large, heated (90°C)

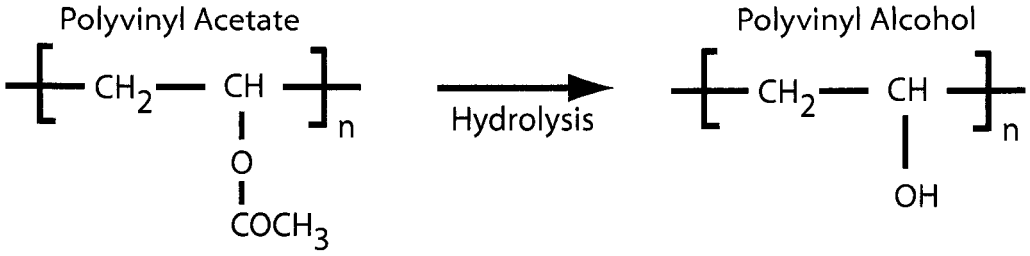

Figure 7.2: Polyvinyl Alcohol (PVA) is made by fully or partially hydrolyzing Polyvinyl Acetate, a hydrophobic polymer that is the main component of common household "white glue." In our experiments we use fully (100%) hydrolized PVA. Partially hydrolized PVA contains some acetate groups and is less soluble in water.

water bath containing added polyvinyl alcohol (PVA) (70,000-100,000 molecular weight, Sigma P1763). Polyvinyl alcohol is a water-soluble polymer created by hydrolyzing Polyvinyl Acetate, as shown in Fig. 7.2. The weight percent PVA used were 0.00 wt% (for unreinforced aerogels), 0.25 wt%, 0.50 wt%, 0.75 wt%, or 1.00 wt%. The bath solution is typically changed at least three times over the course of 3-5 days. This procedure effectively removes the surfactant, as evidenced by SEM and TEM imaging and by energy dispersive x-ray spectroscopy (EDX) (see Fig 7.3); the PVA reinforces the gel structure [149]. The samples are then cut into $\sim$5 mm long pieces and dried using methods described in the next section.

7.2.2 Critical-point drying and freeze drying

To create the aerogel, the background liquid is removed from the wet nanotube gel by either critical-point drying or freeze-drying. Unlike simple evaporation, in which surface tension of the evaporating liquid causes the gel network to collapse and shrink, these drying processes avoid the liquid/gas interface, removing the liquid while leaving the network largely intact. The principles of the processes are shown schematically in Fig. 7.4.

Freeze drying, also called lyophilization, is performed by freezing the sample and placing it

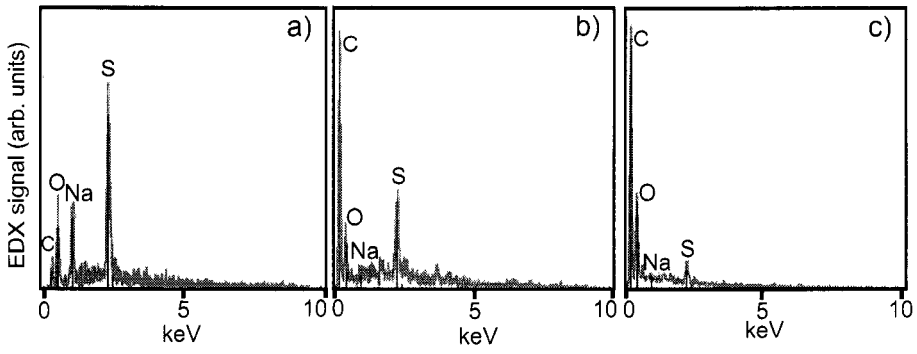

Figure 7.3: Elemental analysis by Energy Dispersive X-ray Spectroscopy (EDX) is used to qualitatively determine the effectiveness of the water bath for removing surfactant in PVA reinforced CNT aerogels. a) In an unwashed, unreinforced aerogel sample that contains sodium dodecylbenzene sulfonate (NaDDBs) surfactant, the elements carbon, oxygen, sulfur and sodium are evident. These elements are consistent with the composition of the surfactant. b) Aerogel sample after being placed in a 0.25 wt% PVA solution for three days at room temperature. The mobile sodium ion is effectively removed, but the presence of sulfur suggests that some surfactant remains. c) Aerogel sample placed in a 0.25 wt% PVA bath at 90°C for three days shows only trace amounts of sulfur and no sodium, suggesting the surfactant is effectively removed. The main peaks here are carbon and oxygen, likely from the nanotubes and PVA polymer.

in vacuum. The sample is then heated while under vacuum, causing the ice to sublimate into vapor. The triple point of water is at a pressure of 0.006 Atm and 0.01°C. If the pressure at the sample is lower than the triple point pressure while the sample is heated, the ice sublimates directly into gas. When using water, adequate vacuum can be obtained with relatively inexpensive roughing pumps. Freeze-drying is a common technique used in biology and in the food industry and is routinely performed on an industrial scale. Upon freezing, ice crystals form throughout the sample. While the crystals grow, they eject any material incompatible with the crystal lattice from the solidification front. This typically includes all materials other than the molecules in the crystal lattice. This process is called zone refinement. An example of zone refinement taken in the context of another experiment is shown in Fig. 7.5. As a result of this process, the carbon nanotubes in the gel can be displaced within the network during freezing. The size of the ice crystals, and therefore the displacement of the material, depends strongly on the growth rate of the ice crystals.

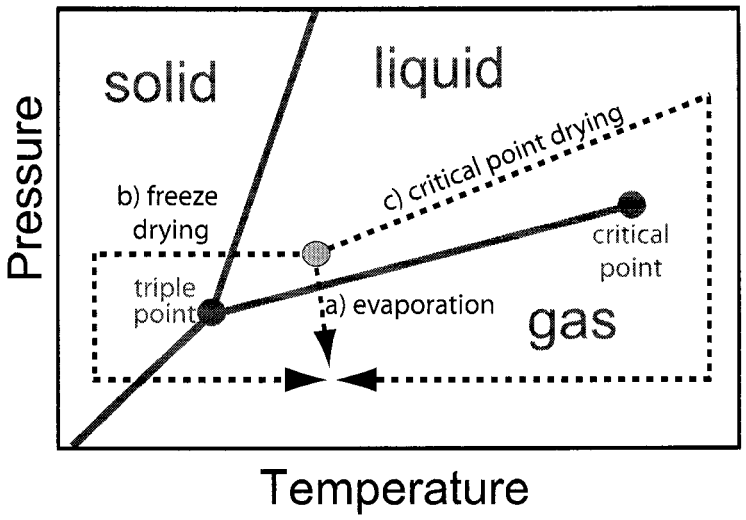

Figure 7.4: Principles of critical point drying and freeze drying on a generic phase diagram. By starting with a wet gel, there are in general three ways to remove the background liquid by transitioning to the gas phase. The simplest is to evaporate the liquid, directly transitioning from liquid to gas, as in (a). However, as the liquid evaporates, surface tension at the liquid/gas interface causes the gel network to collapse. To preserve the network structure, the liquid/gas interface is avoided. b) In freeze-drying, the sample is flash frozen, and placed under vacuum. The temperature is then raised to allow the ice to sublimate. c) In critical-point drying, the pressure and temperature are raised above the critical point, where liquid and gas cease to be separate phases. Once above the critical point, the pressure is slowly released, and the sample is subsequently cooled.

By cooling the sample rapidly, crystals nucleate at many points at the same time, creating small microcrystalline domains that result in smaller perturbations in the matrix than if the sample was frozen slowly. Therefore, for preserving the structure of freeze-dried samples, it is desirable to freeze the samples quickly. In SWNT aerogels, the samples are flash-frozen by immersion in liquid nitrogen. A commercial freeze-dryer (Labconco FreeZone 4.5 Liter Benchtop Freeze Dry System) is used to perform the drying. The drying proceeds overnight.

Critical-point drying bypasses the liquid/gas interface by using high pressure and temperature to place the background liquid in a state above the critical point at which liquid and gas cease to be separate phases. The critical point of water is at 374°C and 217.7 atm. The high temperature required to reach the critical point is sufficient to destroy many organic samples, and the high

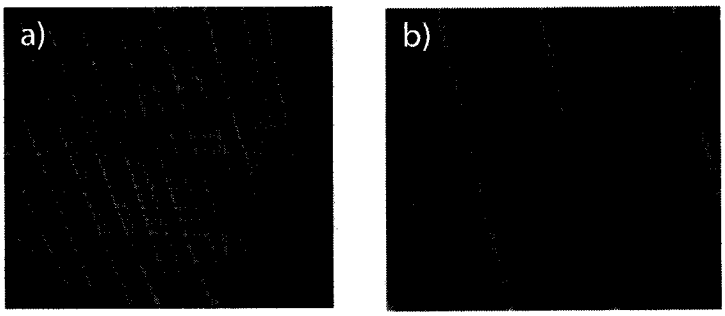

Figure 7.5: Zone refinement is seen in this optical image of fluorescently-labeled DNA being frozen in a thin glass cell. a) ice "fingers" (large dark features) grow through the liquid and push DNA out of the way. Note the brighter fluorescence, i.e., higher DNA concentration, at the liquid/ice interface. Field of view is $\sim$600 μm. b)As the sample solidifies, the DNA is concentrated in the narrow bands between the ice fingers.

pressures are difficult to achieve and may be dangerous. A more tenable approach relies on carrying out a solvent exchange to a liquid with a more accessible critical point. The most common such solvent is liquid carbon dioxide, whose critical point is at 31.1°C, 72.8 atm. Since liquid CO_2 is immiscible with water, an intermediate solvent exchange to ethanol is carried out first. Ethanol is completely miscible with both water and liquid CO_2. To carry out the intermediate solvent exchange, the sample is soaked in pure, anhydrous ethanol for several hours to overnight, and the ethanol is changed at least three times to ensure a complete exchange. The gels are then subjected to critical-point drying in a Tousimis SAMDRI-PVT-3B critical-point dryer using the manufacturer recommended drying procedure. The ethanol-soaked gel sample is placed along with excess ethanol in the drying chamber and cooled below 0°C. The ethanol solvent is replaced by liquid CO_2 by flushing the chamber for several minutes. The chamber is then sealed and heated above the critical point of CO_2. After stabilizing for several minutes, the pressure in the chamber is slowly released over approximately 20 min at a constant temperature. When atmospheric pressure is reached, the sample is taken out of the chamber. Because of the high pressures required for critical-point drying, this method requires significantly more costly equipment than freeze drying

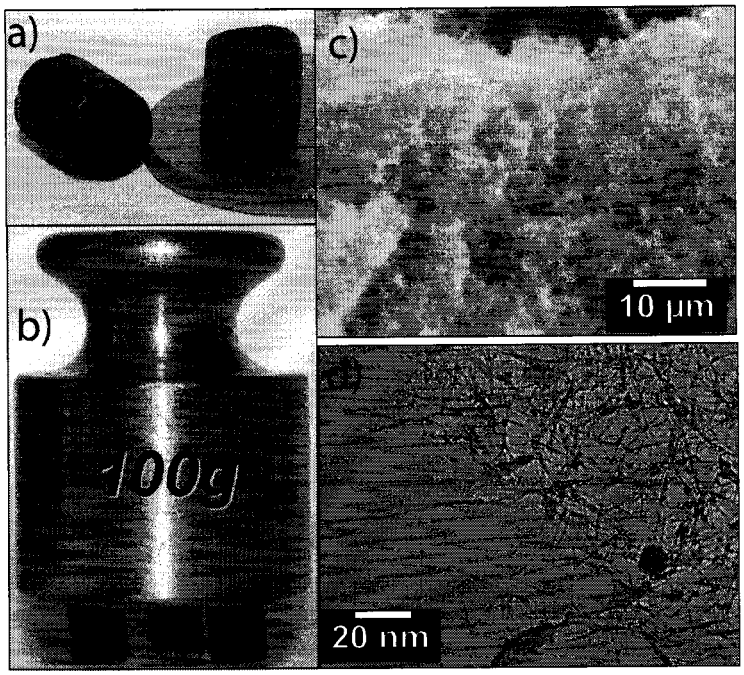

Figure 7.6: Images of aerogels. a) Macroscopic pieces of 7.5 mg/mL CNT aerogels. Pristine CNT aerogel (left) appears black, while the aerogel reinforced in a 1 wt% PVA bath (right) is slightly gray. b) Three PVA-reinforced aerogel pillars (total mass = 13.0 mg) supporting 100 g, or ~8000 times their weight. c) SEM image of a critical-point dried aerogel reinforced in a 0.5 wt% PVA solution (CNT content = 10 mg/mL) reveals an open, porous structure. d) High-magnification TEM image of an unreinforced aerogel reveals small-diameter CNTs arranged in a classic filamentous network.

and is usually performed on a small scale in research applications. However, because the distortion of the carbon nanotube network is minimized, critical point drying yields superior aerogels, as will be described later in this chapter.

7.3 Aerogel Structure

Images of typical critical-point dried aerogels are seen in Fig. 7.6. Unreinforced aerogels are fragile, but strong enough to permit careful handling. Reinforcement of aerogels with polyvinyl alcohol (PVA) polymer [118, 149, 150] improves the strength and stability of the aerogel. In the

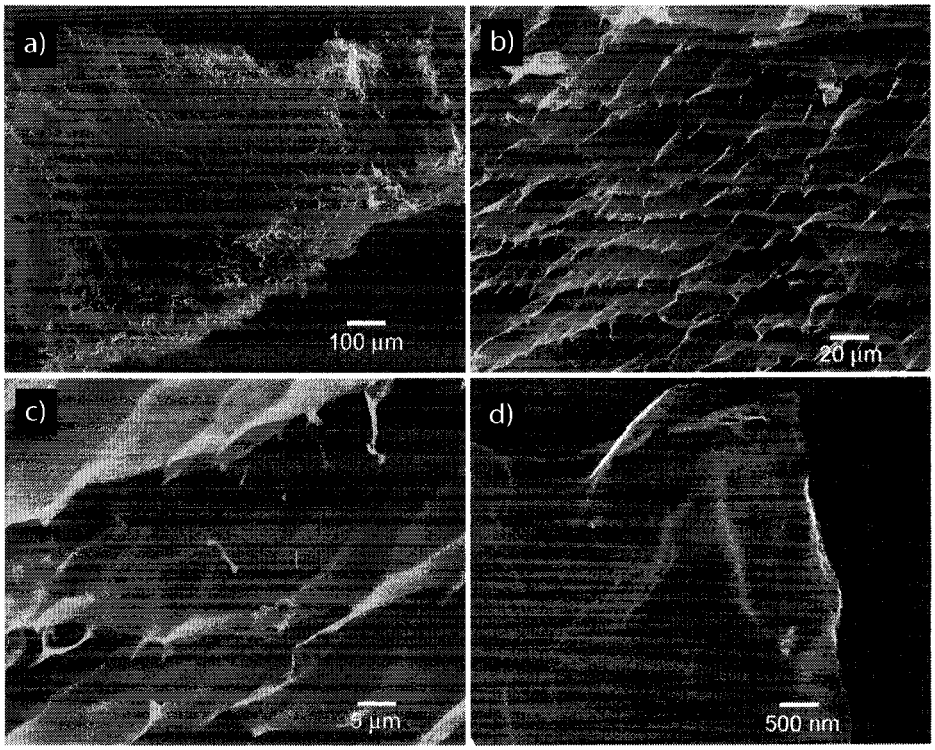

Figure 7.7: a) Freeze-dried aerogels sometimes have a second porosity lengthscale of order tens to hundreds of μm, as seen in this SEM image of an unreinforced aerogel (7.5 mg/mL CNT content. b) The large pores in freeze-dried aerogels are a result of the growth of ice crystals during freezing, and can have remarkably regular patterns, including the cellular structures seen here. c) closeup of a honeycomb structure. d) Individual CNTs are seen here compressed into a thin layer due to the pressure of the ice crystals. Many other morphologies are also observed in freeze-dried samples.

latter case, the aerogels can support at least 8000$\times$ their own weight, as shown in Fig. 7.6(b). All of the aerogels (with or without PVA reinforcement) are highly porous, with pore sizes ranging from tens of nanometers up to one micron. TEM images like the one in Fig. 7.6(d), prepared by shredding (pulling apart) unreinforced CNT aerogels above a TEM sample grid, suggest nanotubes in the aerogels form a random filamentous network [163] with little bundling. In the absence of bundling, the nanotube surface area is very large, a unique feature potentially useful for applications that require materials with large surface-area-to-volume ratios, including chemical sensors,

reaction catalysts and novel electrodes. The freeze-dried samples sometimes have a second porosity length scale of the order of tens to hundreds of microns as a result of ice crystals that form during the freezing process and displace nanotubes within the network. Some examples of the network distortion are shown in Fig. 7.7. Densities of the CNT aerogels studied range from 10 - 30 mg/mL with no PVA reinforcement, to 40 - 60 mg/mL for aerogels reinforced in a 1 wt% PVA bath. The PVA content in the aerogels can be estimated by subtracting the known mass of the CNTs in each sample, as determined from the sample volume and initial CNT gel concentration. We find that the PVA content in the aerogel increases with increasing bath PVA concentration, and also depends on the CNT concentration. PVA to CNT weight ratios range between 1 and 6 for all reinforced samples, with most samples ranging between 2 and 3, as shown in Fig 7.8.

7.4 Electrical Properties

The electrical conductivity of the aerogels is measured by a two-probe method in high vacuum ($<10^{-5}$ Torr), after painting the flat surfaces of the cylindrical samples with conductive paint (DuPont 4929N), see the inset of Fig. 7.9(b). Separate four-point conductivity measurements are made by painting additional parallel ring electrodes around the circumference of the sample, in a geometry presented in chapter 5 and Ref. [21]. By isolating the bulk sample conductivity from any electrode contact resistance, these measurements confirm that the breakdown occurs in the bulk of the sample, not just at the electrodes.

7.4.1 Nominal Electrical Conductivity

The electrical conductivity of the aerogels is found to depend on several factors, including nanotube and PVA content, and the drying process (i.e., freeze drying or critical-point drying). The

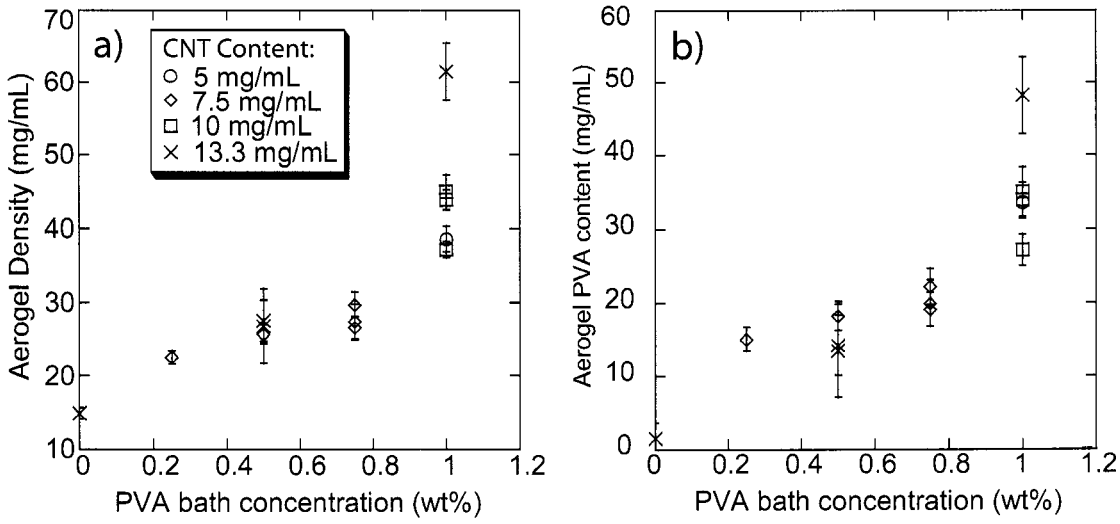

Figure 7.8: a) Densities of some critical-point dried aerogels are plotted vs. the PVA bath concentration. The density increases with increasing PVA bath concentration and depends on the CNT content of the aerogel. b) PVA content in the aerogels can be estimated by subtracting the CNT weight from the total weight of the aerogel sample. The CNT weight is determined to an accuracy of $\sim$10% from the CNT content in the precursor gel and the measured sample volume. The average PVA content ranges between 15 to 50 mg/mL, which corresponds to PVA to CNT weight ratios of between 1 and 6. The observed variation in aerogel PVA content with PVA bath concentration could be a result of deposition of more than one PVA layer on the nanotubes and/or deposition of residual PVA from the solution during solvent exchange.

freeze-dried samples are consistently less conductive than the critical-point dried samples. We attribute this difference to disruptions of the nanotube network that occur during the freezing process such as those described above. Samples created by critical-point drying suffer significantly less mechanical distortion and have more reproducible conductivities. Fig. 7.9 summarizes our results for a variety of CNT and PVA bath concentrations. In Fig. 7.9(a), aerogel conductivity is plotted as function of CNT content, while the PVA bath concentration is held constant at 1 wt%. In Fig. 7.9(b), the conductivity is plotted against PVA bath concentration, while the CNT content is fixed at 7.5 mg/mL. As can be seen, a 7.5 mg/mL CNT aerogel with no PVA has a conductivity of nearly 1 S/cm, significantly higher than typically obtained in solid carbon nanotube/polymer

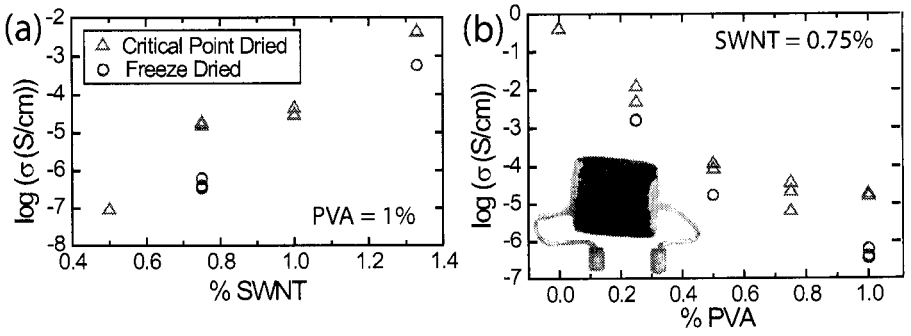

Figure 7.9: Conductivities of as-prepared CNT aerogel samples. a) Dependence of CNT content on the conductivity. The bath PVA content is fixed at 1 wt%. b) Dependence of aerogel conductivity on PVA content. CNT content is fixed at 7.5 mg/mL. Inset depicts the electrical connections to an aerogel sample.

composites with comparable nanotube volume fractions of order 1% [21]. Although the addition of PVA into the bath reinforces the physical structure of the aerogel, the electrical conductivity of the reinforced aerogels is initially significantly reduced. After reinforcement in a 1 wt% PVA solution, for example, the conductivity drops by five orders of magnitude to $\sim 10^{-5}$ S/cm. This level of conductivity is more typical of solid polymer composites with comparable nanotube volume fractions of order 1% [21]. For comparison, aligned CNT/PVA fibers, which are significantly more dense ($\sim$1.3 g/cm^3) have conductivities of $\sim$10 S/cm [149].

7.4.2 Conductivity Enhancement

While the physical reinforcement provided by PVA is often desirable, the concurrent reduction in conductivity may present problems for certain applications. Interestingly, we discovered that short, high-current pulses applied to a PVA-reinforced aerogel sample produce stepwise, irreversible increases in network electrical conductivity. The net increase can be quite large, for example several orders of magnitude, as shown for a critical-point dried sample in Fig. 7.10.

In a typical configuration, the sample is placed under high vacuum and 15 ms current pulses

of increasing amplitude are applied across the sample as shown in Fig. 7.10(a). The current pulses are spaced at least 30 seconds apart and kept as short as possible to minimize bulk heating of the sample, which can cause significant distortion of the network and the sample as a whole. The maximum current applied in our experiments is 100 mA, as limited by our instrumentation. A transient increase in conductivity is observed immediately after each pulse, followed by a partial rebound, as seen in Fig. 7.10(b) and (c). Following a stepwise increase of the current with each pulse up to the 100 mA instrumentation limit, the conductivity of all samples is $\sim 10^{-2}$ S/cm, regardless of the initial conductivity. This appears to be the limit for our samples at this current/pulse duration combination. Repeated pulsing at a constant current level does not significantly change the resistance of the sample. However, currents beyond the 100 mA used here might result in even higher final conductivities, perhaps up to those of pristine aerogel or higher.

Measurements of sample mass and volume before and after applying current pulses, as well as SEM imaging suggest the aerogel structure does not noticeably change either macroscopically or microscopically during this pulsing process as long as the duration of the current pulses is minimized to reduce bulk heating of the sample. While the mechanism for this breakdown is not fully understood, one interpretation is that the current pulses effectively remove or decompose PVA at the junctions between the nanotubes. Preliminary results suggest the breakdown can be effected either in vacuum or in a gaseous atmosphere, with subtle differences depending on environment.

7.5 Composite Applications

The CNT aerogels described here present a distinctive opportunity for creating composite materials with exceptional electrical conductivities and unique compositions. Although heavily researched, carbon nanotube composites have not as yet provided the levels of electrical conductivity that might

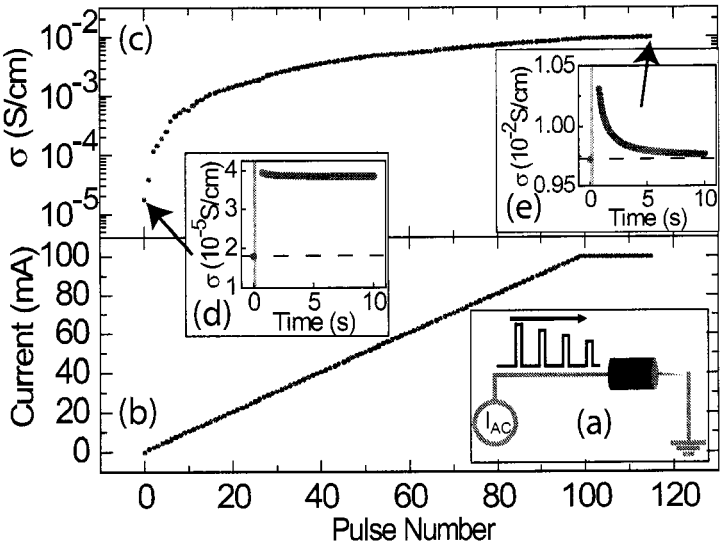

Figure 7.10: (a) Discrete current pulses, I_p, applied across a sample, as shown in this schematic, improve the electrical conductivity of PVA reinforced CNT aerogels. (b) A 15 ms, 0.5 mA current pulse (depicted by vertical gray line) is applied to a 13.3 mg/mL CNT critical-point dried sample reinforced in a 0.5 wt% PVA bath. The conductivity improves by $\sim 2\times$ after the pulse, and remains at the new level indefinitely. (c) A 15 ms, 100 mA current pulse is applied across the same sample, after the sample has undergone repeated current pulses and the starting resistance is much lower. Although the current here is much higher, conductivity improves only transiently, presumably due to heating, and returns to the original value in a matter of seconds. (d) and (e) show the full breakdown history of this sample. (d) Pulsing current is linearly increased up to 100 mA (pulse duration is always 15 ms; pulses are spaced more than 30s apart). Each point represents a discrete current pulse. Arrows point to the pulses depicted in (b) and (c). (e) The corresponding steady-state conductivity, measured 30s after each pulse. Notice, the conductivity improved by several orders of magnitude after repeated pulsing.

be anticipated based on the conductivity of isolated nanotubes. This can be partly attributed to the often contradictory goals of dispersing CNTs in a host material while simultaneously attempting to form a strongly connected nanotube network [21, 23]. As a result, and due to the difficulty of dispersing single-wall and small diameter carbon nanotubes in most materials, methods for creating composites are usually highly specific to a particular host material and are sensitive to many variables [21].

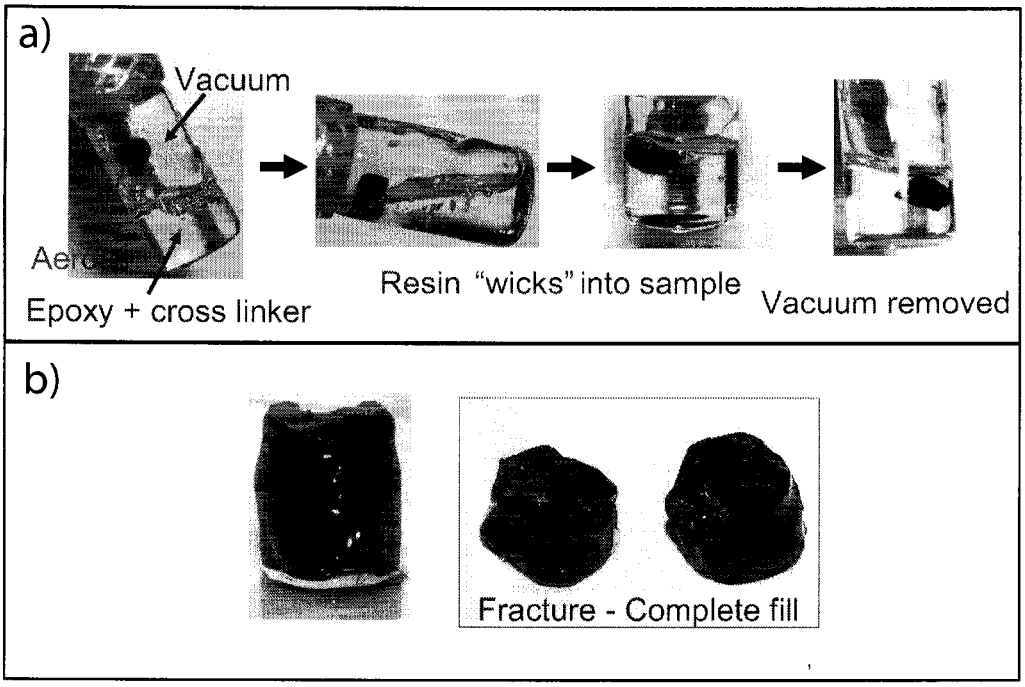

Figure 7.11: (a) Aerogel sample (7.5 mg/mL CNT, 0.5% PVA bath) backfilled under vacuum with Epon 828 epoxy resin and EpiKure 3234 cross-linker. (b) The sample is removed from the resin and left to cure. Fracturing the sample reveals that the infiltration of the sample by the resin was complete; no voids or bubbles are evident.

In the process described herein, the aerogel CNT network is created under controlled conditions, and the conductivity can therefore be significantly higher than is possible with other methods. This optimized nanotube network can then be backfilled with a host material. For example, we have found that immersing the aerogel in a liquid leads to complete impregnation of the aerogel through a "wicking" [153] or infiltration [42] process. The liquid can be a polymer or other material that can be subsequently cured to form a solid composite. For highly viscous liquids, the process is aided by placing the sample under vacuum. We have successfully impregnated PVA-reinforced aerogels with Epon 828 epoxy resin with EpiKure 3234 crosslinker, as shown in Fig. 7.11, and with Silbond H-5, a partially polymerized silica that was cured to produce silica/carbon-nanotube

composites. Our initial results with epoxy indicate that, upon backfilling and curing, the conductivity remains constant to within a factor of 2. Since the nanotube network is formed independently of the host material, the process should be useful for making composites which might not be otherwise feasible, for example, composites based on ceramic slurries or even metals [59].

In summary, we have created carbon nanotube aerogels from wet gel precursors that differ significantly from gelatin-nanotube foams [103] and high-temperature aerogels [96] reported previously. The nanotube aerogels are strong and electrically conducting, offering potential improvement over current carbon aerogel technologies for applications such as sensors, actuators, electrodes, thermoelectric devices, etc., as well as silica-based aerogel applications. We demonstrate the aerogels can be significantly reinforced by small amounts of PVA, albeit at the cost of reduced conductivity; the network conductivity, however, can be at least partially restored by applying current pulses through the sample. Lastly, the aerogel structures can be backfilled with polymeric fluids, which in turn can be cured to create novel electrically conducting solid composites.

Chapter 8

Conclusions

8.1 Summary

As described throughout this thesis, networks of carbon nanotubes in composites and suspensions have been studied by numerous research groups, with different studies often yielding different results. In our work, we have identified and explored a number of variables that affect the electrical and thermal properties of carbon nanotube networks. Among these are nanotube aspect ratio, nanotube dispersion quality and the resultant network morphology, the quality of contacts between the nanotubes, and the local environment near the nanotubes. In addition, by using purified carbon nanotubes, we were able to significantly reduce the effects of impurities that have influenced some past studies and thus we were able to extract more meaningful information about network properties.

We observed in chapter 5 that the threshold volume fractions depend on the SWNT aspect ratio, with, not surprisingly, longer and thinner nanotubes forming conductive networks at lower concentrations. More significantly, we found that the thresholds lie within the semi-dilute SWNT

concentration regime. We also showed that the electrical conductivity of carbon nanotube networks depend strongly on the nanotube dispersion, including the perhaps counterintuitive result that more inhomogeneous dispersions lead to lower thresholds. In particular, the electrical conductivity of SWNT-epoxy composites was found to depend on the amount of sonication. When sonication was stopped prior to curing, the SWNTs were able to partially re-aggregate and form chains. The resultant composites were more inhomogeneous, but had lower thresholds than composites made under continuous sonication throughout curing. By using this observation, we have created conducting nanotube composites at the lowest SWNT volume fractions to date.

The thermal conductivity studies of SWNT-epoxy composites (chapter 6) made with and without surfactant to aid in SWNT dispersion revealed that the addition of surfactant increased the thermal interfacial resistance between the nanotubes tenfold and resulted in worse thermal conductivity at comparable SWNT volume fractions. However, when surfactant was used, composites could be made at SWNT volume fractions as high as 0.1, whereas volume fractions of only 0.005 - 0.01 were possible when no surfactant was used. Because of the higher SWNT content, it was possible to attain a higher overall thermal conductivity enhancement in the surfactant processed composites, despite the increased thermal interfacial resistance.

In Chapter 7, we used a well-characterized dispersion process to create the first true carbon nanotube aerogels. These free-standing nanotube networks allowed us to probe the properties of the CNT network independently of any supporting material. We found that the electrical conductivity of a "pristine" CNT network is many orders of magnitude higher than the conductivity of comparable networks inside composites. Furthermore, we found that by adding PVA polymer to the aerogel for reinforcement, the conductivity dropped to levels more comparable to those of solid composites. This is likely due to a change in the contacts between nanotubes or a different local

environment the nanotube length. The latter reason makes our aerogels particularly interesting candidates for sensor applications, where changes in the electrical properties of the aerogel due to the local environment might be used to identify specific substances. We have also found that the conductivity of PVA-reinforced aerogels may be restored to near the pristine aerogel values by applying short, high current pulses across the SWNT network. While the origin of this conductivity enhancement is not well understood, it may be due to PVA being effectively removed or decomposed at the junctions or to changes in the local environment near the nanotubes, such as, for example, PVA desorption, decomposition, or re-alignment.

An interesting, though somewhat disappointing, feature of our studies of SWNT-epoxy composites is that the sought-after properties were achieved at a trade-off to other potentially desirable qualities. In the case of electrical conductivity, SWNT homogeneity was sacrificed to achieve lower threshold concentrations. In the thermal conductivity study, it was found that lower thermal interfacial resistance can be obtained by using bare SWNTs in place of surfactant-stabilized SWNT suspensions, but doing so reduced the maximum SWNT loading that could be obtained, and resulted in a lower overall thermal conductivity enhancement.

The CNT aerogel process was developed in part to surmount these tradeoffs by creating an "optimized" nanotube network independently of the host material. Whereas specific applications will dictate which processing methods are most appropriate, the aerogel study does offer indications that greater control over the nanotube network is possible and may be useful. Although creating the aerogel requires several additional steps, the process makes it possible to individually optimize the nanotube dispersion and homogeneity as well as the contact quality. In addition, the aerogel network should be compatible with any number of background materials. Such control over the network structure may be necessary for some applications.

The processes and data presented in this thesis should aid ongoing experimental and theoretical studies to explain how nanotube aspect ratio, nanotube dispersion quality, the quality of contacts between the nanotubes, and the local environment affect network conductivity. On the application level, our results provide a method for making conductive epoxy composites at the lowest SWNT concentrations to date, elucidate the effects of surfactant on thermally-conductive SWNT composites, and provide a way to create free-standing, three-dimensional networks of carbon nanotubes with significant control over the network properties.

8.2 Future directions

8.2.1 Aerogel improvement, characterization, and applications

The novel carbon nanotube aerogels presented in this thesis hold the potential for numerous applications. As mentioned in chapter 7, the high surface-area to volume ratios of the aerogels makes them ideal candidates for electrode materials, chemical and biological sensors, and reaction catalysts. Many properties of the aerogels remain unknown, however, and improvements to the process for making the aerogels may yield improved properties and simpler production methods.

Developing useful aerogel applications hinges on a thorough characterization of the aerogel properties. A quantitative determination of the surface-area-to-volume ratios may be possible through BET nitrogen adsorption studies [20, 115], a common method used to estimate the surface areas of other porous carbons. "BET" stands for the initials of the names of the method's inventors [20]. It may also be possible to determine the amount of nanotube bundling in the aerogel through fluorescence measurements similar to those described in chapter 3. The production process may then be adjusted to reduce bundling and increase the available surface area.

Preliminary results in various gaseous environments suggest that the electrical conductivity of the aerogels depends on the surrounding gas, pointing to potential chemical sensor applications and offering a unique opportunity to study how a nanotube network reacts when subjected to various environments. The latter is an important problem in the field, and a deeper experimental understanding of these interactions could pave the way for improved nanotube composites and other applications. Detailed measurements of the electrical properties of the aerogels in various media, i.e., gaseous, liquid, or solid environments, should provide insight into how the immediate environment near the nanotubes affects network conductivity. This knowledge may provide ways to reduce interfacial resistances and improve network conductivities, a central topic in this thesis. Measurements of the complex impedance of a *single* aerogel in *different* environments may be of particular interest. The response may be found to be specific to the particular molecules in the immediate environment of the nanotubes, and the measurement would offer significantly more information about the system than simple DC measurements.

While critical-point drying yielded superior aerogels in our studies, freeze-drying is significantly simpler and less expensive, and can be readily performed on an industrial scale. Freeze-drying may be the only option for creating large (i.e., meter-scale) aerogels for aerospace applications, for example. In our studies, the main drawback of freeze-drying was the displacement of the nanotubes within the network by ice crystals. The growth of ice crystals might be minimized with the use of cryoprotectants such as glycerol or polyethylene glycol, among others, or by using solvents other than water to minimize crystallite size. Improvements in the freeze-drying procedure would significantly reduce costs and raise the application potential of the aerogels.

While PVA reinforcement has proven effective, other methods of reinforcement may be far superior. Methods which would not deteriorate the conductivity and enhance the transport and/or mechanical properties would be particularly valuable. These may include fusing the SWNTs together (i.e., welding), connecting them together with an external linker akin to the PVA but electrically conducting (i.e., soldering), or physically tying the SWNTs together (i.e., weaving). A method for "welding" MWNTs using high-energy electron beams has been demonstrated, but welding SWNTs, especially within the random structure of the aerogel network, will likely prove challenging. Soldering may involve the use of conducting polymers in place of PVA, or by applying a metal coating of the aerogels. The latter may be achieved by solution-based electrolytic coating or by evaporation or sputtering. Preliminary results of the last method suggest that a sputtered gold layer penetrates into the aerogel to a skin-depth of approximately one millimeter or less. Skin depth may not be such a significant issue for solution-based electrolytic coatings due to shielding of electrostatic interactions by ions inside the aerogel pores.

8.2.2 Improved SWNT composites

The work described in this thesis presents several possible approaches to achieving improved electrical and thermal conductivities in SWNT composites. In particular, the enhanced conductivity of PVA-reinforced aerogels may provide a reproducible and robust method for creating highly conductive composite materials in a variety of matrix materials. Controlled studies of backfilling CNT aerogels to make composites are necessary to test the potential and limitations of the technique.

Our results with the electrical conductivity of SWNT composites suggest that SWNTs form stronger conducting networks if they are given time to re-aggregate into chains. The method used here was limited by the curing time of the epoxy, and it is not likely that the re-aggregation was

optimal. Methods may be developed that separate the curing of the composite from the network formation, so that the two processes may be studied and optimized independently. For example, using a photo-initiated cross-linker instead of the thermally-activated one used here may provide the opportunity to study the time-dependent component of network formation and to determine whether there is an "optimal" time between stopping sonication and curing that results in the best electrical properties. Another method for improving composite electrical conductivity is also suggested by the aerogel study. A conductivity enhancement due to current pulsing similar to the one described in chapter 7 was also observed in SWNT composites, albeit to a lesser degree. Early results suggest that applying high-current pulses to the SWNT-epoxy composites improves the conductivity by a factor of two or more. These results may warrant further study.

The tradeoff between lower thermal interfacial resistances and higher SWNT loadings on the resulting composite thermal conductivity might be alleviated by using dispersion aids other than NaDDBs surfactant. Agents that can be removed or modified after dispersion, but prior to curing, might be of particular interest. The goal here would be to reduce interfacial resistances while still facilitating high SWNT loading. Examples of such agents may include volatile co-surfactants or surfactants that may be cross-linked into the matrix background to reduce thermal damping. Since one origin of thermal interfacial resistance is dissimilarity in thermal expansion coefficients between the matrix and the inclusions, another possibility to mitigate these resistances may be to choose dispersion agents with thermal expansion coefficients more closely matched to the matrix material.

8.2.3 Theoretical issues

Our work on nanotube composites also raises some theoretical questions. While our simple percolation model correctly places the threshold in the semi-dilute concentration regime, it does not fully account for all of the differences between the two types of SWNTs studied. In both "sonicured" and "non-sonicured" composites, HiPco SWNTs percolate closer to the dilute limit than laser-oven SWNTs. It is unclear whether the effect is due to purely geometric differences between the nanotubes such as aspect ratio, differences in dispersion quality between the two types of nanotubes (e.g., shorter HiPco nanotubes disperse more easily and form chains more quickly), or other properties of the material. More detailed theoretical and simulation studies comparing network morphology to the transport and mechanical properties, as well as theoretical descriptions of chain formation in SWNT suspensions may yield useful information to improve our understanding of such systems.

Fields related to carbon nanotubes and carbon nanotube networks are heavily researched and rapidly evolving, but they are still far from mature. The work presented here, while offering insight into some currently relevant problems, is also also a starting point toward future work that has the potential to create novel and unique materials and devices and to offer a deeper understanding of the physics of random networks.

Bibliography

[1] *Single Wall Nanotube Composites*, Yodh, A.G., Islam, M.F., and Bryning, M.B. (U.S. Patent Application No. not yet assigned, filed July 7, 2004).

[2] References 1 and 10 use the same underlying theory, but the approximations in reference 1 are better suited for long, thin, randomly-oriented conducting rods.

[3] Based on in-house characterization and personal correspondence with Alain Pnicaud, Philippe Poulin, and Thomas Swan, Inc.

[4] Improving the repeatability of ultra-high resistance and resistivity measurements. Keithley white paper.

[5] A. Allaoui, S. Bai, H. M. Cheng, and J. B. Bai. Mechanical and electrical properties of a mwnt/epoxy composite. *Composites Sci. Technol.* **62**, 1993 (2002).

[6] J. Als-Nielsen and D. McMorrow. *Elements of Modern X-ray Physics*. John Wiley & Sons, Ltd. New York (2001).

[7] M. S. Arnold, A. A. Green, J. F. Hulvat, S. I. Stupp, and M. C. Hersam. Sorting carbon nanotubes by electronic structure using density differentiation. *Nat. Nanotech.* **1**, 60 (2006).

[8] S. M. Bachilo, M. S. Strano, C. Kittrell, R. H. Hauge, R. E. Smalley, and R. B. Weisman. Structure-assigned optical spectra of single-walled carbon nanotubes. *Science* **298**, 2361 (2002).

[9] X. D. Bai, D. Li, D. Du, H. J. Zhang, L. F. Chen, and J. Liang. Laser irradiation fro purification of aligned carbon nanotube films. *Carbon* **42**, 2113 (2004).

[10] R. T. K. Baker. Catalytic growth of carbon filaments. *Carbon* **27**(3), 315 (1989).

[11] I. Balberg, C. H. Anderson, S. Alexander, and N. Wagner. Excluded volume and its relation to the onset of percolation. *Phys. Rev. B* **30**(7), 3933 (1984).

[12] I. Balberg, N. Binenbaum, and N. Wagner. Percolation thresholds in the three-dimensional sticks system. *Phys. Rev. Lett.* **52**(17), 1465 (1984).

[13] S. Bandow, G. Chen, G. U. Sumanasekera, R. Gupta, M. Yudasaka, S. Ijima, and P. Eklund. Diameter-selective resonant raman scattering in double-wall carbon nanotubes. *Phys. Rev. B* **66**, 075416 (2002).

[14] S. Barrau, P. Demont, E. Perez, A. Peigney, C. Laurent, and C. Lacabanne. Effect of palmitic acid in the electrical conductivity of carbon nanotubes-epoxy resin composites. *Macromolecules* **36**(36), 9678 (2003).

[15] H. J. Barraza, F. Pompeo, E. A. O'Rear, and D. E. Resasco. Swnt-filled thermoplastic and elastomeric composites prepared by miniemulsion polymerization. *Nanoletters* **2**, 797 (2002).

[16] J. M. Benoit, B. Corraze, and O. Chauvet. Localization, coulomb interactions, and electrical heating in single-wall carbon nanotubes/polymer composites. *Phys. Rev. B* **65**, 241405(R) (2002).

[17] S. Berber, Y. K. Kwon, and D. Tománek. Unusually high thermal conductivity of nanotubes. *Phys. Rev. Lett.* **84**(20), 4613 (2000).

[18] D. S. Bethune, C. H. Klang, M. S. de Vries, G. Gorman, R. Savoy, J. Vazquez, and R. Beyers. Cobalt-catalysed growth of carbon nanotubes with single-atomic-layer walls. *Nature* **363**, 605 (1993).

[19] M. J. Biercuk, M. C. Llaguno, M. Radosavljevic, J. K. Hyun, A. T. Johnson, and J. E. Fischer. Carbon nanotube composites for thermal management. *Appl. Phys. Lett.* **80**(15), 2767 (2002).

[20] S. Brunauer, P. H. Emmett, and E. Teller. Adsorption of gases in multimolecular layers. *J. Am. Chem. Soc.* **60**, 309 (1938).

[21] M. B. Bryning, M. F. Islam, J. M. Kikkawa, and A. G. Yodh. Very low conductivity thresholds in bulk isotropic swnt epoxy composites. *Adv. Mater.* **17**, 1186 (2005).

[22] M. B. Bryning, D. E. Milkie, M. F. Islam, , L. A. H. J. M. Kikkawa, and A. G. Yodh. Carbon nanotube aerogels. *Adv. Mater.* (2007).

[23] M. B. Bryning, D. E. Milkie, M. F. Islam, J. M. Kikkawa, and A. G. Yodh. Thermal conductivity and interfacial resistance in single-wall carbon nanotube epoxy composites. *Appl. Phys. Lett.* **87**(17), 161909 (2005).

[24] A. L. R. Bug, S. A. Safran, and I. Webman. Continuum percolation of rods. *Phys. Rev. Lett.* **54**, 1412 (1985).

[25] W. D. Callister, Jr. *Materials Science and Engineering: An Introduction.* Clarendon Press New York 1997 edition (John Wiley & Sons).

[26] F. Carmona, F. Barreau, P. Delhaes, and R. Canet. An experimental model for studying the effect of anisotropy on percolative conduction. *Phys. Paris Lett.* **41**, L–531 (1980).

[27] F. Carmona, P. Prudhon, and F. Barreau. Percolation in short fibers epoxy resin composites: Conductivity behavior and finite size effects near threshold. *Solid State Commun.* **51**, 255 (1984).

[28] T. Chen, G. J. Weng, and W. C. Liu. Effect of kapitza contact and consideration of tube-end transport on the effective conductivity in nanotube-based composites. *J. Appl. Phys.* **97**, 104312 (2005).

[29] L. Chico, L. X. Benedict, S. G. Louie, and M. L. Cohen. Quantum conductance of carbon nanotubes with defects. *Phys. Rev. B.* **54**(4), 2600 (1996).

[30] S. U. S. Choi, Z. G. Zhang, W. Yu, F. E. Lockwood, and E. A. Grulke. Anomalous thermal conductivity enhancement in nanotube suspensions. *Appl. Phys. Lett.* **79**(14), 2252 (2001).

[31] T. C. Choy. *Effective Medium Theory: Principles and Applications.* Clarendon Press Oxford (1999).

[32] A. R. Clarke and C. N. Eberhardt. *Microscopy Techniques for Materials Science.* CRC Press Boca Raton (2002).

[33] J. F. Colomer, C. Stephan, S. Lefrant, G. V. Tendeloo, I. Willems, Z. Knya, A. Fonseca, C. Laurent, and J. B.Nagy. Large-scale synthesis of single-wall carbon nanotubes by catalytic chemical vapor deposition (ccvd) method. *Chem. Phys. Lett.* **317**, 83 (2000).

[34] J. P. Dear, J. E. Field, and A. J. Walton. Gas compression and jet formation in cavities collapsed by a shock wave. *Nature* **332**, 505 (1988).

[35] P. Delaney, H. J. Choi, J. Ihm, S. G. Louie, and M. L. Cohen. Broken symmetry and pseudogaps in ropes of carbon nanotubes. *Nature* **391**, 466 (1998).

[36] Z. Dogic, J. Zhang, A. C. Lau, H. Aranda-Espinoza, P. Dalhaimer, D. E. Discher, P. A. Janmey, R. D. Kamien, T. C. Lubensky, and A. Yodh. Elongation and fluctuations of semi-flexible polymers in a nematic solvent. *Phys. Rev. Lett.* **92**(12), 125503–1 (2004).

[37] M. Doi and S. F. Edwards. *The Theory of Polymer Dynamics*. Oxford Science Publications Walton Street, Oxford OX2 6DP 1st edition (1986).

[38] M. S. Dresselhaus, G. Dresselhaus, and P. Avouris. *Carbon Nanotubes: Synthesis, Structure, Properties, and Applications*. Springer Berlin (2001).

[39] M. S. Dresselhaus, G. Dresselhaus, and P. C. Eklund. *Science of Fullerenes and Carbon Nanotubes*. Academic San Diego (1996).

[40] M. S. Dresselhaus and P. C. Eklund. Phonons in carbon nanotubes. *Adv. Phys.* **49**(6), 705 (2000).

[41] F. Du, J. E. Fischer, and K. I. Winey. Coagulation method for preparing single-walled carbon nanotube/poly(methyl methacrylate) composites and their modulus, electrical conductivity, and thermal stability. *J. Polym. Sci., B* **41**, 3333 (2003).

[42] F. Du, C. Guthy, T. Kashiwagi, J. E. Fischer, and K. I. Winey. An infiltration method for preparing single-wall nanotube/epoxy composites with improved thermal conductivity. *J. Polym. Sci., B* **44**, 1513 (2006).

[43] R. Duggal and M. Pasquali. Dynamics of individual single-walled carbon nanotubes inwater by real-time visualization. *Phys. Rev. Lett.* **96**, 246104 (2006).

[44] T. W. Ebbesen and P. M. Ajayan. Large-scale synthesis of carbon nanotubes. *Nature* **358**, 220 (1992).

[45] A. C. Ferrari and J. Robertson. Interpretation of raman spectra of disordered and amorphous carbon. *Phys. Rev. B* **61**(20), 14095 (2000).

[46] E. Flahaut, A. Govindaraj, A. Peigney, C. Laurent, A. Rousset, and C. N. R. Rao. Synthesis of single-walled carbon nanotubes using binary (fe, co, ni) alloy nanoparticles prepared in situ by the reduction of oxide solid solutions. *Chem. Phys. Lett.* **300**, 236 (1999).

[47] M. Foygel, R. D. Morris, D. Anez, S. French, and V. L. Sobolev. Theoretical and computational studies of carbon nanotube composites and suspensions: Electrical and thermal conductivity. *Phys. Rev. B* **71**, 104201 (2005).

[48] G. Gao, T. Çağin, and W. A. Goddard III. Energetics, structure, mechanical and vibrational properties of single-walled carbon nanotubes. *Nanotechnol.* **9**, 184 (1998).

[49] L. A. Girifalco, M. Hodak, and R. S. Lee. Carbon nanotubes, buckyballs, ropes, and a universal graphitic potential. *Phys Rev B* **62**(19), 13104 (2000).

[50] E. Gmelin, M. Asen-Palmer, M. Reuther, and R. Villar. Thermal boundary resistance of mechanical contacts between solids at sub-ambient temperatures. *J. Phys. D: Appl. Phys.* **32**, R19 (1999).

[51] J. C. Grunlan, A. R. Mehrabi, M. V. Bannon, and J. L. Bahr. Water-based single-walled-nanotube-filled polymer composite with an exceptionally low percolation threshold. *Adv. Mater.* **16**(2), 150 (2004).

[52] J. H. Hafner, M. J. Bronikowski, B. R. Ajamian, P. Nikolaev, A. G. Rinzler, D. T. Colbert, K. A. Smith, and R. E. Smalley. Catalytic growth of single-wall carbon nanotubes from metal particles. *Chem. Phys. Lett.* **296**, 195 (1998).

[53] J. H. Hafner, M. J. Bronikowski, B. R. Azamian, P. Nikolaev, A. G. Rinzler, D. T. Colbert, K. A. Smith, and R. E. Smalley. Catalytic growth of single-wall carbon nanotubes from metal particles. *Chem. Phys. Lett.* **296**(2), 195 (1998).

[54] R. Haggenmueller, H. H. Gommans, A. G. Rinzler, J. E. Fischer, and K. I. Winey. Aligned single-wall carbon nanotubes in composites by melt processing methods. *Chem. Phys. Lett.* **330**, 219 (2000).

[55] N. Hamada, S. Sawada, and A. Oshiyama. New one-dimensional conductors: Graphitic microtubules. *Phys. Rev. Lett.* **68**, 1579 (1992).

[56] A. Hartschuh, H. N. Pedrosa, L. Novotny, and T. D. Krauss. Simultaneous fluorescence and raman scattering from single carbon nanotubes. *Science* **301**, 1354 (2003).

[57] Z. Hashin. Assessment of the self consistent scheme approximation - conductivity of particulate composites. *J. Compos. Mater.* **2**, 284 (1968).

[58] Hexion Specialty Chemicals. Technical Data Bulletin RP:3075 EPON Resin 828 (2005). [Online; accessed 12-December-2006].

[59] O. Hjortstam1, P. Isberg, S. Sderholm, and H. Dai. Can we achieve ultra-low resistivity in carbon nanotube-based metal composites? *Appl. Phys. A* **78**(8), 1175 (2004).

[60] J. Hone, B. Batlogg, Z. Benes, A. T. Johnson, and J. E. Fischer. Quantized phonon spectrum of single-wall carbon nanotubes. *Science* **289**, 1730 (2000).

[61] J. Hone, M. C. Llaguno, N. M. Nemes, A. T. Johnson, J. E. Fischer, D. A. Walters, M. J. Casavant, J. Schmidt, and R. E. Smalley. Electrical and thermal transport properties of magnetically aligned single wall carbon nanotube films. *Appl. Phys. Lett.* **77**, 666 (2000).

[62] J. Hone, M. Whitney, C. Piskoti, and A. Zettl. Thermal conductivity of single-wall carbon nanotubes. *Phys. Rev. B* **59**, R2514 (1999).

[63] D. J. Hornbaker, S. J. Kahng, S. Misra, B. Smith, A. Johnson, E. Mele, D. Luzzi, and A. Yazdani. Mapping the one-dimensional electronic states of nanoscopic peapod. *Science* **295**, 828 (2002).

[64] L. A. Hough, M. F. Islam, B. Hammouda, A. G. Yodh, and P. A. Heiney. Structure of semidilute single-wall carbon nanotube suspensions and gels. *Nanoletters* **6**(2), 313 (2006).

[65] L. A. Hough, M. F. Islam, P. A. Janmey, and A. G. Yodh. Viscoelasticty of single wall carbon nanotube suspensions. *Phys. Rev. Lett.* **93**(16), 168102 (2004).

[66] L. W. Hrubesh. Aerogel applications. *J. Non-Cryst. Solids* **225**, 335 (1998).

[67] J. E. Huang, X. H. Li, J. C. Xu, and H. L. Li. Well-dispersed single-walled carbon nanotube/polyaniline composite films. *Carbon* **41**(14), 2731 (2003).

[68] S. M. Huang and L. M. Dai. Plasma etching for purification and controlled opening of aligned carbon nanotubes. *J. Phys. Chem. B* **106**(14), 3543 (2002).

[69] S. T. Huxtable, D. G. Cahill, S. Shenogin, L. P. Xue, R. Ozisik, P. Barone, M. Usrey, M. S. Strano, G. Siddons, M. Shim, and P. Keblinski. Interfacial heat flow in carbon nanotube suspensions. *Nat. Mater.* **2**, 731 (2003).

[70] S. Ijima. Helical microtubules of graphitic carbon. *Nature* **354**, 56 (1991).

[71] S. Ijima and T. Ichihashi. Single-shell carbon nanotubes of 1-nm diameter. *Nature* **363**, 603 (1993).

[72] M. F. Islam, A. M. Alsayed, Z. Dogic, J. Zhang, T. C. Lubensky, and A. G. Yodh. Nematic nanotube gels. *Phys. Rev. Lett.* **92**, 088303 (2004).

[73] M. F. Islam, D. E. Milkie, C. L. Kane, A. G. Yodh, and J. M. Kikkawa. Direct measurement of the polarized optical absorption cross section of single wall carbon nanotubes. *Phys. Rev. Lett.* **93**, 037404 (2004).

[74] M. F. Islam, D. M. Milkie, O. N. Torrens, A. G. Yodh, and J. M. Kikkawa. Magnetic heterogeneity and alignment of single wall carbon nanotubes. *Phys. Rev. B* **71**, 201401(R) (2005).

[75] M. F. Islam, E. Rojas, D. M. Bergey, A. T. Johnson, and A. G. Yodh. High weight fraction surfactant solubilization of single-wall carbon nanotubes in water. *Nanoletters* **3**, 269 (2003).

[76] M. E. Itkis, D. E. Perea, S. Niyogi, S. M. Rickard, M. A. Hamon, H. Hu, B. Zhao, and R. C. Haddon. Purity evaluation of as-prepared single-walled carbon nanotube soot by use of solution-phase near-ir spectroscopy. *Nanolett.* **3**(3), 309 (2003).

[77] D. E. Johnston, M. F. Islam, A. G. Yodh, and A. T. Johnson. Electronic devices based on purified carbon nanotubes grown by high-pressure decomposition of carbon monoxide. *Nat. Mater.* **4**, 589 (2005).

[78] A. Jorio, M. A. Pimenta, A. G. S. Filho, R. Saito, G. Dresselhaus, and M. S. Dresselhaus. Characterizing carbon nanotube samples with resonance raman scattering. *New J. Phys.* **5**, 139.1 (2003).

[79] A. Jorio, R. Saito, J. H. Hafner, C. M. Lieber, M. Hunter, T. McClure, G. Dresselhaus, and M. S. Dresselhaus. Structural (n,m) determination of isolated single-wall carbon nanotubes by resonant raman scattering. *Phys. Rev. Lett.* **86**(6), 1118 (2001).

[80] A. Jorio, R. Saito, T. Hertel, R. B. Weisman, G. Dresselhaus, and M. S. Dresselhaus. Carbon nanotube photophysics. *MRS Bull.* **29**(4), 276 (2004).

[81] C. Journet, W. K. Maser, P. Bernier, A. Loiseau, M. Lamy de la Chapelle, S. Lefrant, P. Deniard, R. Lee, and J. E. Fischer. Large-scale production of single-walled carbon nanotubes by the electric-arc technique. *Nature* **388**, 756 (1998).

[82] C. L. Kane and E. J. Mele. Ratio problem in single carbon nanotube fluorescence spectroscopy. *Phys. Rev. Lett.* **90**(20), 207401–1 (2003).

[83] H. Kataura, Y. Kumazawa, Y. Maniwa, I. Umezu, S. Suzuki, Y. Ohtsuka, and Y. Achiba. Optical properties of single-qall carbon nanotubes. *Synth. Met.* **103**, 2555 (1999).

[84] B. Kim, J. Lee, and I. Yu. Electrical properties of single-wall carbon nanotube and epoxy composites. *J. appl. phys.* **94**(10), 6724 (2003).

[85] S. Kirkpatrick. Percolation and conduction. *Rev. Mod. Phys.*, **45**, 574 (1973).

[86] C. Kittel. *Introduction to Solid State Physics*. John Wiley & Sons, Inc. New York 7th edition (1996).

[87] J. Kong, A. M. Cassell, and H. Dai. Chemical vapor deposition of methane for single-walled carbon nanotubes. *Chem. Phys. Lett.* **292**, 567 (1998).

[88] J. Kong, H. T. Soh, A. M. Cassell, C. F. Quate, and H. Dai. Synthesis of individual single-walled carbon nanotubes on patterned silicon wafers. *Nature* **395**, 878 (1998).

[89] J. Kong, E. Yenilmez, T. W. Tombler, W. Kim, D. H., R. B. Laughlin, L. Liu, C. S. Jayanthi, and S. Y. Wu. Quantum interference and ballistic transmission in nanotube electron waveguides. *Phys. Rev. Lett.* **87**(10), 106801 (2001).

[90] A. Krishnan, E. Dujardin, T. W. Ebbesen, P. N. Yianilos, and M. M. J. Treacy. Young's modulus of single-walled nanotubes. *Phys. Rev. B.* **58**(20), 14013 (1998).

[91] U. Kuhlmann, H. Jantoljak, N. Pfander, P. Bernier, C. Journet, and C. Thomsen. Infrared active phonons in single-walled carbon nanotubes. *Chem. Phys. Lett.* **294**, 237 (1998).

[92] E. Kymakis, I. Alexandou, and G. A. J. Amaratunga. Single-walled carbon nanotube-polymer composites: electrical, optical and structural investigation. *Synth. Met.* **127**, 59 (2002).

[93] B. J. Landi, C. D. Cress, C. M. Evans, and R. P. Raffaelle. Thermal oxidation profiling of single-walled carbon nanotubes. *Chem. Mater.* **17**, 6819 (2005).

[94] B. J. Landi, H. J. Ruf, J. J. Worman, and R. P. Raffaelle. Effects of alkyl amide solvents on the dispersion of single-wall carbon nanotubes. *J. Phys. Chem. B* **108**, 17089 (2004).

[95] Y. J. Li, K. L. Wang, J. Q. Wei, Z. Y. Gu, Z. C. Wang, J. B. Luo, and D. H. Wu. Tensile properties of long aligned double-walled carbon nanotube strands. *Carbon* **43**(1), 31 (2005).

[96] Y. L. Li, A. Ian, and A. H. Windle. Direct spinning of carbon nanotube fibers from chemical vapor deposition synthesis. *Science* **304**, 276 (2004).

[97] D. R. Lide, ed. *CRC Handbook of Chemistry and Physics, Internet version*. CRC Press Boca Raton (2005).

[98] Y. Lin, B. Zhou, K. A. S. Fernando, P. Liu, L. F. Allard, and Y. P. Sun. Polymeric carbon nanocomposites from carbon nanotubes functionalized with matrix polymer. *Macromolecules* **36**, 7199 (2003).

[99] C. H. Liu, H. Huang, Y. Wu, and S. S. Fan. Thermal conductivity improvement of silicone elastomer with carbon nanotube loading. *Appl. Phys. Lett.* **84**(21), 4248 (2004).

[100] J. Liu, A. G. Rinzler, H. Dai, J. H. Hafner, R. K. Bradley, P. J. Boul, A. Lu, T. Iverson, K. Shelimov, C. B. Huffman, F. Rodriguez-Macias, Y. S. Shon, T. R. Lee, D. T. Colbert, and R. E. Smalley. Fullerene pipes. *Science* **280**, 1253 (1998).

[101] J. W. Mintmire, B. I. Dunlap, and C. T. White. Are fullerene tubules metallic? *Phys. Rev. Lett.* **68**(5), 631 (1992).

[102] V. L. Mironov. *Fundamentals of the Scanning Probe Microscopy*. The Russian Academy of Sciences Nizhniy Novgorod (2004).

[103] M. Nabeta and M. Sano. Nanotube foam prepared by gelatin gel as a template. *Langmuir* **21**(5), 1706 (2005).

[104] C. W. Nan, R. Birringer, D. R. Clarke, and H. Gleiter. Effective thermal conductivity of particulate composites with interfacial thermal resistance. *J. Appl. Phys.* **81**(10), 6692 (1997).

[105] C. W. Nan, G. Liu, Y. Lin, and M. Li. Interface effect on thermal conductivity on carbon nanotube composites. *Appl. Phys. Lett.* **85**(16), 3549 (2004).

[106] C. W. Nan, Z. Shi, and Y. Lin. A simple model for thermal conductivity of carbon nanotube-based composites. *Chem. Phys. Lett.* **375**, 666 (2003).

[107] S. Niyogi, M. A. Hamon, H. Hu, B. Zhao, R. S. P. Bhowmik, and M. E. Itkis. Chemistry of single-walled carbon nanotubes. *Acc. Chem. Res.* **35**, 1105 (2002).

[108] A. Nogales, G. Broza, Z. Roslaniec, K. Schulte, I. Šics, B. S. Hsiao, A. Sanz, M. C. García-Gutiérrez, D. R. Rueda, C. Domingo, and T. A. Ezquerra. Low percolation threshold in nanocomposites based on oxidized single wall carbon nanotubes and poly(butylene tereph-thalate). *Macromolecules* **37**(20), 7669 (2004).

[109] S. P. Obukhov. First order rigidity transition in random rod networks. *Phys. Rev. Lett.* **74**, 4472 (1995).

[110] M. J. OConnell, S. M. Bachilo, C. B. Huffman, V. C. Moore, M. S. Strano, E. H. Haroz, K. L. Rialon, P. J. Boul, W. H. Noon, C. Kittrell, J. P. Ma, R. H. Hauge, R. B. Weisman, and R. E. Smalley. Band gap fluorescence from individual single-walled carbon nanotubes. *Science* **297**, 593 (2002).

[111] Z. Ounaies, C. Park, K. E. Wise, E. J. Siochi, and J. S. Harrison. Electrical properties of single wall carbon nanotube reinforced polyimide composites. *Composites Sci. Technol.* **63**, 1637 (2003).

[112] M. J. B. P. Nikolaev, R. K. Bradley, F. Rohmund, D. T. Colbert, K. A. Smith, and R. E. Smalley. Gas-phase catalytic growth of single-walled carbon nanotubes from carbon monoxide. *Chem. Phys. Lett.* **313**, 91 (1999).

[113] C. Park, Z. Ounaies, K. A. Watson, R. E. Crooks, J. S. Jr., S. E. Lowther, J. W. Connell, E. J. Siochi, J. S. Harrison, and T. L. St.Clair. Dispersion of single wall carbon nanotubes by in situ polymerization under sonication. *Chem. Phys. Lett.* **364**, 303 (2002).

[114] R. W. Pekala. Organic aerogels from the polycondensation of resorcinol with formaldehyde. *J. Mater. Sci.* **24**, 3221 (1989).

[115] R. W. Pekala, J. C. Farmer, A. C. T., T. D. Tran, S. T. Mayer, J. M. Miller, and B. Dunn. Carbon aerogels for electrochemical applications. *J. Non-Cryst. Solids* **225**(1), 74 (1998).

[116] A. P. Philipse and A. M. Wierenga. On the density and structure formation in gels and clusters of colloidal rods and fibers. *Langmuir* **14**, 49 (1998).

[117] F. Pobell. *Matter and Methods at Low Temperatures*. Springer-Verlag Berlin; New York 2nd edition (1996).

[118] P. Poulin, B. Vigolo, and P. Launois. Films and fibers of oriented single wall nanotubes. *Carbon* **40**, 1741 (2002).

[119] D. Qian, G. J. Wagner, W. K. Liu, M. F. Yu, and R. S. Ruoff. Mechanics of carbon nanotubes. *Appl. Mech. Rev.* **55**(6), 495 (2002).

[120] R. Ramasubramaniam, J. Chen, and H. Liu. Homogeneous carbon nanotube/polymer composites for electrical applications. *Appl. Phys. Lett.* **83**(14), 2928 (2003).

[121] O. Regev, P. N. B. ElKati, J. Loos, and C. E. Koning. Preparation of conductive nanotube-polymer composites using latex technology. *Adv. Mater.* **16**, 248 (2004).

[122] L. Reimer. *Scanning Electron Microscopy - Physics of Image Formation and Microanalysis*. Springer Berlin 2nd edition (1998).

[123] D. Resasco, W. Alvarez, F. Pompeo, L. Balzano, J. Herrera, B. Kitiyanan, and A. Borgna. A scalable process for production of single-walled carbon nanotubes (swnts) by catalytic disproportionation of co on a solid catalyst. *J. Nanopart. Res.* **4**, 131 (2002).

[124] A. G. Rinzler, J. Liu, H. Dai, P. Nikolaev, C. B. Huffman, F. J. Rodriguez-Marcias, P. J. Boul, A. H. Lu, D. Heyman, D. T. Colbert, R. S. Lee, J. E. Fischer, A. M. Rao, P. C. Eklund, and R. E. Smalley. Large-scale purification of single-wall carbon nanotubes: process, product, and characterization. *Appl. Phys. A* **67**, 29 (1998).

[125] S. P. Rwei, F. H. Ku, and K. C. Cheng. Dispersion of carbon black in a continuous phase: Electrical, rheological, and morphological studies. *Colloid Polym. Sci.* **280**, 1110 (2002).

[126] M. Sahimi. *Applications of Percolation Theory*. Taylor & Francis London (1994).

[127] R. Saito, G. Dresselhaus, and M. S. Dresselhaus. *Physical Properties of Carbon Nanotubes*. Imperial College Press London (1998).

[128] R. Saito, M. Fujita, G. Dresselhaus, and M. S. Dresselhaus. Electronic structure of chiral graphene tubules. *Appl. Phys. Lett.* **60**, 2204 (1992).

[129] J. Sandler, M. S. P. Shaffer, T. Prasse, W. Bauhofer, K. Schulte, and A. H. Windle. Development of a dispersion process for carbon nanotubes in an epoxy matrix and the resulting electrical properties. *Polymer* **40**, 5967 (1999).

[130] J. Sandler, M. S. P. Shaffer, T. Prasse, W. Bauhofer, K. Schulte, and A. H. Windle. Development of a dispersion process for carbon nanotubes in an epoxy matrix and the resulting electrical properties. *Polymer* **40**, 5967 (1999).

[131] J. K. W. Sandler, J. E. Kirk, I. A. Kinloch, M. S. P. Shaffer, and A. H. Windle. Ultra-low electrical percolation threshold in carbon-nanotube-epoxy composites. *Polymer* **44**, 5893 (2003).

[132] O. A. Saunders. Notes on some radiation heat transfer formulae. *Proc. Phys. Soc.* **41**, 569 (1928).

[133] R. Schueler, J. Petermann, K. Schulte, and H. Wentzel. Agglomeration and electrical percolation behavior of carbon black dispersed in epoxy resin. *J. Appl. Polymer Science* **63**, 1741 (1997).

[134] C. Seoul, Y. T. Kim, and C. K. Baek. Electrospinning of poly(vinylidene fluoride)/dimethylformamide solutions with carbon nanotubes. *J. Polym. Sci., B* **41**(13), 1572 (2003).

[135] M. S. P. Shaffer and A. H. Windle. Fabrication and characterization of carbon nanotube/poly(vinyl alcohol) composites. *Adv. Mater.* **11**, 937 (1999).

[136] S. Shenogin, L. Xue, R. Ozisik, P. Keblinski, and D. G. Cahill. Role of thermal boundary resistance on the heat flow in carbon-nanotube composites. *J. Appl. Phys.* **95**(12), 8136 (2004).

[137] S. V. Slavov, A. R. Sanger, and K. T. Chuang. Mechanism of silation of silica with hexamethyldisilazane. *J. Phys. Chem. B.* **104**, 983 (2000).

[138] J. G. Smith Jr., J. W. Connell, D. M. Delozier, P. T. Lillehei, K. A. Watson, Y. Lin, B. Zhou, and Y. P. Sun. Space durable polymer/carbon nanotube films for electrostatic charge mitigation. *Polymer* **45**, 825 (2004).

[139] R. F. Speyer. *Thermal analysis of materials*. Marcel Dekker, Inc. New York (1994).

[140] T. V. Sreekumar, T. Liu, B. G. Min, H. Guo, S. Kumar, R. H. Hauge, and R. E. Smalley. Polyacrylonitrile single-walled carbon nanotube composite fibers. *Adv. Mater.* **16**(1), 58 (2004).

[141] C. Staii and A. T. Johnson. Quantitative analysis of scanning conductance microscopy. *Nanolett.* **4**(5), 859 (2004).

[142] D. Stauffer and A. Aharony. *Introduction to Percolation Theory*. Taylor & Francis London 2nd edition (1992).

[143] M. Su, B. Zheng, and J. Liu. A scalable cvd method for the synthesis of single-walled carbon nanotubes with high catalyst productivity. *Chem. Phys. Lett.* **322**(5), 321 (2000).

[144] Y. P. Sun, K. Fu, Y. Lin, and W. Huang. Functionalized carbon nanotubes: Properties and applications. *Acc. Chem. Res.* **35**, 1096 (2002).

[145] A. Thess, R. Lee, P. Nikolaev, H. J. Dai, P. Petit, J. Robert, C. H. Xu, Y. H. Lee, S. G. Kim, A. G. Rinzler, D. T. Colbert, G. E. Scuseria, D. Tomanek, J. E. Fischer, and R. E. Smalley. Crystalline ropes of metallic carbon nanotubes. *Science* **273**, 483 (1996).

[146] G. G. Tibbetts. Why are carbon filaments tubular? *J Cryst Growth* **66**(3), 632 (1984).

[147] A. Ugawa, A. G. Rinzler, and D. B. Tanner. Far-infrared gaps in single-wall carbon nanotubes. *Phys. Rev. B* **60**, R11305 (1999).

[148] B. Vigolo, C. Coulon, M. Maugey, C. Zakri, and P. Poulin. An experimental approach to the percolation of sticky nanotubes. *Science* **309**, 920 (2005).

[149] B. Vigolo, A. Pénicaud, C. Coulon, C. Sauder, R. Pailler, C. Journet, P. Bernier, and P. Poulin. Macroscopic fibers and ribbons of oriented carbon nanotubes. *Science* **290**, 1331 (2000).

[150] B. Vigolo, P. Poulin, M. Lucas, P. Launois, and P. Bernier. Improved structure and properties of single-wall carbon nanotube spun fibers. *Appl. Phys. Lett.* **81**(7), 1210 (2002).

[151] C. Vinches, L. Salome, C. Coulon, and F. Carmona. Critical concentration in percolating systems containing a high-aspect-ratio filler. *J. Phys. France* **51**, 2505 (1990).

[152] F. Wang, G. Dukovic, L. E. Brus, and T. F. Heinz. The optical resonances in carbon nanotubes arise from excitons. *Science* **308**, 838 (2005).

[153] J. Wang, L. Angnes, H. Tobias, R. A. Roesner, K. C. Hong, R. S. Glass, F. M. Kong, and R. W. Pekala. Carbon aerogel composite electrodes. *Anal. Chem.* **65**, 2300 (1993).

[154] Q. H. Wang, A. A. Setlur, J. M. Lauerhaas, J. Y. Dai, E. W. Seelig, and R. P. H. Changa. A nanotube-based field-emission flat panel display. *Appl. Phys. Lett.* **72**(22), 2912 (1998).

[155] Y. Wang, Z. Iqbal, and S. Mitra. Rapidly functionalized, water-dispersed carbon nanotubes at high concentration. *J. Am. Chem. Soc.* **128**, 95 (2006).

[156] J. Q. Wei, H. W. Zhu, B. Jiang, L. Ci, and D. H. Wu. Electronic properties of double-walled carbon nanotube films. *Carbon* **41**(13), 2495 (2003).

[157] N. Xu, Z. Wu, S. Deng, and J. Chen. High-voltage triode flat-panel display using field-emission nanotube-basedthin films. *J. Vac. Sci. Technol. B* **19**(4), 1370 (2001).

[158] Y. G. Yoon, M. S. C. Mazzoni, H. J. Choi, J. Ihm, and S. G. Louie. Structural deformation and intertube conductance of crossed carbon nanotube junctions. *Phys. Rev. Lett.* **86**(4), 688 (2001).

[159] M. Zhang, K. R. Atkinson, and R. H. Baughman. Multifunctional carbon nanotube yarns by downsizing an ancient technology. *Science* **306**, 1358 (2004).

[160] M. Zhang, S. L. Fang, A. A. Zakhidov, S. B. Lee, A. E. Aliev, C. D. Williams, K. R. Atkinson, and R. H. Baughman. Strong, transparent, multifunctional, carbon nanotube sheets. *Science* **309**, 1215 (2005).

[161] M. Zheng, A. Jagota, E. D. Semke, B. A. Diner, R. S. Mclean, S. R. Lustig, R. E. Richardson, and N. G. Tassi. Dna-assisted dispersion and separation of carbon nanotubes. *Nat. Mater.* **2**, 338 (2003).

[162] M. Zheng, A. Jagota, M. S. Strano, A. P. Santos, P. Barone, S. G. Chou, B. A. Diner, M. S. Dresselhaus, R. S. Mclean, G. B. Onoa, G. G. Samsonidze, E. D. Semke, M. Usrey, and D. J. Walls. Structure-based carbon nanotube sorting by sequence-dependent dna assembly. *Science* **302**, 1545 (2003).

[163] W. Zhou, M. F. Islam, H. Wang, D. L. Ho, A. G. Yodh, K. I. Winey, and J. E. Fischer. Small angle neutron scattering from single-wall carbon nanotube suspensions: evidence for isolated rigid rods and rod networks. *Chem. Phys. Lett.* **384**, 185 (2004).

[164] W. Zhou, Y. H. Ooi, R. Russo, P. Papanek, D. E. Luzzi, J. E. Fischer, M. J. Bronikowski, P. A. Willis, and R. E. Smalley. Structural characterization and diameter-dependent oxidative stability of single wall carbon nanotubes synthesized by the catalytic decomposition of co. *Chem. Phys. Lett* **350**, 6 (2001).

[165] J. Zhu, J. Kim, H. Peng, J. L. Margrave, V. N. Khabashesku, and E. V. Barrera. Improving the dispersion and integration of single-walled carbon nanotubes in epoxy composites through functionalization. *Nanoletters* **3**, 1107 (2003).